

Bacterial cytoskeletal filaments

Towards a DNA segregation system for a synthetic cell

Amini Hounejani, R.

DOI

[10.4233/uuid:79de9e6e-8201-499b-8d41-7c52ae450257](https://doi.org/10.4233/uuid:79de9e6e-8201-499b-8d41-7c52ae450257)

Publication date

2023

Document Version

Final published version

Citation (APA)

Amini Hounejani, R. (2023). *Bacterial cytoskeletal filaments: Towards a DNA segregation system for a synthetic cell*. [Dissertation (TU Delft), Delft University of Technology].
<https://doi.org/10.4233/uuid:79de9e6e-8201-499b-8d41-7c52ae450257>

Important note

To cite this publication, please use the final published version (if applicable).
Please check the document version above.

Copyright

Other than for strictly personal use, it is not permitted to download, forward or distribute the text or part of it, without the consent of the author(s) and/or copyright holder(s), unless the work is under an open content license such as Creative Commons.

Takedown policy

Please contact us and provide details if you believe this document breaches copyrights.
We will remove access to the work immediately and investigate your claim.

BACTERIAL CYTOSKELETAL FILAMENTS

TOWARDS A DNA SEGREGATION SYSTEM FOR A SYNTHETIC
CELL

BACTERIAL CYTOSKELETAL FILAMENTS

TOWARDS A DNA SEGREGATION SYSTEM FOR A SYNTHETIC
CELL

Dissertation

for the purpose of obtaining the degree of doctor
at Delft University of Technology

by the authority of the Rector Magnificus prof. dr. ir. T. H. J. J. van der Hagen,
chair of the Board for Doctorates,

to be defended publicly on

Wednesday 8 March 2023 at 12:30 o'clock

by

Reza AMINI HOUNEJANI

Master of Science in Physics,
Institute for Advance Studies in Basic Sciences (IASBS), Iran
Born in Esfahan, Iran

This dissertation has been approved by the promoters.

Composition of the doctoral committee:

Rector Magnificus, Prof. dr. A.M. Dogterom, Dr. C.J.A. Danelon,	Chairperson Delft University of Technology, promotor Delft University of Technology, copromotor
---	---

Independent members:

Prof. dr. J. Löwe,	Cambridge MRC-LMB, UK
Prof. dr. C. Joo,	Delft University of Technology
Prof. dr. S.J.J. Brouns,	Delft University of Technology
Dr. T. Shima,	The University of Tokyo, Japan
Dr. ir. L. Laan,	Delft University of Technology
Prof. dr. C. Dekker,	Delft University of Technology, reserve member



Keywords: Microtubules, bacterial microtubules, DNA segregation, PhuZ, TubZRC system, optogenetics, micro-fabrication, in vitro reconstitution, Monte Carlo simulations

Printed by: Gildeprint

Cover: Reza Amini - Masoud Amirkhani - Nemo Andrea - Reza Rahimi

Back cover: *When life is spent, what's Balkh or Nishapore?
What sweet or bitter, when the cup runs o'er?
Come drink! full many a moon will wax and wane
In time to come, when we are here no more.*
(Khayam - translation by: Whinfield)

Copyright © by Reza Amini Hounejani 2023

Casimir PhD Series, Delft-Leiden 2023-05

ISBN/EAN 978-90-8593-553-7

An electronic version of this dissertation is available at
<http://repository.tudelft.nl/>.

CONTENTS

Summary	vii
Samenvatting	ix
1 Introduction	1
1.1 Aim of this thesis	2
1.2 A synthetic cell	2
1.3 DNA segregation in eukaryotes	4
1.4 DNA segregation in bacteria	4
1.5 Bacterial cytoskeletal filaments	7
1.6 Spatiotemporal control based on optogenetics	10
1.7 Force generation by cytoskeletal filaments	10
1.8 Microtubule models	12
1.9 Thesis outline	12
2 Methods and Materials	15
2.1 Proteins	16
2.2 Micro-barrier fabrication	19
2.3 Stalling assay flow cell preparation	20
2.4 Fluorescence imaging	22
2.5 Analysis of filament dynamics	22
3 Dynamic instability of force-generating bacterial microtubules	27
3.1 Introduction	28
3.2 Results	29
3.3 Discussion	37
3.4 Methods and materials	40
4 Designing a minimal DNA segregation system for synthetic cells	47
4.1 Introduction	48
4.2 Results	51
4.3 Discussion	56
4.4 Materials and Methods	59
5 <i>In vitro</i> reconstitution of force-generating <i>PhuZ</i> filaments	67
5.1 Introduction	68
5.2 Results	70
5.3 Discussion	74
5.4 Methods and materials	77
6 Conclusion and Outlook	81

Bibliography	85
7 Bibliography	85
Acknowledgements	99
Curriculum Vitæ	101
List of Publications	103

SUMMARY

The past decades have seen the rapid development of many aspects of synthetic biology. For example, attempts to build synthetic cells under controlled conditions in the laboratory have led to significant achievements. Following a bottom-up approach, scientists aim at building a self-reproducing synthetic cell with a minimum number of biological modules. A functional synthetic cell should accomplish at least four processes during one cycle: growth, DNA replication, DNA segregation, and division. DNA segregation, as a vital step in the life cycle of a synthetic cell, is in focus in this thesis.

Segregation of replicated DNA in eukaryotes depends highly on microtubules. Microtubules are protein polymers which form cylindrical tubes, a dynamic structure with which they can exert both pulling and pushing forces. During cell division, microtubules form a spindle-like structure, named the mitotic spindle. Microtubules in the mitotic spindle apparatus attach to the replicated chromosomes through kinetochores and exert pulling forces to separate the sister chromosomes and place them in the newly born daughter cells. These hollow tubes can grow in the presence of GTP-bound tubulin dimers. When all the GTP-tubulin subunits at the end of a filament turned into GDP-tubulin, the microtubule exhibits a transition to shrinkage. While the addition of GTP-tubulin to the end of microtubules may cause pushing forces, shrinking microtubules are able to exert pulling forces with the help of microtubule adapter proteins. The random transitions between growth and shrinkage of a microtubule is called dynamic instability and has been studied throughout decades.

DNA segregation components of a synthetic cell should preferably be fully expressible in a cell-free manner which employs reconstituted transcription-translation factors. Although mitosis in eukaryotes is the best-studied DNA segregation system to date, microtubules are unsuitable for cell-free expression due to their complex chaperon-dependent folding as well as essential post-translational modifications. Interesting alternatives for DNA segregation in synthetic cells are provided by bacterial segregation systems. An active bacterial segregation system is ideally composed of three elements: a cytomotive NTPase filament, a connecting or adapter protein, and a centromere-like DNA sequence. This thesis will examine various bacterial cytoskeletal filaments with a central focus on their suitability for building a DNA segregation system for synthetic cells.

Bacterial microtubules which are the closest relatives to eukaryotic microtubules, both in sequence and in behavior, have been discovered in *Prostheco bacter* bacteria. Similar to eukaryotic microtubules, bacterial microtubules form dynamic filamentous polymers by assembling into a polar structure. In Chapter 3 of this thesis, we first employ micro-fabricated rigid barriers to study the dynamic behavior of bacterial microtubules in the presence of a stalling force. Then, by using cryo-ET tomograms of

both eukaryotic and bacterial microtubules, we compare the end structures of the two filaments. We conclude that both the dynamic and structural properties of force-generating bacterial microtubules are very similar to eukaryotic microtubules.

In Chapter 4, we assess whether bacterial microtubules can provide a partitioning cytomotive filament for low-copy plasmid segregation in a synthetic cell. Although bacterial microtubules were shown to be compatible with cell-free gene expression systems such as the PURE system, a failure to identify DNA-filament binding adapter proteins promoted us to consider other candidates among bacterial partitioning systems. TubZRC encoded by some bacterial virulence plasmids (*e.g.*, pBtoxis from *Bacillus thuringiensis*) or bacteriophages (*e.g.*, *Clostridium botulinum* phage c-st) have been hypothesized to maintain plasmids during cell division. Although the segregation based on this system has not been observed *in vivo*, *in vitro* reconstitution has revealed that treadmilling TubZ filaments transport the centromeric DNA sequence tubC mediated by TubR proteins. We therefore engineered an optogenetics-based system combining two natural systems in one hybrid system in order to perform plasmid segregation. The filament binding protein bTubC from *P. debontii* on the one hand and the DNA binding TubR protein from the TubZRC segregation system, on the other hand, were fused to iLID and SspB, respectively. We show that in the presence of blue light SspB-TubR may accumulate on bacterial microtubules through activated bTuC-iLID proteins.

Bacteriophages are the most abundant biological modules on earth. Different phages have evolved various mechanisms against host cell defense systems. One of the mechanisms which has been characterized recently protects the phage genome from DNA-targeting defense systems such as CRISPR-cas. To protect their genome, jumbo phages of *Pseudomonas* encode for a protein which forms a spherical structure, a phage nucleus, around the phage DNA. In search for cytomotive filament alternatives for DNA segregation, we studied PhuZ, a tubulin-like protein encoded by 201 ϕ 2-1 phages which has been shown to enhance phage production efficiency by localizing the phage nucleus and transporting capsids to the cell center. GTP-bound PhuZ proteins form three-stranded filaments and display dynamic instability both *in vivo* and *in vitro*. In Chapter 5 of this thesis we show that the interaction with a rigid barrier, mimicking the phage nucleus, leads to PhuZ filament destabilization. On the other hand, we observed that bundling stabilizes PhuZ filaments which *in vivo* may compensate for the destabilizing interaction with the phage nucleus. PhuZ concentration increases over time during infection. We hypothesize that minus end growth at higher PhuZ concentrations may facilitate the transition between dynamic instability and treadmilling during the infection process. Although no PhuZ adapter protein has been discovered yet, we hypothesize that these filaments could also be used in synthetic cell applications. However, further investigation is needed to find suitable PhuZ adapter proteins.

SAMENVATTING

De afgelopen decennia hebben veel aspecten van de synthetische biologie zich snel ontwikkeld. Zo hebben pogingen om in het laboratorium onder gecontroleerde omstandigheden synthetische cellen te bouwen tot belangrijke resultaten geleid. Volgens een bottom-up benadering streven wetenschappers naar het bouwen van een zelfgeproduceerde synthetische cel met een minimum aantal biologische modules. Een functionele synthetische cel moet tijdens één cyclus ten minste vier processen uitvoeren: groei, DNA-replicatie, DNA-segregatie en deling. DNA-segregatie, als een essentiële stap in de levenscyclus van een synthetische cel, staat centraal in dit proefschrift.

Segregatie van gerepliceerd DNA in eukaryoten hangt sterk af van microtubuli. Microtubuli zijn eiwitpolymeren die cilindrische buizen vormen, een dynamische structuur waarmee ze zowel trekkende als duwende krachten kunnen uitoefenen. Tijdens de celdeling vormen microtubuli een spindelachtige structuur, de mitotische spindel genoemd. Microtubuli in het mitotische spilapparaat hechten zich via kinetochoren aan de gerepliceerde chromosomen, en oefenen vervolgens trekkrachten uit om de zusterchromosomen te scheiden en in de pasgeboren dochtercellen te plaatsen. Deze holle buisjes kunnen groeien in de aanwezigheid van GTP-gebonden tubulinedimeren. Wanneer na GTP-hydrolyse alle GTP-tubuline-subeenheden aan het uiteinde van een filament veranderen in GDP-tubuline, vertoont de microtubule een overgang naar krimp. Terwijl de toevoeging van GTP-tubuline aan het uiteinde van microtubuli duwkrachten kan veroorzaken, kunnen krimpende microtubuli trekkrachten uitoefenen met behulp van microtubule-adaptoreiwitten. De willekeurige overgangen tussen groei en krimp van een microtubulus wordt dynamische instabiliteit genoemd en is gedurende tientallen jaren bestudeerd.

De componenten voor de DNA-segregatie van een synthetische cel moeten bij voorkeur volledig tot expressie kunnen worden gebracht op een celvrije manier die gereconstitueerde transcriptie-translatiefactoren gebruikt. Hoewel mitose in eukaryoten het best bestudeerde DNA-segregatiesysteem tot nu toe is, zijn microtubuli ongeschikt voor celvrije expressie vanwege hun complexe eiwitvouwing die chaperonne afhankelijk is, en vanwege de essentiële post-translationele modificaties. Interessante alternatieven voor DNA-segregatie in synthetische cellen worden geboden door bacteriële segregatiesystemen. Een actief segregatiesysteem bestaat idealiter uit drie elementen: een cytomotorisch NTPase-filament, een verbindend of adaptoreiwit, en een centromeerachtige DNA-sequentie. Dit proefschrift onderzoekt verschillende bacteriële cytoskeletfilamenten met een centrale focus op hun geschiktheid voor het bouwen van een DNA-segregatiesysteem voor synthetische cellen.

Bacteriële microtubuli die de naaste verwanten zijn van eukaryote microtubuli, zowel in volgorde als in gedrag, zijn ontdekt in *Prostheco bacter*-bacteriën. Net als eukaryote

microtubuli vormen bacteriële microtubuli dynamische filamenteuze polymeren door zich te assembleren tot een polaire structuur. In hoofdstuk 3 van dit proefschrift gebruiken we eerst micro-gefabriceerde stijve barrières om het dynamische gedrag van bacteriële microtubuli te bestuderen in de aanwezigheid van een blokkerende kracht. Vervolgens vergelijken we met behulp van cyro-ET-tomogrammen van zowel eukaryote als bacteriële microtubuli de eindstructuren van de twee filamenten. We concluderen dat zowel de dynamische als structurele eigenschappen van krachtgenererende bacteriële microtubuli sterk lijken op eukaryotische microtubuli.

In Hoofdstuk 4 beoordelen we of bacteriële microtubuli een scheidend cytomotorisch filament kunnen vormen voor segregatie van plasmiden met weinig kopieën in een synthetische cel. Hoewel werd aangetoond dat bacteriële microtubuli compatibel zijn met celvrije genexpressiesystemen zoals het PURE-systeem, heeft het niet identificeren van DNA-filament-adaptoreiwitten ons ertoe aangezet om andere kandidaten onder bacteriële partitiesystemen te overwegen. Van TubZRC gecodeerd door sommige bacteriële virulentieplasmiden (bijv. pBtoxis van *Bacillus thuringiensis*) of bacteriofagen (bijv. *Clostridium botulinum* faag c-st), wordt verondersteld dat ze plasmiden behouden tijdens celdeling. Hoewel de segregatie op basis van dit systeem niet *in vivo* is waargenomen, heeft reconstitutie *in vitro* onthuld dat TubZ-filamenten de centromere DNA-sequentie tubC transporteren door middel van een loopbandmechanisme, gemedieerd door TubR-eiwitten. Daarom hebben we een optogenetica-gebaseerd systeem ontwikkeld dat twee natuurlijke systemen combineert in één hybride systeem voor segregatie van plasmiden met weinig kopieën in synthetische cellen. Het filament-bindende eiwit bTubC van *P. debontii* enerzijds en het DNA-bindende TubR-eiwit van het TubZRC-segregatiesysteem anderzijds werden gefuseerd met respectievelijk iLID en SspB. We laten zien dat, in de aanwezigheid van blauw licht, SspB-TubR zich kan bevinden op bacteriële microtubuli door middel van geactiveerde bTuC-iLID-eiwitten.

Bacteriofagen zijn de meest voorkomende biologische modules op aarde. Verschillende fagen hebben verschillende mechanismen ontwikkeld tegen afweersystemen van de gastheercel. Een van de recentelijk gekarakteriseerde mechanismen beschermt het faaggenoom tegen op DNA gerichte verdedigingssystemen zoals CRISPR-cas. Om hun genoom te beschermen, coderen jumbofagen van *Psuedomonas* voor een eiwit dat een bolvormige structuur vormt, een faagkern, rond het faag-DNA. Op zoek naar alternatieven voor cytomotorische filamenten voor DNA-segregatie, bestudeerden we PhuZ, een tubuline-achtig eiwit gecodeerd door 201 ϕ 2-1 fagen waarvan is aangetoond dat het de faagproductie-efficiëntie verbetert door de faagkern te lokaliseren en capsiden naar het celcentrum te transporteren. GTP-gebonden PhuZ-eiwitten vormen driestrengige filamenten en vertonen zowel *in vivo* als *in vitro* dynamische instabiliteit. In hoofdstuk 5 van dit proefschrift laten we zien dat de interactie met een rigide barrière, die de faagkern nabootst, leidt tot destabilisatie van het PhuZ-filament. Aan de andere kant hebben we waargenomen dat bundeling de PhuZ-filamenten stabiliseert, wat *in vivo* de destabiliserende interactie met de faagkern kan compenseren. PhuZ-concentratie neemt toe tijdens de infectie. Onze hypothese is dat negatieve eindgroei bij hogere PhuZ-concentraties de overgang tussen dynamische instabiliteit

en tredmolen tijdens het infectieproces kan vergemakkelijken. Hoewel er nog geen PhuZ-adaptewit is ontdekt, veronderstellen we dat deze filamenten ook kunnen worden gebruikt in toepassingen van de synthetische cel. Er is echter verder onderzoek nodig om geschikte PhuZ-adaptewitten te vinden.

To my family

1

INTRODUCTION

*Come so that we can scatter flowers and fill the glass to brim with wine
Split heaven's ceiling with our powers and try a wholly new design*

Hafez Shirazi

An important aspect of a synthetic cell is the correct partitioning of the genomic material during division. DNA segregation systems have been discovered in bacterial cells which include a minimum number of components. These systems have been successfully isolated and their properties have been studied. However, steps still remain to be carried out to fully reconstitute them in a cell-free system like a synthetic cell. In this chapter, we briefly introduce a synthetic cell and the methodological aspects of it. Then, a number of minimal segregation systems are described with a focus on their cytomotive filaments which are the main players of DNA segregation in these systems.

1.1. AIM OF THIS THESIS

In recent years, there has been an increasing interest in creating a synthetic cell from isolated elements. Several attempts have been made to reconstitute biological processes essential for a functional living cell including growth [11], DNA replication and segregation [50, 69, 125, 130], and division (Figure 1.1) [8, 51, 72]. Despite some efforts, no reliable active DNA segregation system has been reconstituted in a cell-free manner to date. DNA segregation in eukaryotic cells is conducted through an enormously precise and complicated mechanism known as mitosis [91]. Microtubules play the main role in a mitotic spindle in collaboration with other proteins. Although microtubules are the best-studied cytoskeletal filaments, the extreme complexity and chaperon-dependent folding of eukaryotic tubulins are the major drawbacks which make them unsuitable for cell-free gene expression. In this thesis, we, therefore, explore bacterial cytoskeletal filaments to build an active minimal DNA segregation system for a synthetic cell in a bottom-up approach.

Several bacterial cytoskeletal filaments have been discovered in the last thirty years. Bacterial microtubules which have been discovered in *Prosthocobacter* strains display dynamic instability which is a crucial property of eukaryotic microtubules [31]. These filaments are called bacterial microtubules because they are the closest counterparts to eukaryotic microtubules [68]. On the other hand, TubZ, another tubulin-like GTPase protein has been shown to form filaments as well. Treadmilling is the hallmark of TubZ filaments and no dynamic instability has been observed for them. Treadmilling TubZ filaments are believed to be involved in DNA segregation inside bacterial cells although it is not experimentally proven [82]. TubZ filaments are also encoded by jumbo phages of *Pseudomonas* and form a distinct form of GTPase filaments: PhuZ filaments. These filaments exhibit dynamic instability and treadmilling [23, 41]. Interestingly, both features are essential for their role in phage production inside the host cell. We have studied various aspects of these systems by reconstituting their dynamic features *in vitro* with a synthetic cell application in mind.

In our synthetic cell, cell-free expression of the proteins will be conducted in a PURE background and the system should be encapsulated in vesicles. The PURE system is a protein synthesis system which includes transcription-translation machinery to conduct cell-free gene expression. Most of the experiments in this thesis, however, are performed using purified proteins. Purified proteins are labeled with fluorescent dyes and imaged with either total internal reflection fluorescence (TIRF) or confocal microscopes. In addition, optogenetic tools are explored to make the segregation externally controllable.

1.2. A SYNTHETIC CELL

A cell-free out-of-equilibrium system which is enclosed in a lipid bilayer and able to self-replicate is called a synthetic cell. The system needs to perform all the crucial steps of a living cell namely growth, gene replication and segregation, and division (Figure 1.1) [105]. After encapsulation of the genome material in a lipid bilayer container like a liposome, the transcription-translation machinery triggers the production of all nec-

essary molecules. During growth, DNA partitioning follows DNA replication and the replicated system subsequently undergoes a division (Figure 1.1). This completes a full cycle of life for a synthetic cell.

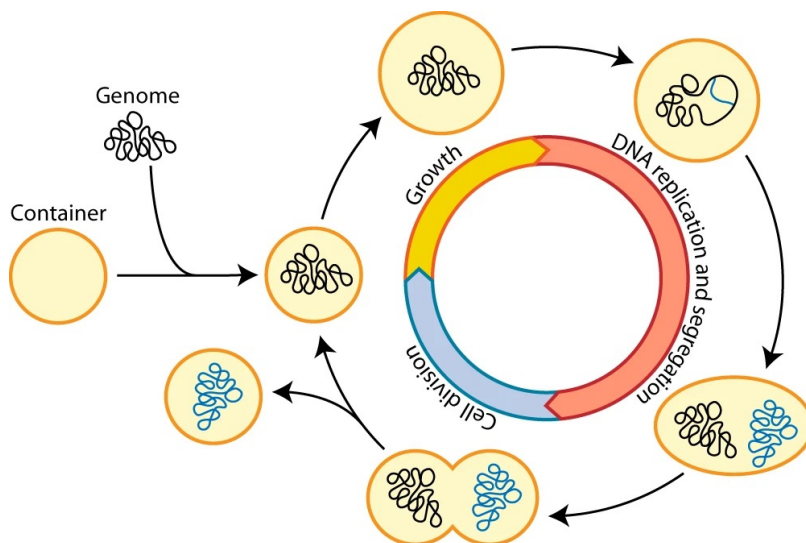


Figure 1.1: **Synthetic cell model:** A cartoon representation of a model synthetic cell. The three steps of growth, DNA replication and segregation, and division inside a container driven from a genome represent fundamental components of a synthetic cell. Growth is a continues process throughout the entire reproduction cycle. After initiative growth step, the enclosed genome undergoes consecutive replication and segregation steps which places the sister chromosomes in dividing daughter cells which continue to produce more new cells. Image from [105].

There are two main ways to approach building a minimal synthetic cell. In a top-down approach, the complexity of an organism is reduced by deleting the unnecessary sequences of its genome in a way that the organism remains functional [79]. In this thesis, however, we follow an approach called a bottom-up approach to building a synthetic minimal cell from the building blocks of various living cells. In a bottom-up approach, we mix and match ingredients until we have a functional cell which satisfies our definition of a synthetic cell.

One of the main components of our synthetic cell is a system which can accomplish protein expression. A reconstituted cell-free protein synthesis system under the commercial name PURE (Protein Synthesis Using Recombinant Elements) system or PUREflex® has been shown to successfully synthesize proteins of interest from the related genes in various studies [51, 69, 72]. The system is a combination of transcription and translation factors which are purified separately from *E. Coli* (the so-called S30 fraction) and is composed of energy regeneration and aminoacylation components (www.pureflex.genefrontier.com). As mentioned before, the system should be compartmentalized, therefore, liposomes will be used to separate the system from the environment.

Faithful transfer of genetic materials is an important aspect of the proliferation of all organisms. Different organisms have their distinct ways of genome partitioning which is known as DNA segregation [9, 53, 96, 111]. DNA segregation in our synthetic cell could be done with various methods given that it should include the minimum number of components and be compatible with our approach *i.e.*, compatible with cell-free expression and more specifically should be expressible in the PURE system. In the following sections we will discuss different DNA segregation methods and their potential applications in a synthetic cell.

1.3. DNA SEGREGATION IN EUKARYOTES

In eukaryotic cells, the segregation of replicated chromosomes is achieved accurately during a process called mitosis. An apparatus called the mitotic spindle forms during mitosis and is responsible for the pulling forces that are required to segregate the DNA [39, 129]. This mitotic spindle contains a considerable number of different proteins, but the main players in the process are microtubules (Figure 1.2A) [4, 111]. Microtubules (MTs) are cylindrical hollow tubes which form by polymerization of proteinous subunits $\alpha\beta$ -tubulins (Figure 1.2B) [129]. The GTPase tubulins assemble into microtubules by binding to GTP nucleotides and when a GTP-tubulin hydrolyses to a GDP-bound tubulin, the tubulin structure alters in a way that enhances destabilization of the filament [57]. An unstable MT may undergo depolymerization and thus shrink its length. The switching from a growing to a shrinking state is known as a catastrophe event. Microtubules may experience multiple cycles of growth and shrinkage in the presence of GTP-tubulin, a feature called dynamic instability [95].

During mitosis, MTs mostly nucleate from MTs organizing centers (MTOCs), anchor to the chromosomes centromeric regions through kinetochore protein complexes, and implement the segregation by applying pulling force [129]. One way to study DNA segregation in eukaryotes is to reconstitute its features *in vitro*. Attempts to reconstitute the mitotic spindle in lipid confinements have resulted in the formation of a minimal spindle-like structure with encapsulation of tubulin and MT associated proteins (MAPs) and motor proteins in water-in-oil droplets which have been able to self-organize (Figure 1.2C) [130]. Although the mitotic spindle is the best-studied DNA segregation apparatus and MTs are the best-known cytoskeletal filaments, complex and chaperon-dependent folding of tubulin dimers and a substantial number of necessary post-translational modifications make them inadequate for cell-free applications in our synthetic cell [70].

1.4. DNA SEGREGATION IN BACTERIA

DNA segregation in prokaryotic cells has evolved into a simpler and less developed machinery. According to the size and frequency of the chromosomal DNA, DNA segregation in bacteria has developed into three different mechanisms. High copy plasmid segregation happens without any external force and solely by random diffusion of the small plasmids [112]. The high frequency of the plasmids in this case ensures the uniform distribution of the information in daughter cells (Figure 1.3A, left). low-

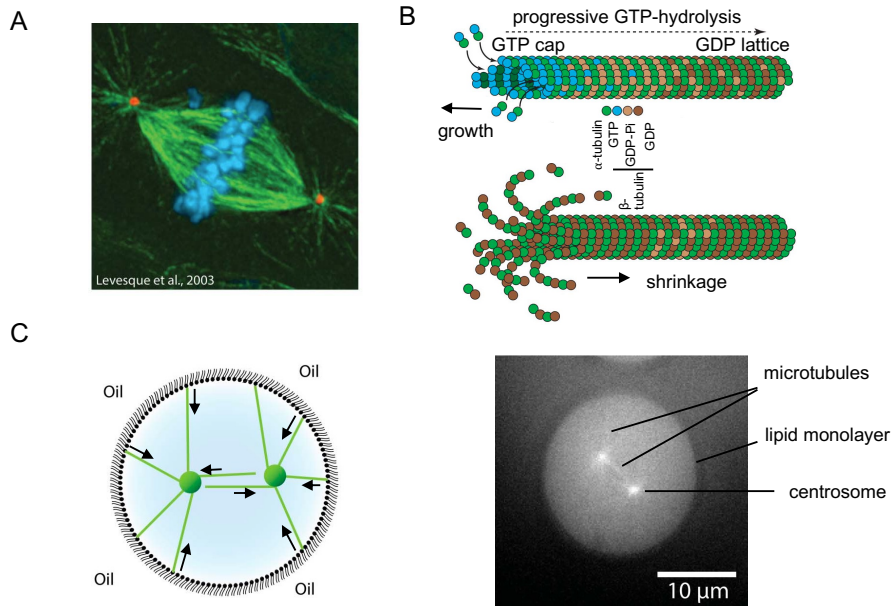


Figure 1.2: **Microtubules in DNA segregation in eukaryotes:** (A) Mitotic spindle formed by microtubules (green) which have grown from centrosomes (red) and are attached to the chromosomes (blue). Image from [84]. (B) Schematic depiction of microtubule polymer structure. $\alpha\beta$ -tubulin dimers assemble into a polar structure by the addition of GTP-bound $\alpha\beta$ -tubulin to the tip of the filament. The incorporated tubulin dimers hydrolyze to GDP-tubulin which forms the GDP lattice. The GTP cap which stabilizes the filament forms at the tip of the filament as a result of the time gap between the incorporation and the hydrolysis of the GTP. When the GTP cap is lost, the filament becomes unstable and undergoes a catastrophe. Image adapted from [129]. (C) (left) A schematic depiction of a minimal mitotic spindle in an emulsion droplet. Pulling and pushing forces are necessary for spindle alignment. (right) Reconstitution of a spindle-like structure in water-in-oil droplets. Images from [129].

copy plasmids, on the other hand, usually encode more accurate active segregation mechanisms that have been developed with an accuracy of one loss of plasmid in 10^4 cell divisions (Figure 1.3A, middle) [85]. Active DNA segregation of low-copy plasmids based on NTPase proteins is discussed further in the following paragraphs. Last but not least, indirect evidence shows that large linear DNA polymers segregate autonomously based on entropic forces produced during DNA replication (Figure 1.3A, right).

NTPase active segregation in bacteria is classified into three categories. Each system consists of at least three elements: an NTPase force-generating component, an adapter protein which mediates the interaction between the NTPase and the plasmid, and a centromere-like sequence where the adapter protein binds. Based on the NTPase protein, DNA segregation mechanisms are categorized into type I, II, and III which are Walker-A type, actin-like, and tubulin-like systems, respectively (Figure 1.3B). The Walker-A type system forms a uniform carpet of ATPase ParA proteins inside the cell.

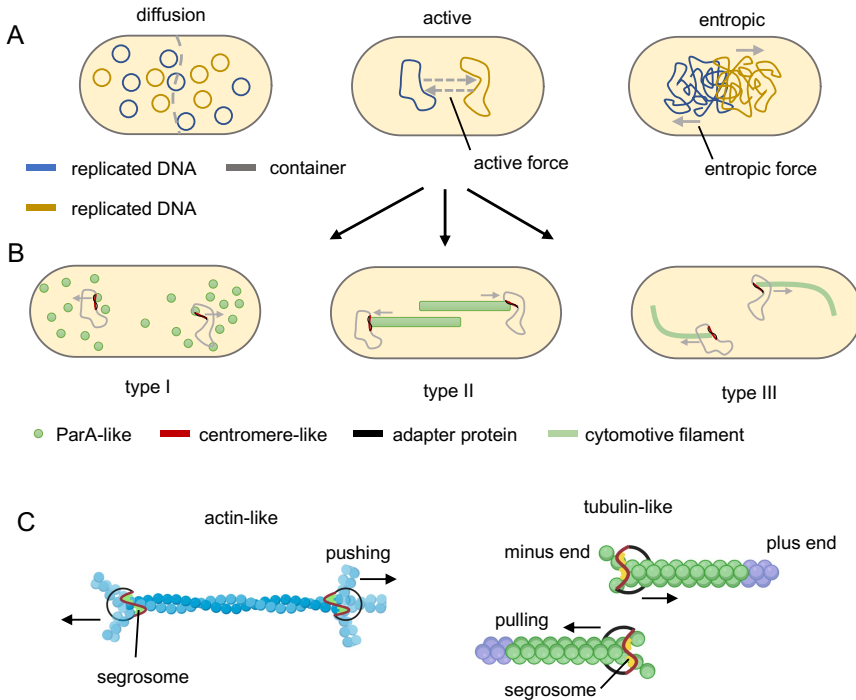


Figure 1.3: DNA segregation in bacteria: (A) A schematic depiction of various DNA segregation strategies in prokaryotic cells. (left) Brownian motion is responsible for the segregation of high-copy plasmids. (middle) For low-copy plasmids, an active force produced by NTPase proteins either pushes or pulls the plasmids towards the cell poles. (right) Large duplicated linear DNA in a confinement with a comparable size segregate intrinsically by entropic forces. (B) Different active DNA segregation mechanisms are depicted schematically. (left) A Walker A-type partitioning mechanism segregates the DNA by depletion of the ParA-like proteins during a random walk towards the cell poles (type I). (middle) Type II category contains actin-like proteins which form a minimal spindle by binding to centromere-like DNA sequence via adapter proteins. Filament growth exerts pushing forces to locate the replicated plasmids in opposite sides of the dividing cell. (right) A type III DNA segregation system which partitions the DNA by pulling the plasmids attached to the minus end of the cytomotive tubulin-like proteins via adapter proteins. (C) Schematic illustration of two minimal filament-based active DNA segregation mechanisms. On the left, an actin-like (*e.g.*, ParM) forms a cytomotive filament in the presence of ATP. Due to the interaction with two segrosomes (*e.g.*, ParRC) the filament extends from both ends and segregates the plasmids by pushing force. On the right, tubulin-like proteins (*e.g.*, TubZ) form treadmilling filaments in the presence of GTP which grow from the plus ends and shrink from their minus ends. Shrinking minus end of each filament carry a segrosome (*e.g.*, TubRC) by pulling on the complex. Created with BioRender.com.

The carpet gradually disappears towards the cell poles due to the ParA depletion by ParB. A ParBS segrosome which has formed close to the cell center jumps randomly onto the neighbouring active ParA proteins. This way the segrosome is successfully transported to the cell poles based on a random walk following a Brownian ratchet model [53, 61]. ATP-bound actin-like ParM filaments of the type II category, form in a radial arrangement around a ParRC segrosome. Since the interaction with the ParRC

complex stabilizes ParM filaments, as soon as two asters approach each other the filaments start pushing the segrosomes either by bundling or by elongation through stabilization (Figures 1.3C, left) [49, 63, 96]. The last partitioning mechanism (type III), which is the central focus of this thesis, is based on tubulin-like GTPase proteins. Bacterium or phage-encoded GTPase proteins which form filaments in the presence of GTP, segregate the DNA through a pulling mechanism. Treadmilling is a hallmark of these filaments and upon binding to the minus end of a depolymerizing filament, a segrosome will be segregated by the treadmilling filament (Figures 1.3C, right) [43, 98, 104]. Three different tubulin-like bacterial cytoskeletal proteins are studied in this thesis, two of which have been used in our attempt in building a synthetic DNA segregation system. In the following sections, a brief introduction to all these is presented.

1.5. BACTERIAL CYTOSKELETAL FILAMENTS

For years, the cytoskeleton was a hallmark of eukaryotes. However, with the development of new imaging techniques, cytoskeletal filaments have been discovered inside bacterial cells [30, 120]. Bacterial cytoskeletal filaments have been shown to engage in various activities inside cells including bacterial proliferation [1, 9, 17, 64, 96]. Tubulin-like FtsZ, which forms filamentous rings in the presence of GTP is one of the best-studied examples of prokaryotic cytoskeletal filaments and plays the main role in cell constriction which results in cell division [1]. Other cytoskeletal filaments involve in maintaining cell shape (*e.g.*, actin-like MreB) [30], intracellular organization (*e.g.*, actin-like MamK) [37], an unknown function (*e.g.*, bacterial microtubules) [31, 110], or DNA segregation as mentioned before. In this thesis we will study three tubulin-like bacterial cytoskeletal proteins namely, bTubAB, TubZ, and PhuZ.

BACTERIAL MICROTUBULES

Bacterial microtubules (bMTs) are the closest microtubule prokaryotic counterparts with about 35% sequence similarity [68]. bTubA and bTubB assemble in a head-to-tail fashion to form four-stranded hollow tubes in the presence of GTP which share some main features with MTs including dynamic instability and polarity (Figure 1.4A) [31, 33, 110]. Bacterial microtubules were discovered in *Prostheco bacter* strains where they were observed to locate mostly close to or in the stalk extension of the cell (Figure 1.4B) [110]. Although at first it was proposed that these filaments are necessary for the formation and stability of prostheca of these cells, research showed that *Prostheco bacter* strains without bMTs still display extended cell walls *i.e.*, stalks [123] which means that the function of the bMTs in their native cells remains unknown. In spite of their unknown function, significant similarity to eukaryotic MTs has made bMTs an interesting model to study.

Most of the MT functions in a eukaryotic cell are shown to be accomplished in collaboration with one or more microtubule-associated proteins or MAPs. These adapter proteins either mediate the interaction of the MTs with other cell compartments or alter their dynamics [4, 14, 62, 129]. The only known bacterial adapter protein to date is bacterial tubulin C or bTubC. bTubC has shown binding affinity to both bMTs and the

cell membrane and it has been shown to stabilize the filaments upon binding to the filament lattice [3, 31]. Distinctive characteristics of bacterial microtubules are studied more extensively in **Chapter 3** of this thesis. We have also used bMTs in combination with bTubC proteins to design a hybrid DNA segregation system which is discussed in **Chapter 4** of this thesis.

TUBZ

Type III mechanisms in the active DNA segregation subgroups include a GTPase tubulin-like protein which forms filaments that hypothetically transport replicated low-copy plasmids by pulling them towards cell poles. For instance, low-copy virulence plasmid pBtoxis of *Bacillus thuringiensis* and *Clostridium botulinum* phage c-st encode for closely related tubulin-like TubZ proteins to maintain the plasmid and the prophage during cell division, respectively [26, 82, 104]. Although the segregation with TubZ filaments has not been demonstrated experimentally in the native or host cells, over-expression of the genes in *E. Coli* has revealed treadmilling filaments inside living cells (Figure 1.4C) [82]. Moreover, a four-stranded helical structure was identified for the filaments of TubZ in the presence of GTP using cryo-EM images (Figure 1.4D, left) [97]. As mentioned before, a minimal DNA segregation system requires three components. The segregation system encoded by pBtoxis includes an adapter protein namely TubR and a centromere-like DNA sequence called tubC. In a TubZRC segregation system, the interaction between the TubZ filaments and tubC is mediated by TubR. It has been shown that the nucleoprotein TubRC complex forms a ring-like filament with multiple TubR dimers binding to the DNA sequence which can form either one or two loops (Figure 1.4D, right) [88]. *In vitro* reconstitution of the TubZRC system revealed the transportation of TubRC complex by TubZ filaments [43]. In **Chapter 4** of this thesis, we will assess the application of the TubZRC system in a synthetic cell and propose a hybrid DNA segregation system based on those results.

PHUZ

As mentioned above, phage-encoded filaments might participate in cargo transportation inside their host cell. Recently, tubulin-like proteins with distinct properties have been discovered in various *Pseudomonas* jumbo phages *e.g.*, 201 ϕ 2-1. It has been shown that these phage-encoded TubZ (PhuZ) proteins form filaments in their host cell forming a minimal spindle apparatus (Figure 1.4C) [122]. Unlike the *C. botulinum* c-st phage-encoded DNA segregation system that protects the phage DNA during the host cell division in a lysogenic cycle [104, 116], PhuZ filaments are involved in intracellular organization which enhances the phage reproduction through a lytic cycle [55]. Upon cell infection and in order to provide protection against host cell defence systems, a 3-D proteinous structure called phage nucleus forms surrounding the phage DNA [83]. The phage nucleus is then transported to the cell center by pushing PhuZ filaments [94]. It has been shown that PhuZ filaments exhibit dynamic instability in this stage [23]. Thereafter, capsids which have formed on the membrane at cell poles are carried on treadmilling PhuZ filaments to the phage nucleus for encapsidation of replicated DNA [23] (Figure 1.4E). *In vitro* reconstitution from the purified proteins showed that in the presence of GTP nucleotides, PhuZ proteins form three-

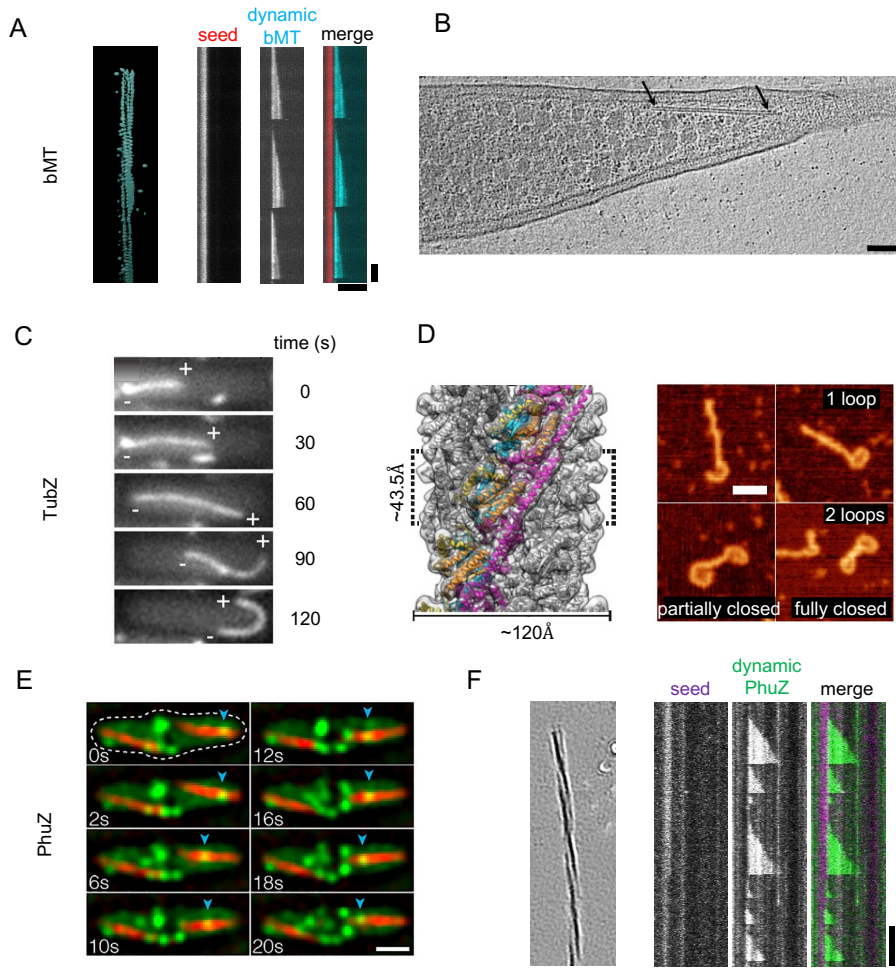


Figure 1.4: **Bacterial cytoskeletal filaments:** (A) (left) A rendered cryo-ET image of a bacterial microtubule. (right) Time versus length graphs of a dynamic bMT (cyan) which is growing from a stabilized bMT seed (red) representing the dynamic instability of bMTs. Scale bars: horizontal = 5 μm , vertical = 1 min. For more information see **Chapter 3**. (B) An EM image of bacterial microtubules in a *Prosthococcus vanneervanii* cell. The filaments are located close to the stalk of the cell and marked by arrows. Image from [110]. Scale bar = 100 nm. (C) Overexpression of TubZ filaments in *E. coli* which has resulted in formation and treadmilling of the filament along the cell. Image from [82]. (D) A cryo-EM reconstruction of a four-stranded GTP TubZ filament (left, image from [97]) and AFM images of tubC DNA segments bound to TubR proteins forming one- and two-loop structures (right, image from [88]). Scale bar = 30 nm. (E) A timelapse of the capsid (green spots) transportation along PhuZ filaments (red) in an infected cell. Image from [23]. Scale bar = 1 μm . (F) (left) A cryo-ET image of a three-stranded PhuZ filament. Scale bar = 20 nm. (right) A time-length graph of a dynamic PhuZ filament exhibiting dynamic instability in the presence of GTP. Scale bars: horizontal = 5 μm , vertical = 1 min. For more information see **Chapter 5**.

stranded helical filaments which exhibit dynamic instability, treadmilling, bundling, and polar growth (Figure 1.4F) [41].

Whilst some research has been carried out on the phage spindle and PhuZ filaments, the mechanism by which the filaments interact with their environment has not been established. In **Chapter 5** of this thesis, we will investigate the PhuZ force-generating properties and discuss some of the details about the phage spindle based on empirical evidence.

1.6. SPATIOTEMPORAL CONTROL BASED ON OPTOGENETICS

One of the most challenging phenomena which should be addressed in a synthetic cell is the spatial and temporal control of the biological processes. Chemical control methods suffer from genuine limitations. The non-permeable nature of the lipid bilayer of a vesicle may be overcome with the use of microfluidic techniques [32, 133]. Another solution to this issue would be to enhance the complexity of the system by implementing natural or artificial transporters into the membrane of the synthetic cell [46]. Additionally, external control based on proteins sensitive to light has recently emerged with various applications. This form of the interaction with biological systems is shown to be more precise, target specific, and easier to execute.

Some biological systems possess natural light-sensitive tools [117] while many other tools were developed and genetically engineered by the fusion of the functional domains of other proteins to naturally occurring photoreceptors [59, 90]. An inclusive database of "all existing non-opsin-based optogenetic switches and publications" can be found on www.optobase.org [75]. A wide range of electromagnetic wavelengths are utilized in the opto-control techniques, for instance, to regulate gene expression in bacteria [103] or cell-free systems [67] or for protein activation/deactivation in the *in vitro* assays [93, 127]. In **Chapter 4** of this thesis, we investigate the application of a blue light-sensitive optogenetic switch in our segregation system. The photo-switchable system is built based on the fusion of photoreceptors to the proteins involved in a segregation system. The DNA segregation would then be either triggered or terminated based on the photoreceptor's mechanism in use.

1.7. FORCE GENERATION BY CYTOSKELETAL FILAMENTS

Dynamic cytoskeletal polymers generate various forms of force which contribute to their distinctive roles in cells. FtsZ and actin, for instance, implement cell contraction in, respectively, bacterial and eukaryotic cells by exerting constrictive forces at the middle of dividing cells [5, 8, 17, 45]. Growing and shrinking MTs can produce forces which play a critical role in chromosome segregation and cell motility. Forces exerted by MTs have been studied *in vivo* [13, 107] and *in vitro* using devices such as optical tweezers and microfabricated barriers [54, 65, 80] (Figures 1.5A and B). Forces can alter the dynamics of MTs as well (Figure 1.5C) [62, 66, 74]. It has been shown that growing MTs can exert a pushing force which enhances catastrophes [66, 74].

Kattan et al. [69] have recently shown that growing bMTs can exert force by forming long and bundled filaments. The force is large enough to reshape giant unilamellar vesicles (GUVs). Whether this pushing affects the dynamics of bMTs is not known, however, based on their similar behavior with MTs, we hypothesized that stalling by a rigid barrier can enhance catastrophes of bMTs. To assess this hypothesis, we repeated previous barrier experiments of MTs and studied the bMT-barrier interaction, the results of which are discussed in **Chapter 3** (Figure 1.5D).

A key role of PhuZ filaments in their host cell is phage nucleus positioning. Dynamic PhuZ filaments are shown to push the phage nucleus towards the cell center while growing [23]. Moreover, as PhuZ filaments display dynamic instability similar to that of MTs and bMTs, we asked how a pushing force impacts the dynamics of these filaments. Therefore, we performed barrier experiments for dynamic PhuZ filaments as well (Figure 1.5D) and showed that in the presence of pushing forces, PhuZ filaments also encounter catastrophes more frequently (**Chapter 5**).

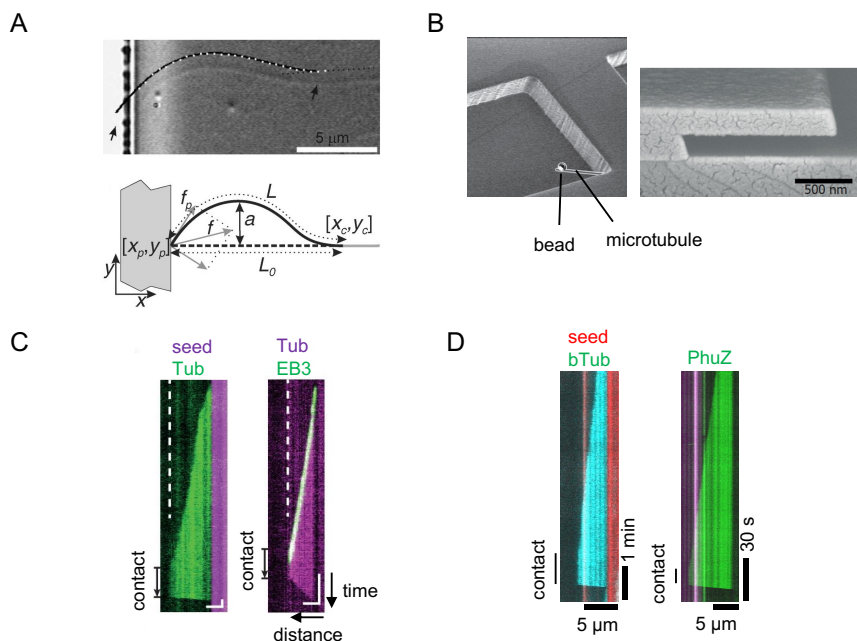


Figure 1.5: **Force generation by cytoskeletal filaments:** (A) A microscopy (top) and a schematic depiction (bottom) of a buckling microtubule during interaction with a rigid barrier which is used to measure the buckling force. Image from [65]. (B) Examples of the barriers that have been used to study force-generating MTs. images from (left) [80] and (right) [73]. (C) Position-time graph of microtubules which stall at a rigid barrier in the presence and absence of microtubule-associated protein EB3. The contact time duration is marked by arrows. Scale bars: 2 μm (horizontal) and 10 s (vertical). Image from [74]. (D) Position-time graphs of a bacterial microtubule and a PhuZ filament which encounter a stalling force against a rigid barrier. Scale bars: horizontal = 5 μm , vertical = 1 min (left) and 30 s (right). For more details about the experimental conditions see **Chapter 3** for bMTs and **Chapter 5** for PhuZ.

1.8. MICROTUBULE MODELS

As was indicated previously, a better understanding of biological processes such as mitosis is achievable by reconstitution and investigation of individual players of the system of interest. Since the discovery of dynamic instability in microtubules, several theoretical models have emerged to explain the stochastic behavior of these filaments [12, 15, 74, 109]. People have been trying to make predictions of MTs' dynamic features such as catastrophe and growth rates by the means of theoretical approaches. One of the first theoretical models which predicts the growth speed and diffusion coefficient based on the on and off rates of a 1-D polymer was published by Oosawa [106]. Later this model was successfully applied to microtubules [47]. Two dimensional models have been able to explain dynamic instability characteristics of MTs based on the estimation of the mechanical energies of the intra-lattice interactions [128], extending the number of protofilaments by generalizing a 1-D model [12], or by accounting longitudinal interactions between the terminal protofilaments that allows the single-protofilament rescues between neighboring protofilaments [15] in the expense of increased complexity. On the other hand, 1-D models were also formulated which with fewer variables and thus less complexity still could explain MTs' behavior [6, 44, 74]. In this thesis, we used a 1-D microtubule model to explain the growth and stalling times of bMTs (**Chapter 3**). This model was previously successfully applied to eukaryotic MTs [74].

1.9. THESIS OUTLINE

This thesis focuses on the dynamic principles that govern bacterial cytoskeletal filaments with a perspective to use these systems for DNA segregation in synthetic cells. The thesis is organized in the following way:

- **Chapter 2:** The second Chapter is concerned with the methodology used in this thesis. This Chapter provides an explanation of the methods and the materials used to perform the *in vitro* reconstitution studies and barrier experiments in the rest of the thesis.
- **Chapter 3:** In this Chapter we present combined experimental and computational results to compare the catastrophe dynamics of bacterial microtubules with eukaryotic ones. This work shows that a one-dimensional phenomenological model of microtubules can be employed to explain the dynamic features of the bacterial microtubules. Cryo-electron tomography images of bacterial microtubules are also presented. Furthermore, observation of bacterial microtubule doublets in the cryo-ET images provides new insights into the bundling effect of these filaments.
- **Chapter 4:** This Chapter provides a perspective on the potential use of bacterial microtubules as well as other prokaryotic cytoskeletal systems in synthetic cells based on cell-free expression in the PURE system, and the use of a light-controllable DNA recruitment. We propose to build a hybrid DNA segregation system which is composed of bacterial microtubules hooked up to cetricromeric DNA by the means of a light-inducible engineered system which is composed of

the adapter proteins bTubC and TubR.

- **Chapter 5:** This Chapter focuses on the phage-encoded cytoskeletal protein PhuZ which forms a minimal spindle in *Pseudomonas* cells upon infection. The catastrophe times of freely growing and stalling PhuZ filaments are compared to those of eukaryotic and bacterial microtubules by growing the filaments against rigid microfabricated barriers. Here we show that the interaction with a rigid barrier increases the catastrophe rate of PhuZ filaments which is consistent with the other two dynamically unstable filaments. In addition, our observations such as parallel bundling and aster formation in the presence of surface interactions which seem to be exclusive to these filaments extend our understanding of the underlying mechanism of the phage spindle.
- **Chapter 6:** This Chapter concludes the thesis and presents a brief outline of possible future research.

2

METHODS AND MATERIALS

So, express your love and pain to a degree that its trace would not scar anyone's heart.

Mahmud Dolatabadi - Kelidar

The majority of the experiments in this thesis concern the reconstitution of the system of interest utilizing essential purified proteins. Purified proteins were used to reconstitute systems in order to assess their compatibility with the cell-free assays. Bacterial microtubules and PhuZ filaments were studied by the reconstitution of their dynamic properties from the purified globular proteins in the absence and presence of rigid barriers. Most of the above-mentioned assays were imaged by either TIRF or spinning disk confocal microscopy which became feasible by fluorescent labeling of purified proteins. Specific methods and materials used in each assay are provided in each Chapter separately. More general experimental methods and materials used are explained in this Chapter. In this Chapter, we first introduce and explain the purification and labeling methods of the proteins utilized in the rest of the thesis. We then describe the steps that have been taken to fabricate rigid barriers. Dynamic assays, imaging, and image analysis methods used to study those assays are introduced next.

2.1. PROTEINS

Various proteins were used in different Chapters of this thesis. Here we introduce the proteins by explaining the purification and labeling methods. Proteins were purified and labeled in-house by Dr. Eli O. van der Sluis, Dr. Anne Doerr, Angel Goutou, or Reza Amini Hounejani. Amino acid or nucleotide sequences of the proteins are embedded at the end of this Chapter in the Supplementary Materials section. In all cases, after the purification or labeling of a protein, small aliquots were made and snap frozen in liquid nitrogen and stored in a -80°C freezer for later use. Frozen protein aliquots were thawed on ice before use.

BACTERIAL TUBULINS A AND B

Bacterial tubulins A and B (bTubA and bTubB) were used in Chapters 3 and 4 of this thesis. *Prostheobacter dejongei* bacterial tubulins A and B were co-expressed and purified following the procedure explained by Diaz-Celis et al. [33] except that vectors were overexpressed in OverExpress C41(DE3) Chemical Component Cells (Immunosource) instead of BL21(DE3). In short, following the steps of harvesting the cells, lysing, and removing the debris, the proteins went through three consecutive polymerization-depolymerization cycles using Beckman ultracentrifuges. Each cycle started with addition of 5 mM MgCl_2 and 0.5 M KCl and incubation for 10 min at 25°C . 2 mM GTP was then added to the solution and the solution was immediately centrifuged at $100\,000\times g$ for 30 min in a Type 60 Ti a Beckman rotor (273 000 rpm). The supernatant was discarded, and the pellet was resuspended with 3 mL ice-cold 50 mM HEPES-KOH pH 7 and incubated for 30 min on ice with occasional pipetting. A cycle was completed by a $100\,000\times g$ centrifuge for 30 min at 4°C in the similar rotor. The pellet was discarded, and the supernatant was warmed to 25°C for the next cycle.

The pellet of the final cycle was resuspended in 500 μl 50 mM HEPES-KOH pH 7, incubated for 30 min on ice with occasional pipetting, and aliquots of 1 μl were made. The final concentration of the protein was measured by a NanodropTM 2000 spectrophotometer at 280 nm (A280) (extinction coefficient = $103\,754.2\text{ M}^{-1}\text{ cm}^{-1}$). An overloaded Coomassie blue-stained protein gel of the two proteins is shown in Figure S1.

Purified bTubAB were labeled on their lysine residues either by biotin or Atto dyes following the procedure described by Deng et al. [31]. Inactive proteins were first discarded from the bTubAB solution by completing a polymerization-depolymerization cycle started by adding GTP and MgCl_2 to the bTubAB solution at final concentrations 2 mM and 5 mM, respectively, and incubating for 10 min at 37°C . The solution was centrifuged in a Beckmen airfuge rotor at ambient temperature at 30 psi for 5 min. The supernatant was discarded and the pellet was resuspended in buffer L (80 mM PIPES-KOH, 75 mM K-Acetate, 0.5 mM EDTA, and 0.2 mM TCEP pH 7.5). The label (in DMSO) at a ratio of 1:2 (protein:label) in the presence of 2 mM GTP was added to the solution and incubated for 30 min at room temperature. Then the mixture was supplemented by 75 mM K-Glutamate and 2 mM GTP and was gently added as a layer on top of 6 mL pre-warmed glycerol cushion (40 mM PIPES-KOH, 37.5 mM K-Acetate, 0.25 mM EDTA, 0.1 mM TCEP (pH 7.5), 20% glycerol (v/v), 75 mM K-Glutamate) and centrifuged at $100\,000\times g$ in a Type Ti 60 Beckman rotor (27 300 rpm) at 35°C for 30 min.

After removing the cushion and washing the pellet with warm MRB80 (80 mM PIPES-KOH pH 6.8, 4 mM MgCl₂, 1 mM EGTA), the pellet was resuspended in 50 μl MRB80 on ice for 10 min and centrifuged in a Beckman airfuge in a cold rotor for 5 min at 30 psi. At the end, the supernatant was collected and the concentration as well as the labeling ratio was measured with a Nanodrop™ 2000 spectrophotometer using A280 and then A500 to correct the label absorption at 280 nm. The aliquots were then snap-frozen in liquid nitrogen and stored at -80°C.

BACTERIAL TUBULIN C

The eGFP N-terminal fusion of bacterial tubulin C or eGFP-bTubC from *Prostheco bacter debontii* was used in Chapter 4 of this thesis. The protein was expressed in ER2566 strain (New England Biolabs, fhuA2 lacZ::T7 gene1 [lon] ompT gal sulA11 R(mcr73::miniTn10-TetS)2 [dcm] R(zgb-210::Tn10-TetS) endA1 Δ(mcrCmrr)114::IS10), from pET11a-6xHis-eGFP-btubC plasmid. Cells grew to an OD600 = 0.5 at 37°C at which point the expression was induced by addition of 1 mM isopropyl-β-D-thiogalactopyranoside (IPTG) (Thermo Scientific™) followed by another 3 h growth at 37°C. Cells were harvested and pelleted cells were stored at -80°C for later use.

The cell pellet was then dissolved in 1 mL B-PER™ (Bacterial Protein Extraction Reagent, Thermo Scientific™) and 10 μl of 10 mg mL⁻¹ lysozyme and 10 μl DNase I (1 U/μl) and incubated for 10 min at room temperature. The solution was centrifuged at 16 000×g for 20 min at 4°C. The pellet was resuspended in 2 mL 1:10 B-PER (in MilliQ) and centrifuged at 16 000×g for 15 min at 4°C. The last two steps were repeated two more times. Next, the pellet was resuspended in 600 mM Tris-HCl pH 8.0 containing 0.6 M

guanidinium-HCl and incubate for 30 min at room temperature and then centrifuge at 16 000×g for 20 min at 4°C once more. A mini-NiNTA spin column was equilibrated with 10 mM Tris-HCl pH 8.0 containing 0.6 M guanidinium-HCl. The supernatant was loaded and then reload flow-through two more times to the column. The column was washed two times with 600 μl 10 mM Tris-HCl pH 6.3 and 8 M urea and eluted in three fractions with 200 μl 10 mM Tris-HCl pH 6.3 and 8 M urea containing 400 mM imidazole. An overnight dialysis was done for 4 h against 20 mM HEPES-KOH pH7.6, 200 mM NaCl, and 1 mM MgCl₂. Using Bradford assays the concentration was measured and smaller aliquots were made. A Coomassie blue-stained protein gel with the purified protein is shown in Figure S1.

TUBZ AND TUBR

Proteins of *Bacillus thuringiensis* partitioning system encoded on pBtoxis plasmid *i.e.*, TubZ and TubR were expressed and purified essentially as described by Fink and Lowe [43] from plasmids pTXB1-BtTubZ and pOPINS-His₆-SUMO-BtTubR, respectively, that were kindly provided by Prof. Jan Löwe and were used in Chapter 4 of this thesis. In short, intein-tagged TubZ and sumo-tagged TubR proteins were expressed in *E. coli* ER2566 cells supplemented with the Rosetta™ 2 plasmid. Proteins were then purified using affinity column and after elution, ion exchange and size exclusion chro-

matography was used to enhance the purification further. The purification of TubZ was followed by a polymerization-depolymerization cycle to remove inactive proteins. The concentration of each protein batch was determined by a NanodropTM 2000 spectrophotometer at 280 nm.

2

bTUBC-iLID AND SspB-TubR

The hybrid system optogenetics tool which includes bTubC from *P. debontii* on the one hand and TubR from *B. thuringiensis*, on the other hand, was used in the DNA segregation module in Chapter 4. The photo-sensitive proteins were designed by fusion of iLID to bTubC (forming bTubC-iLID construct) and SspB to TubR (forming SspB-TubR construct). Both fusion proteins were expressed in *E. coli* ER2566 cells supplemented with the RosettaTM 2 plasmid.

The fusion protein bTubC-iLID was expressed with an N-terminal His₈-tag followed by a DYDIPTT linker and a 3C protease recognition site, and contained GCN4 leucine zipper for dimerization at the fusion point (plasmid pED76). Expression was induced with 0.2 mM IPTG after cooling the cells for 30 minutes on ice, and continued overnight at 18°C. Cells were harvested, washed in PBS, lysed by passing through a microfluidizer (20 kpsi) in buffer A (20 mM HEPES-NaOH pH 7.5 (at 20°C), 200 mM NaCl, 5% (w/v) glycerol, 0.05 mM TCEP), and membranes were removed by centrifugation at 40,000 rpm in a Ti45 rotor. After affinity purification using Talon Superflow beads, bTubC-iLID was eluted with 3C homemade protease, concentrated using a Vivaspin 30 kDa ultrafiltration device, and further purified by size exclusion chromatography on a Superdex Increase S200 10/300 column (Cytiva).

The fusion protein SspB-TubR was expressed with an N-terminal MBP-tag followed by a 3C protease recognition site and a GGGGATAGAGG linker at the fusion point (plasmid pED75), and expression was induced with 1 mM IPTG and continued for 3 hours at 37°C. Cell lysis and two-step purification was performed as described above for bTubC-iLID, using amylose resin (New England Biolabs) instead of Talon.

If applicable, proteins were fluorescently labeled on their cysteine residues by maleimide reagents (0.1 mM, 30 minutes room temperature) prior to size exclusion chromatography.

PHUZ

PhuZ was purified according to an adjusted version of the procedure reported by Erb et al. [41], Kraemer et al. [77] and used in Chapter 5 of this thesis. Briefly, before the cell lysate was added, the matrix (TALON[®] SuperflowTM (Cytiva)) was equilibrated in a column with PhuZ buffer (50 mM HEPES-KOH pH 8.0, 250 mM KCl, 1 mM MgCl₂, 10% glycerol and 1 mM β-mercaptoethanol). After addition to the column, the cell lysate was incubated on a spinning wheel at 4°C for one hour. 10 mM imidazole in PhuZ buffer was then added to the resin to remove non-specifically bound proteins. Subsequently, 125 mM imidazole in PhuZ buffer was added to the resin to elute the PhuZ proteins. To cleave the 6-His-tag, 3C protease was added to the solution and incubated overnight at 4°C in a 10k MWCO Slide-A-LyzerTM Dialysis Cassette (Thermo Scientific)

in buffer composed of 50 mM HEPES-KOH pH 8.0, 250 mM KCl, 1 mM MgCl₂, 10% glycerol. The solution was added once more to the resin and the flow-through was collected. Purified PhuZ was then concentrated using Vivaspin ultrafiltration device.

PhuZ proteins were labeled with PEG-biotin, Cy3, or Cy5 following the procedure explained by Erb et al. [41].

2.2. MICRO-BARRIER FABRICATION

Micro-barriers were fabricated by adapting the procedure used by Kok et al. [74] and were used in Chapters 3 and 5 of this thesis. The process is schematically depicted in Figure 2.1. The procedure starts by cleaning 24×24 mm coverslips in a base piranha solution containing H₂O₂:NH₄OH:H₂O with 1:1:5 ratio at 75°C for 10 min. Clean coverslips were transferred to a cleanroom (van Leeuwenhoek Laboratory, NanoLab NL) using boxes cleaned with ethanol and dried using N₂ air. Using a plasma-enhanced chemical vapour deposition (PE-CVD) machine (Oxford Instruments PlasmaPro 80), three layers were coated on each coverslip at 300°C: first a SiC layer of about 10 nm, then a SiO₂ of about 100 nm and on top of all, a SiC layer of about 250 nm (for more details about the process parameters including different gas pressures see Table 2.1 in [73]). For the next step, we transferred the barrier pattern using photolithography starting with the spin-coating deposition of hexamethyldisilazane (HMDS) at 5000 rpm for 55 s. The deposition was followed by a soft bake at 115°C for 2 min. Subsequently, a layer of positive photoresist S1813 was coated in the same manner and soft-baked for 90 s at 115°C. The 2D pattern of the barriers was transferred to the photoresist by a near-UV source ($\approx 13 \text{ mW/cm}^2$) for 5 s (EVgroup EVG 620). Part of the pattern can be seen in a bright-field image of the barriers in Figure 2.2A. The photoresist was developed by MF321 for 1 min and rinsed for 30 s in distilled water immediately. Afterwards, the photoresist-free surfaces were etched by utilizing a reactive ion etching (RIE) system (Sentech Etchlab 200) with a gas mixture of 50:2.5 sccm for CHF₃:O₂ for 1180 s. The chamber pressure and the RF generator power were set to 50 μ bar and 50 W, respectively. The bias voltage was 200 V, as a result. Using interferometry techniques, etching rates were measured about 0.26 nm/s and 0.2 nm/s for SiC and SiO₂, respectively. The remaining photoresist was removed either by wet or dry cleaning. The wet cleaning was done by sonication of the samples in Acetone for 10 min and subsequently for 5 min in water, and for dry cleaning we used oxygen plasma at 600 W and oxygen pressure of 600 sccm for 1 h. As the wet cleaning was not always reliable and left photoresist residues on the sample, we cleaned some of the samples with dry cleaning. However, by dry cleaning, we observed that wrinkles had formed at the overhang of some of the samples, possibly due to the heat produced by oxygen plasma in the chamber (Figure 2.2D). Both forms of barriers were used in the experiments. At the end, by etching through the exposed SiO₂ layer by dipping into buffered hydrofluoric acid (HF:NH₄F with ratio 12.5:87.5%; also known as buffered oxide etchant, BOE) 10:1 for 5 min an overhang of about 1.5 μ m was created (Figure 2.2C and D).

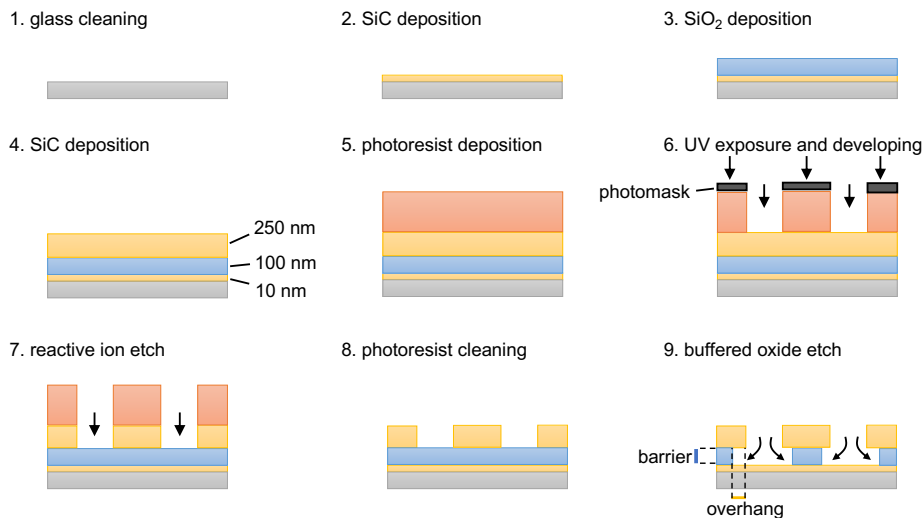


Figure 2.1: **Procedure for micro-barriers fabrication:** (1) Coverslips were cleaned using base piranha and transferred to the cleanroom. (2-4) Three consecutive sputtering coating steps were taken to coat the SiC and SiO₂ layers in the same machine and in the same temperature (300°C). (5) Spin-coating technique was then used to coat a thin layer of S1813 positive photoresist on top of the layers. We spin-coated a thin layer of HMDS prior to the photoresist coating in order to increase the stickiness of the photoresist and SiC surfaces. (6) The 2D pattern of the channels was then transferred to the photoresist by UV exposure utilizing a chromium photomask. UV exposure softened the photoresist which was then removed by MF321 developer. (7) Then we used a CHF₃ ion etching machine to etch through the SiC and probably partially through SiO₂. (8) Next, the photoresist was cleaned either with dry or wet cleaning techniques. (9) Finally, using BOE etching buffer, we etched through the SiO₂ layer to create the desired barriers with a special overhang.

2.3. STALLING ASSAY FLOW CELL PREPARATION

Stalling of a cytoskeletal filament is a situation in which the growth of a filament is abolished. In this thesis, we evoke stalling by using rigid fabricated barriers described in section 2.2. Therefore, in our experiments, stalling is specifically assigned to a situation in which a filament neither grows nor shrinks in a close-to-perpendicular contact with a rigid barrier. To study stalling features of prokaryotic filaments which exhibit dynamic instability *i.e.*, bacterial microtubules (Chapter 3) and PhuZ filaments (Chapter 5), rigid micro-barriers were fabricated on glass coverslips and were used in fluorescence microscopy assays according to what is described by Kok et al. [74]. To make flow cells, coverslips with barriers were cleaned with oxygen plasma at a power of 50 W and oxygen pressure of 200 mbar for 5 min. Then, using double-sided sticky tape, a 10 μ l flow chamber was made on a glass slide with barriers being perpendicular to the flow direction. The chamber was functionalized in three consecutive wash steps: first with 0.2 mg mL⁻¹ PLL-PEG-biotin (20%) (SuSoS, Switzerland), then 0.2 mg mL⁻¹ NeutrAvidin (Invitrogen) and finally with 0.5 mg mL⁻¹ κ -casein (Sigma) all in MRB80 (80 mM PIPES-KOH, 4 mM MgCl₂, 1 mM EGTA, pH 6.8) and with an incubation time of 10 min at room temperature per step. The channel was rinsed with 20 μ l of MRB80 after each incubation and at the end with 20 μ l of 0.2% methylcellulose in MRB80. Af-

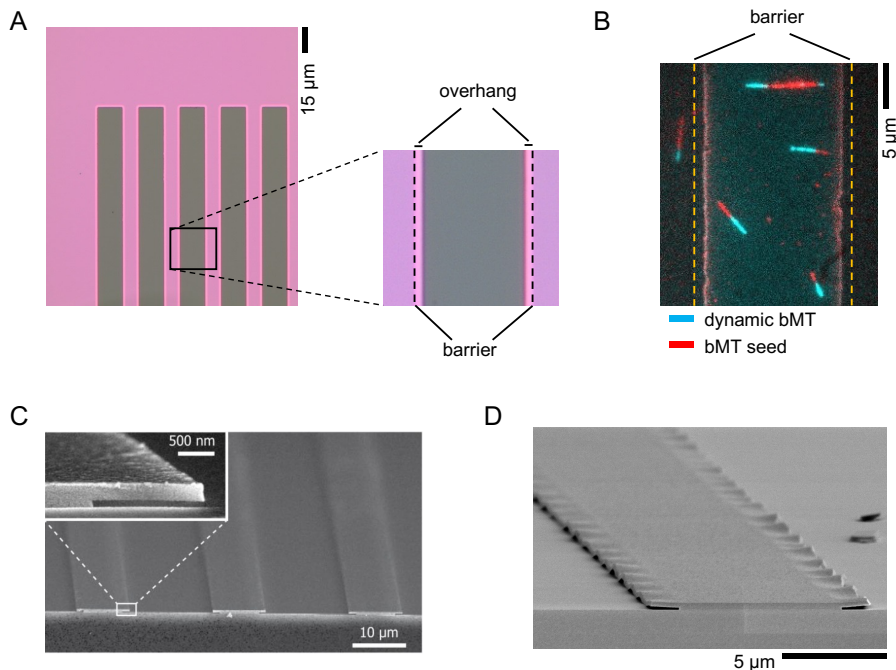


Figure 2.2: Barriers in different scales: (A) A bright-field image of a coverslip with barriers. Barriers and the overhangs are marked in the zoom-in image. The reaction happens in the dark green area where filaments are grown towards barriers and underneath overhangs. (B) An example of a TIRF image of bacterial microtubules in a flow chamber containing barriers. Bacterial microtubule GMPCPP seeds (red) are immobilized on the glass surface and the GTP dynamic bMTs (cyan) grow from them. (C) A scanning electron microscopy (SEM) image of the barriers. The inset shows a zoom-in of a barrier equipped with an overhang. The figure is adapted from [74]. (D) Overhangs of some of the barriers were wrinkled probably due to the high temperature of the oxygen plasma chamber during the dry cleaning of photoresist. The figure depicts the wrinkled barriers in a SEM image. Since there is enough room for filaments to grow underneath the wrinkled overhangs, we believe that the effect is negligible.

terwards, 20 μl of seed mixture (see Chapter 3) was added to the chamber and incubated for 10 min at room temperature in dark. Then, not adhered seeds were removed by rinsing the channel two times with warm (37°C) washing buffer (0.4 μM bTubAB, 2 mM GTP, and 0.2% methylcellulose in MRB80) to prevent seed breakage and seed depolymerization. The channel mix was added, and the sample was sealed with vacuum grease and imaged immediately afterwards. In the case of PhuZ stalling assays, following the Neutravidin incubation, the channel was rinsed two times with the imaging buffer (BRB80 (80 mM PIPES-KOH, 1 mM MgCl₂, 1 mM EGTA) pH 7.2, 0.5 mg mL⁻¹ κ-casein, 100 mM KCl, 0.5% methylcellulose) and incubated for 10 min at room temperature. Then 20 μl seeds (see Chapter 5) were added and incubated for 5 min also at room temperature in the dark. The channel was rinsed with warm (37°C) imaging buffer afterwards and the channel mix was added subsequently, sealed and imaged immediately. In both cases, the sample preparations containing proteins were con-

ducted on ice and in the final step the channel mixes were added to seeds after warming up in hand.

2

2.4. FLUORESCENCE IMAGING

Fluorescence imaging was performed with two main setups. All of the dynamic assays on a surface were imaged with total internal reflection fluorescence (TIRF) setups and image acquisition of the assays including liposomes were done with a spinning disk confocal setup. The TIRF system utilized a FRAP/TIRF Ilas² system (Gataca Systems). The spinning disk confocal setup, on the other hand, was equipped with a Yokogawa CSU-W1-T2 confocal scanner unit and utilized similar emission filters. Image acquisitions were controlled utilizing MetaMorph software (Molecular Devices). All the images were acquired using an inverted Nikon Eclipse Ti-E microscope while the Nikon Eclipse Ti2 was used for PhuZ dynamic assays. Both were equipped with a perfect focus system and a Nikon Plan Apo λ 100 \times NA 1.45 oil immersion objective which was equipped with an extra lens that increases the magnification by 1.5 \times . An Evolve 512 EMCCD camera (Photometrics) was used for image acquisition in bMT stalling assays (Chapter 3), liposome assays and general dynamic assays (Chapter 4) and an iXon Ultra 897 EMCCD camera (Oxford instruments Andor) in PhuZ stalling assays (Chapter 5). To improve the stability of the fluorescent dyes, an oxygen scavenging system composed of 4 mM DTT, 200 $\mu\text{g mL}^{-1}$ catalase, 400 $\mu\text{g mL}^{-1}$ glucose oxide, and 50 mM glucose was used in all assays involved in fluorescence imaging.

2.5. ANALYSIS OF FILAMENT DYNAMICS

Fluorescence microscopy images were analyzed using either Fiji or ImageJ (<https://imagej.net>) and custom-written MATLAB or Python codes. General quantitative analysis procedure for dynamic assays is explained in this section, while details about more specific image analysis for other assays will be provided in each Chapter. Stacks of images were subject to a drift which was removed prior to any quantitative analysis using a custom-written MATLAB script (Figure 2.3A). To measure dynamic features including growth and shrinkage velocities, catastrophe frequency and the lifetime of growing or stalling filaments, a space-time plot called kymograph was constructed for each filament using an ImageJ plugin namely KymoResliceWide (<https://imagej.net/plugins/kymoreslicewide>) by drawing either a straight or a segmented line with a constant width of 9 pixels (Figure 2.3B). Then, by measuring the filament tip distance from the tip of the seed over time, we measured the growth or shrinkage rates of the filament (Figure 2.3B). The growth speed is reported as a weighted average which is both time-averaged and ensemble-averaged and the statistical error is the standard error of the mean which is the standard deviation divided by the square root of ensemble size. Catastrophe frequency is defined as the total number of catastrophes divided by the total growth time of a filament. To exclude random negative excursions from the catastrophe data a minimum shrinkage length was considered for a catastrophe. The error was calculated as the catastrophe frequency divided by the square root of the number of observations. Growth time, on the other hand, is defined as the time a filament spends in the growing state before it undergoes a catastrophe.

The growth time and catastrophe of the filaments which were not completely visible (partial filaments) in one kymograph were discarded from the dataset (Figure 2.3B). Growth time for the filaments was reported as the mean and the standard error of the mean as the statistical error. In addition, where necessary kymographs of the filaments which were composed of more than one filament *i.e.*, bundles were removed from the data by finding the uneven changes in the intensity of a growing filament by eye (Figure 2.3C).

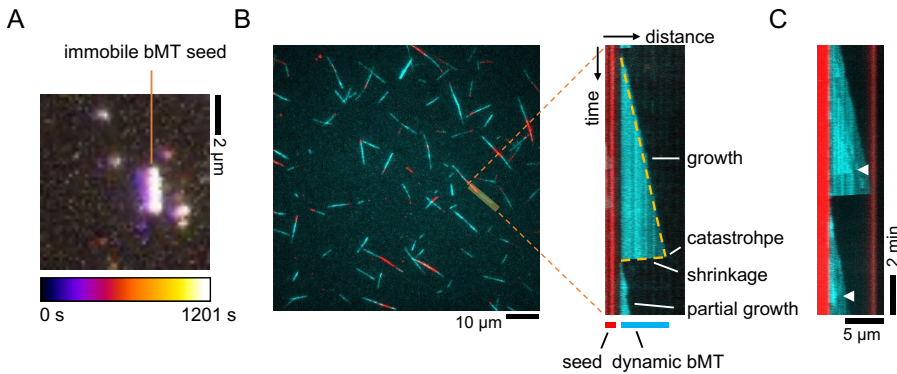


Figure 2.3: **TIRF image analysis to measure filaments dynamics:** (A) A color-coded temporal projection of a bMT seed before drift removal. (B) A TIRF image of bacterial microtubules in a flow chamber (left). For dynamic data analysis, kymographs were built for multiple filaments per field of view (right). A space-time plot named kymograph (right) shows a bMT (cyan) growing from a seed (red). The filament undergoes a catastrophe when it experiences a stochastic shrinkage. Datasets including lifetimes of the filaments include only complete events meaning that partial growth events were discarded. (C) A kymograph of a bundle of bMTs. The arrowheads represent the changes in the intensity which illustrate the formation of a bundle.

ACKNOWLEDGMENTS

We thank Nemo Andrea for his technical assistance on SEM imaging of the barriers.

SUPPLEMENTARY MATERIALS

2

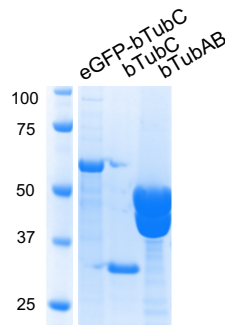


Figure S1: Protein gel of a SDS-PAGE for bTubA, bTubB, and bTubC proteins.

Amino acid sequence of bTubA-dejongei

MKVNNTIVVSIGQAGNQIAASFWKTVCLEHGIDPLTGQTAPGVAPRGNWSSFFSKLGES
SSGSYVPRAIMVDLEPSVIDNVKATSGSLFN PANLISRTEGAGGNFAVG YLGAGREVLPEV
MSRLDYEIDKCDNVGGIIVLHAIGGGTGSGFGALLIESLKEKYGEIPVLSCAVLPSPQVSSV
VTEPYNTVFALNTLRRSADACLIFDNEALFDLAHRKWNIESPTVDDLNL LITEALAGITAS
MRFSGFLTVEITLRELLTNLVQP SLHFLMCAFAPLTPPDRSKFEELGIEEMIKSLFDNGS
VFAACSPMEGRFLSTAVLYRGIMEDKPLADAALAAMREKLPLTYWIPTAFKIGYVEQPGIS
HRKSMVLLANNTEIARVLD RICHNFDKLWQRKAFANWYLN EGMSEEQINVL RASAQEL
VQSYQVAEESGAKAKVQDSAGDTGMRAAAAGVSDDARGSMSLRDLVDRRR*

Amino acid sequence of bTubB-dejongei

VREILSIHVGQCGNQIADSFWR LALREHGLTEAGTLKEGSNAAANSNMEVFFHKVRDG
KYVPRAVLVDLEPGVIARIEGGDMSQLFDESSIVRKIPGAANNWARGYNVEGEKVIDQIM
NVIDSAVEKTKGLQGFLMTHS IGGGSGSGLGLSLILERLRQAYPKKRIFTF SVVPSPLISDSA
VEPYNAILTLQRILDNADGAVLLDNEALFRIAKAKLNRSPNYMDLNNI ALIVSSVTASLRF
PGKLN TDLSEFVTNLVFPGNHFLTASFAPMRGAGQEGQVRTNF PDLARETFAQDNFT
AAIDWQQGVYLAASALFRGDVKAKVDENMATIRKSLNYASYMPASGGLKLG YAEETAPE
GFASSGLALVNHTGIAAVFERLIAQFDIMFDNHAYTHWYENAGVSRDMMAKARNQIAT
LAQSYRDAS*

Amino acid sequence of eGFP-bTubC-debontii

HHHHHHSSGLVPRGSH MVSKGEELFTGVVPILVELDGDVNGHKFSVSGEGEGDATY
GKLT LKFICTTGKLPVPWPTLVTTLYGVQCFSRYPDHMKQHDFFKSAMPEGYVQERT
IFFKDDGNYKTRAEVKFEGD TLVNRIELKGIDFKEDGNILGHKLEYNYN SHNVYIMADK

QKNGIKVNFKIRHNIEDGSVQLADHYQQNTPIGDGPVLLPDNHYLSTQSALS KDPNEKR
 DHMVLLLEFVTAAGITLGMDELYKSGVDSPLDRQLAAASRSVVEARRMAYHDDSKIGYLV
 EQISVLADLRQKEGDFRKAESLYREALFSAQEQRKPDPELLTGIHSLLAHLYDRWGRMD
 LASQFYEKALKIAERGGIAQSDKVAIKNLMLAMIFKQLRDYTRAEQHYQEAL EIFRKT DGE
 YSARVASVFNNLGVLYSNLEVEQAQEMHEHALTIRQSLNSNDQADSGDLSQTYINLGAV
 YKAAGDFQKAEACVDRAKLRASMNNGYHPQPRRAASLLVDKSL*

2

Amino acid sequence of TubZ

MLLNSNELEHIHSTNHSVNDISIRWGVIGAGQKGNKEADLFAGYKFSNGTTTCYPTLAV
 NFAESDMMHLQNIKEDRIHFDGLKGAARTPSVVTDLDFDPETNPANANGYLDKLAQELG
 RKFTNEEGEVVDQFLICLGAGGGVGTGWGSLVLQLIREQFFPCPVMSLISLPSGDPDEI
 NNALVLLSEIDEFMREQDRLFGNSDIKPLANVIVNDNTQMQRIIESQKGTKDLKNRYVN
 WKEVANDNVVSTLHEINIIPENYGSNDVNTYDPSDLIKLLSIPGRFLTIGKARIAKFDLHSL
 NSIKRSLDEGFFSAEHQFETATMYGGFVLRPSNADFFKDVNTENRIRNTLGEYKRLDEIA
 GKFGDPIWDNEYAVCYTIFAGMTMPKRYISLAREGKELAEKQEQLRAEAQRKQDEEKVD
 ISFATNRVQKNTFNPYNKNQGGFSGASRFSGGKNSAFKRQTSEATSTQNQQEEENIISTL
 KTSNPFKKR GSSCITGDALVALPEGESVRIADIVPGARPNSDNAIDLKVLDRHGNPVL
 DRLFHSGEHPVYTVRTEGLRVTGTANHPLLCLVDVAGVPTLLWKLIDEIKPGDYAVIQR
 SAFSVDCAGFARGKPEFAPTTYTVGVPLVRFLEAHHRDPDAQAIADELTDGRFYAKV
 ASVTDAGVQPVYSLRVDTADHAFITNGFVSHATGLTGLNSGLTTNPGVSAWQVNTAYT
 AGQLVTYNGKTYKCLQPHTSLAGWEPSPALWQLQ*

Amino acid sequence of TubR

HHHHHHGSDSEVNQEAKPEVKPEVKPETHINLKVSDGSSEIFFKIKKTTPLRRLMEAFA
 KRQ GKEMDSLRFYDGIQADQTPEDLDMEDNDIIEAHREQIGG MNRDHFYTLNIA
 EIAERIGNDDCAYQVLMAFINENGEAQMLNKTAVAEMIQLSKPTVFATVNSFYCAGYID
 ETRVGRSKIYTLSDLGVEIVECFKQKAMEMRNL*

Nucleotide sequence of PhuZ

ATGAGGGGATCACATCACCACCATCACCACCTTGGAGGTTCTGTTCAG GGTCCGC
 CTGTTAAAGTGTGCCTGATTTTTGCGGGTGGTACAGGCATGAATGTCGCAACCAAGC
 TGTTGACTTGGGTGAGGCTGTGCATTGTTTTGATACGTGCGATAAAAACGTGGTGG
 ATGTGCACCGCTCTGTTAACGTGACTTTGACCAAAGGCACTCGTGGTGC GGGTGGCA
 ATCGTAAGGTGATCCTGCCACTGGTCCGCAAAATCCGGCACTGATGGATACGA
 TTCCGGAGGCTGACTTCTACATCGTGTGTATAGCCTGGGCGGCGGTTCCGGTTCTG
 TTCTGGGCCCACTGATCACC GGCCAACCTGGCGGATCGTAAGGCAAGCTTCGTGAGC
 TTCGTTGTAGGTGCTATGGAATCGACCGACAACCTGGGGAATGATATTGATACGATG
 AAGACTCTAGAGGCGATCGCGGTCAACAAACACCTGCCGATTGTTGTGA ACTACGTT
 CCGAATACCAAGGTAGAAGCTATGAAAGTATTAATGATGAGATCGCAGAGAAAATTC
 GCAAGGTCTGTGTTGTAGTAAACCAAACACCGCCGGTTAGACGTT CATGATGTGC

CCAAC TGGGTTCGTTTCACCGACAAGCACAATTA CTTGATCCCGCAGGTTTGCGAAC
TGCACATTGAAACCACCCGTAAGGACGCGGAAAACGTCCCGGAGGCCATCTCCAGC
TGAGCCTGTATTTGGATCCGTCTAAAGAAGTGGCCTTTGGCACCCCGATCTACCGCA
AAGTTGGTATTATGAAGGTCGATGACCTTGACGTGACGGACGACCAGATTCATTTG
TTATCAACAGCGTGGGCGTTGTGGAAATCATGAAGACCATCACCGACTCCAAACTCG
AAATGACCCGTCAGCAGAGCAAATTCACCCAACGTAACCCGATCATCGATGCGGACG
ACAACGTGGACGAGGACGGTATGGTCGTTTAA

3

DYNAMIC INSTABILITY OF FORCE-GENERATING BACTERIAL MICROTUBULES

Reza AMINI HOUNEJANI, Vladimir A. VOLKOV, and Marileen DOGTEROM

It has been recently reported that microtubules are not unique to eukaryotic cells. Prothecobacter bacteria have been shown to encode tubulin counterparts which in vitro are shown to display dynamic instability and have a GTP-enriched cap that stabilizes the microtubule, two significant features of eukaryotic microtubules. In this Chapter, we hypothesize that studying the dynamic behavior of bMTs and comparing them to microtubules may provide a more profound insight into the dynamic behavior of their more complex counterparts. Therefore, we repeated a series of experiments presented for microtubules using bacterial microtubules and asked whether the results point to similar behavior. We used microfabricated barriers along with TIRF microscopy where the results revealed that similar to microtubules, the catastrophe rate of bacterial microtubules increases when their growth is stalled by a rigid barrier. Additionally, we found that the lifetime distribution of both free and stalled bacterial microtubules can be fitted using a simple one-dimensional model that we introduced for microtubules previously. Using cryo-electron tomography images of bacterial microtubules, we showed that bacterial microtubules may form structures we call bacterial microtubule doublets which in eukaryotes are solely observed for axonemal microtubules.

3.1. INTRODUCTION

In eukaryotic cells, microtubules (MTs) are hollow cylindrical polymers that play essential roles in various cellular activities including cell division, cell motility and intracellular transport (reviewed in [4, 57]). Microtubules alternate between growing and shrinking states *in vitro* and *in vivo*, a phenomenon known as dynamic instability [18, 95]. Microtubules grow by the addition of GTP-bound tubulin to their ends. Subsequential hydrolysis of tubulin-bound GTP leads to a microtubule lattice that is primarily composed of GDP-bound tubulin, a situation that is inherently unstable. A growing microtubule may switch to rapid shrinking in an event termed a catastrophe when a stabilizing cap that is rich in unhydrolyzed GTP is lost from the microtubule end [57, 129]. The exact nature, as well as the size of the stabilizing cap, is still a topic of debate despite a long series of experimental and modeling efforts [38, 74, 92, 113, 114, 134].

Although dynamic instability is a hallmark of eukaryotic microtubules, prokaryotic tubulin-like filaments have recently been shown to display dynamic instability as well. Bacterial microtubules were for example discovered in some *Prostheco bacter* species, [31, 68, 110, 131]; other examples include DNA partitioning TubZ proteins and PhuZ filaments from various bacteriophages [41, 77, 135]. Among these examples, bacterial tubulin bTubA and bTubB show the highest sequence similarity to eukaryotic α - and β -tubulin [118], hence the use of the term bacterial microtubules or bMTs. In analogy to eukaryotic MTs, it is proposed that a GTP-cap stabilizes growing bMTs and the filaments exhibit a catastrophe when the GTP-cap is lost [31]. This dynamic behavior has been reproduced *in vitro* [31], although it is currently unknown whether it also occurs *in vivo* and what is its biological role [33, 69]. Unlike eukaryotic microtubules, which consist of typically 13 protofilaments, bMT only consist of 4-5 protofilaments (Figure 3.1A) [31, 110].

In this paper, we hypothesize that the process that triggers catastrophes in eukaryotic and bacterial MTs may be based on the same basic molecular principles, and that a bMT may ‘simply’ behave as a MT with fewer protofilaments. Studying the dynamic behavior of dynamic bMTs may thus, in addition to its intrinsic interest, provide insight into the dynamic behavior of the structurally more complex eukaryotic MTs. We, therefore, decided to repeat a series of experiments we recently presented for eukaryotic MTs and ask whether the results of catastrophe statistics can be reconciled using a simple 1-D model that we have previously introduced for eukaryotic MTs [74]. In this model, MT growth is presented as a simple one-dimensional process where the size of a stabilizing cap depends on both growth fluctuations of the tip (allowing also for negative growth excursions) and the rate of hydrolysis of tubulin-bound GTP incorporated in the lattice. A MT undergoes a catastrophe when the cap is lost due to either or both processes.

Using microfabricated barriers, we measured the catastrophe statistics both for freely growing bMTs and for force-generating bMTs whose growth was stalled by a rigid barrier. By fitting both datasets using our 1-D model, we obtained values for the two main fitting parameters of the model: the random GTP hydrolysis rate in the bMT lattice,

K_{hyd} , and the effective diffusion constant describing noisy filament growth, D_{tip} . While K_{hyd} was similar to what we found for MTs, D_{tip} was smaller than previously found for (faster-growing) MTs [74]. Unlike what was previously reported [31], we find no evidence for an age-dependency of the bMT catastrophe rate. In addition, we examined the end-structures of dynamic bMTs using cryo-ET and found tapered ends that show similarity to growing MTs. Interestingly, using cryo-ET we also discovered the existence of bacterial microtubule doublets bMTDs, which may explain the frequent observation of bMT bundles both *in vivo* [110] and *in vitro* [33, 118, 121].

3.2. RESULTS

DYNAMIC PROPERTIES OF FREE BACTERIAL MICROTUBULES

To assess the dynamics of bacterial microtubules, the surface of a flow chamber was passivated and GMPCPP-stabilized seeds were immobilized using PLL-PEG-biotin and NuetrAvidin. A mixture of $0.88 \mu\text{M}$ (10:1 unlabeled:labeled) purified bTubAB was then added to the flow chamber and was imaged at 20°C using total internal fluorescence (TIRF) microscopy (Figure 3.1A, bottom). In the absence of physical constraints, bMTs were polymerizing and depolymerizing freely (Figure 3.1B and C). We obtained growth dynamics of the filaments by locating the tips of the filaments at 1 s time intervals. Analysis revealed that the average growth velocity and catastrophe frequency of free bMTs were $0.58 \pm 0.02 \mu\text{m min}^{-1}$ (mean \pm SEM) and $0.35 \pm 0.02 \text{ min}^{-1}$, respectively (Table 3.1). The catastrophe frequency is calculated by dividing the total number of observed catastrophes by the total observed growth time of the bMTs, where the statistical error is obtained by dividing the frequency by the square root of the number of events (assuming a random catastrophe process). The catastrophe time or growth time, on the other hand, is defined as the time an individual bMT spends growing from nucleation until the filament undergoes a catastrophe (Figure 3.1C). The growth time distribution of free bMTs was observed to follow an exponential function instead of a gamma function (shape parameter > 1) as was reported by Deng et al. [31]: fitting revealed an exponential time scale of $209 \pm 19 \text{ s}$ (mean \pm SD) (Figure 3.1D; see also Figure S2).

DYNAMIC PROPERTIES OF STALLED BACTERIAL MICROTUBULES

To better understand the contribution of the GTP cap to the stability of bMTs, we constrained their growth using rigid barriers, using an experimental approach we have previously developed for eukaryotic MTs [74]. The barriers were fabricated on glass coverslips which were then used to make flow chambers. Barriers consisted of a SiO_2 layer of about 100 nm in thickness, with a SiC overhang to increase the chance for the filaments to interact with the barriers (Figure 3.2A and B). bMTs which had (near-)perpendicular physical contact with the barriers, were observed to stop growing (stall), buckle, or slide (depicted in Figure 3.2C – left, middle, and right, respectively). Sliding refers to an occasion in which a filament continues growing while sliding on the wall. Buckling, on the other hand, occurs when a filament endures its growth while hinged at a point on the wall. Sliding and buckling were often followed by the breaking of the filament. The frequency of observation of each of these events is shown in Figure

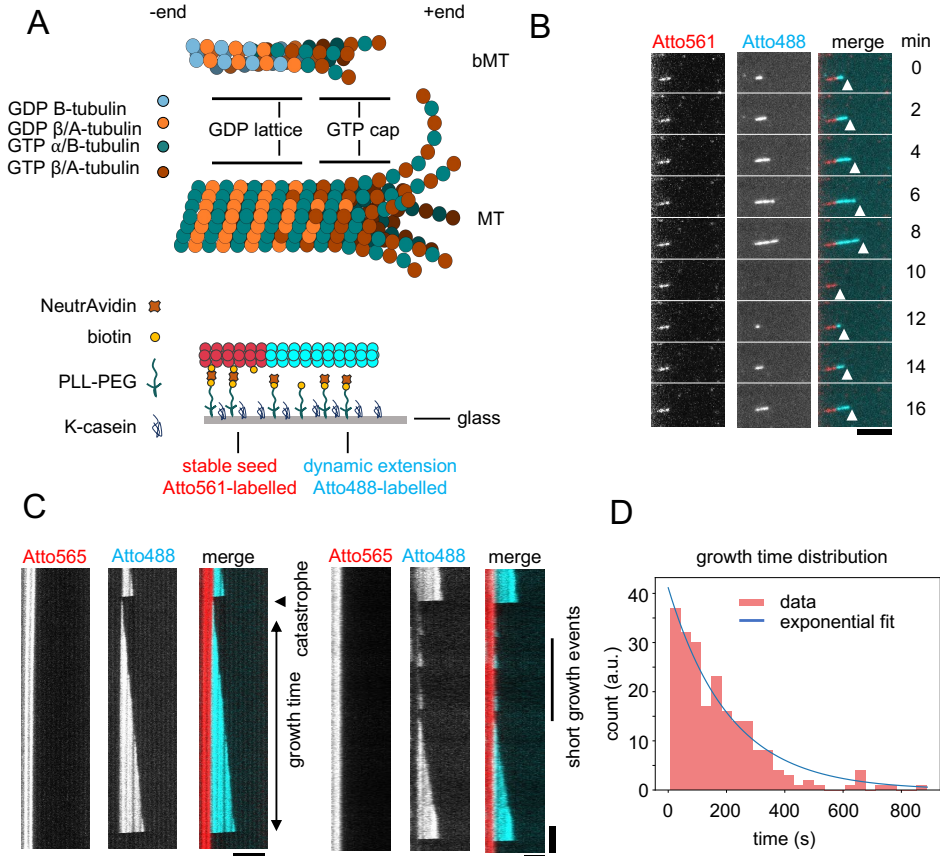


Figure 3.1: Dynamic properties of free bacterial microtubules: (A) (top) Schematic depiction of bacterial and eukaryotic microtubules. Bacterial microtubules are composed of 4-5 protofilaments and both monomers hydrolyse GTP to GDP. Microtubules consist of 13-14 protofilaments instead and only β -tubulin hydrolyses GTP. Both filaments show dynamic instability and hence can be explained by the GTP cap model. (bottom) A schematic depiction of the experimental setup. The glass surface is functionalized with PLL-PEG-biotin and Neutravidin and passivated with κ -casein. GMPCPP-stabilized biotin-labeled seeds which form in the presence of biotin-tubulin bind to the surface through biotin-Neutravidin interaction. Free GTP-tubulin dimers add to the ends of the seeds to generate dynamic filaments. (B) A time series of a bacterial microtubule (cyan, Atto488-labeled bTubAB) growing from an immobilized GMPCPP seed (red, Atto565-labeled bTubAB). The tip of the dynamic bMT is marked by an arrowhead over time, showing dynamic instability of the filament. (C) Time versus distance graphs (kymographs) of dynamic bMTs (cyan, Atto488-labeled bTubAB) which grow from bMT seeds (red, Atto565-labeled bTubAB). The sudden switch from growth to shrinkage is called a catastrophe. Growth time is defined as the growth duration of a filament before a catastrophe. Moreover, on the right, a kymograph example is shown where short growth events were observed to co-exist with longer events. (D) A histogram of growth times of free bMTs. The distribution fits the best with an exponential distribution with a mean equal to 209 ± 19 s. Scale bars = $5 \mu\text{m}$.

3.2D. The catastrophe statistics of stalling events were then further analyzed to compare with previous studies were done with MTs. As observed for MTs, the situation of net zero growth provided by the contact with the barriers, alters the catastrophe dynamics of the filament. Contact time or stalling time is defined as the time interval during which a filament growth velocity is equal to zero ($v_g = 0$) while it is in contact with the barrier before a catastrophe occurs. The mean contact time of 96 bMTs was 27.9 ± 1.6 s (mean \pm SEM), which is 7.6 times shorter than the average growth time of free bMTs (Table 3.1). During data analysis, we manually excluded all the sliding and buckling filaments and focused on true stalling events. The distribution of contact times for stalled bMTs was no longer exponential but clearly peaked as was observed previously for stalled MTs (Figure 3.2E) [66, 74].

Table 3.1: **Dynamic instability features and simulation parameters for bMTs and MTs:** Dynamic instability parameters: growth speed (mean \pm SEM), growth time, and contact time of bMTs and MTs in $0.88 \mu\text{M}$ bacterial and $15 \mu\text{M}$ eukaryotic tubulin concentrations, respectively. Simulation parameters: hydrolysis rate (K_{hyd}) and diffusion of the tip (D_{tip}) (mean \pm 95% CI) and N_{unstable} . Catastrophe is calculated as the number of observations divided by total growth time and the error is catastrophe frequency divided by the square root of the number of observations. Growth time and contact time for bMTs are reported as mean \pm SEM while it is median \pm SE for eukaryotic MTs. MT data from [74].

	growth speed ($\mu\text{m}\cdot\text{min}^{-1}$)	growth time (s)	contact time (s)	K_{hyd} (s^{-1})	D_{tip} ($\text{nm}^2\cdot\text{s}^{-1}$)	N_{unstable}
bMTs	0.58 ± 0.02	173 ± 10 (n = 218)	27.9 ± 1.6 (n = 96)	0.044 ± 0.006	500 ± 151	5
MTs	1.7 ± 0.7	155 ± 15	30.8 ± 1.3	0.070 ± 0.006	3720 ± 310	15

CATASTROPHE STATISTICS FROM SIMULATIONS BASED ON A ONE-DIMENSIONAL MODEL

In analogy to our recent effort for eukaryotic MTs, we then looked for a way to reconcile the measured catastrophe statistics for stalled and free bMTs within a single model. To this end, we simulated bMT dynamics using a simple one-dimensional MT model that has been successfully used before to reconcile the growth time and contact time distributions of free and stalled MTs [74]. The model assumes the stochastic hydrolysis of GTP by tubulin subunits within the MT lattice and a noisy growth, including negative excursions of the MT end (Figure 3.3A), which together affect the size of the stabilizing GTP-tubulin cap. The simulation utilizes a Monte-Carlo method and normally requires three fitting parameters: the GTP hydrolysis rate K_{hyd} , the effective diffusion coefficient of the tip D_{tip} , and the number of adjacent GDP subunits that triggers a catastrophe N_{unstable} . A catastrophe occurs when the number of adjacent GDP subunits at the tip of a filament surpasses N_{unstable} (Figure 3.3A). Using fixed parameter values for the growth rate $v_g = 0.58 \mu\text{m}\cdot\text{min}^{-1}$ (Table 3.1), subunit length $\delta = 8/4$ nm [31], and the average distance between the ends of the filaments (seeds) and the barriers $L_{\text{barrier}} = 1.45 \mu\text{m}$, we sequentially fixed N_{unstable} at a few different values, and then simulated 500 filaments with a range of both K_{hyd} and D_{tip} . Distributions of simulated growth times of free bMTs and contact times of stalled bMTs was com-

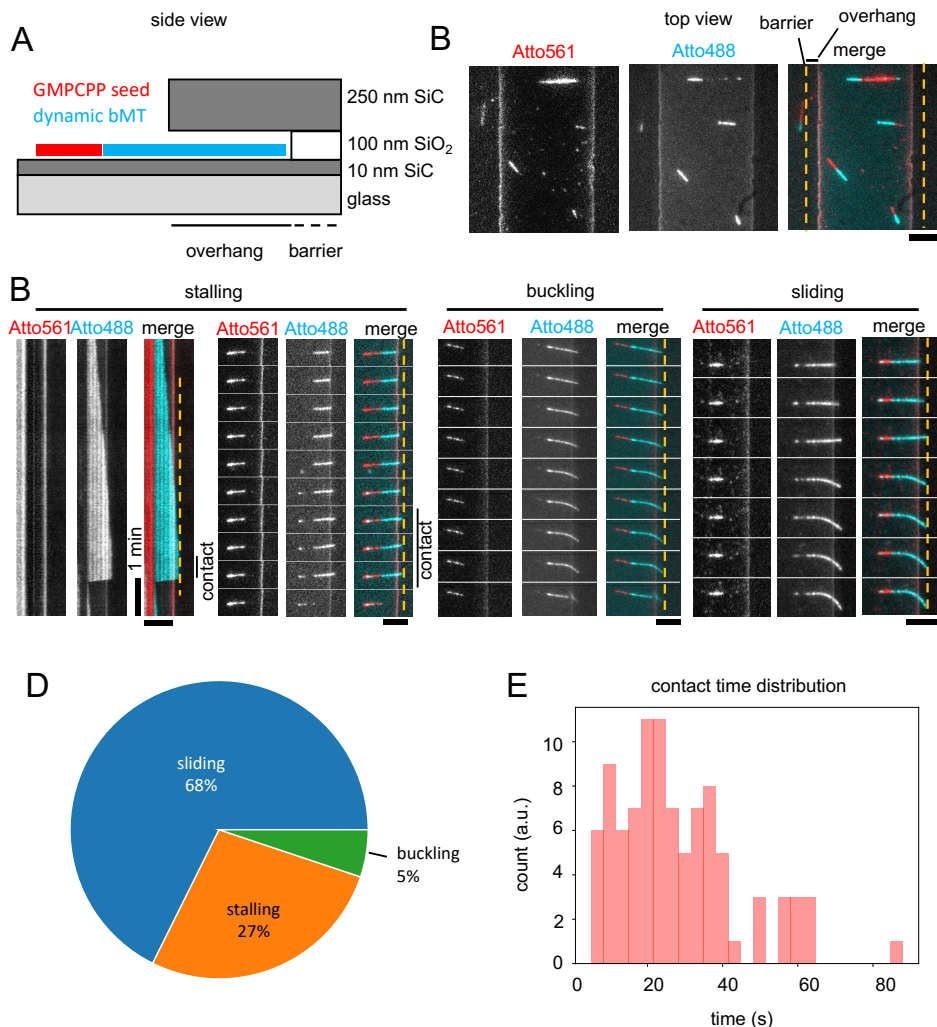


Figure 3.2: Dynamic properties of stalled bacterial microtubules: (A) Schematic illustration of the side view of the experimental setup in the presence of micro-barriers. Barriers were microfabricated on top of a coverslip by coating a thin layer of SiC, a layer of SiO₂ and another layer of SiC. The approximate size of each layer is denoted. In a typical dynamic experiment in the presence of barriers, dynamic bMTs (cyan) grow from immobilized bMT seeds (red) and may interact with a barrier. (B) A TIRFM (top) view of an experimental sample, where bMT seeds polymerized in presence of Atto565-labeled bTubAB are depicted in red, soluble bMT polymerized from Atto488-labeled bTubAB in cyan and barriers with yellow dashed lines. (C) Various events during a bMT-barrier interaction are shown. (left) A kymograph and a time series of a stalling filament (cyan, Atto488-labeled bTubAB) which grows towards a barrier from an immobilized bMT seed (red, Atto565-labeled bTubAB). (middle) A time series of a buckling bMT which undergoes a breakage eventually. (right) A time series of a filament which slides against the barrier and preserves its growth. (D) A pie chart of frequencies of the events described in (C) for a total number of 371 events. (E) A histogram of stalling or contact times of stalled bacterial microtubules. The average contact time of stalling bacterial microtubules was 27.9 ± 1.6 s (mean \pm SEM). Horizontal scale bars = 5 μ m, vertical scale bar = 1 min.

pared to the experimental data using a Kolmogorov-Smirnov-test (Figure 3.3B). The fitting parameters which best capture both free and stalled bMTs were found to be $K_{\text{hyd}} = 0.044 \pm 0.006 \text{ s}^{-1}$, $D_{\text{tip}} = 500 \pm 151 \text{ nm}^2/\text{s}$ (mean \pm 95% CI), and $N_{\text{unstable}} = 5$ (Table 3.1). The predicted diffusion of the tip will remain to be investigated experimentally. The bTubAB hydrolysis rate, on the other hand, was reported $0.02 \pm 5 \times 10^{-4} \text{ mol GTP s}^{-1}$ per mol of bTubAB [33] which is measured for dynamic bMTs in bulk. Figure 3.3C and D depict the empirical cumulative distributions for the simulated (blue) and experimental (red) data sets. As can be seen from the plots, the simulations closely capture the experimental results.

MECHANICAL PROPERTIES OF STALLED BACTERIAL MICROTUBULES

In addition to analyzing the dynamic properties, we used the stalling data to obtain an estimate of the flexural rigidity of bMTs. When growing filament ends arrive at a barrier, they will continue to grow only when the force needed to buckle the filament is smaller than the force needed to halt the growth process (the stall force) [34]. Since the so-called critical buckling force strongly decreases with filament length, we may assume that the longest observed stalling length corresponds to a situation where the stall force and buckling force are just balancing each other.

For the boundary conditions of our experiment, the buckling force is given by the following equation [81]:

$$F_C = 20.19 \frac{\kappa}{L^2} \quad (3.1)$$

where, κ is the flexural rigidity and L is the length of the filament. An estimate of the stall force may independently be obtained using the subunit on- and off-rates during bMT growth. To obtain an estimate of these rates we used the fact that at the critical concentration these rates are balanced. Previously, the critical concentration (C_c) was found to be in the range of 0.4–1 μM in bulk measurements [121]. Taking the lower limit (0.4 μM) to be relevant for growth from seeds, and assuming simple one-dimensional polymer analysis growth [106], we could then use the observed growth rate at 0.88 μM to estimate the values for the association and dissociation rates: $k_{\text{on}} = 10.1 \mu\text{M}^{-1} \text{ s}^{-1}$ and $k_{\text{off}} = 4.02 \text{ s}^{-1}$, assuming that the off-rate is concentration independent. Using $C_c = k_{\text{off}}/k_{\text{on}}$ the stall force can then be calculated [34] from the equation:

$$F_{\text{stall}} = \frac{(k_B T)}{\delta} \ln \frac{k_{\text{on}} C}{k_{\text{off}}} \quad (3.2)$$

where k_B is Boltzman's constant, T is the experimental temperature, $\delta = 2 \text{ nm}$ for bMTs, and C is the subunit concentration. Using the above-mentioned values, we estimate F_{stall} at 1.63 pN for bMTs. Using this value for the force in equation (3.1), combined with the value for the longest stalling bMT filament in our data set: $L = 5.7 \pm 0.2 \mu\text{m}$, we obtained an approximate value for the stiffness of bMTs: $\kappa_{\text{bMT}} = 2.62 \text{ pN}\mu\text{m}^2$. As expected, because of their smaller diameter, this value is smaller than that of MTs, see for example the value that was measured for MTs at 23°C and tubulin concentration 20 μM : $\kappa_{\text{MT}} = 21.2 \pm 1.7 \text{ pN}\mu\text{m}^2$ [65].

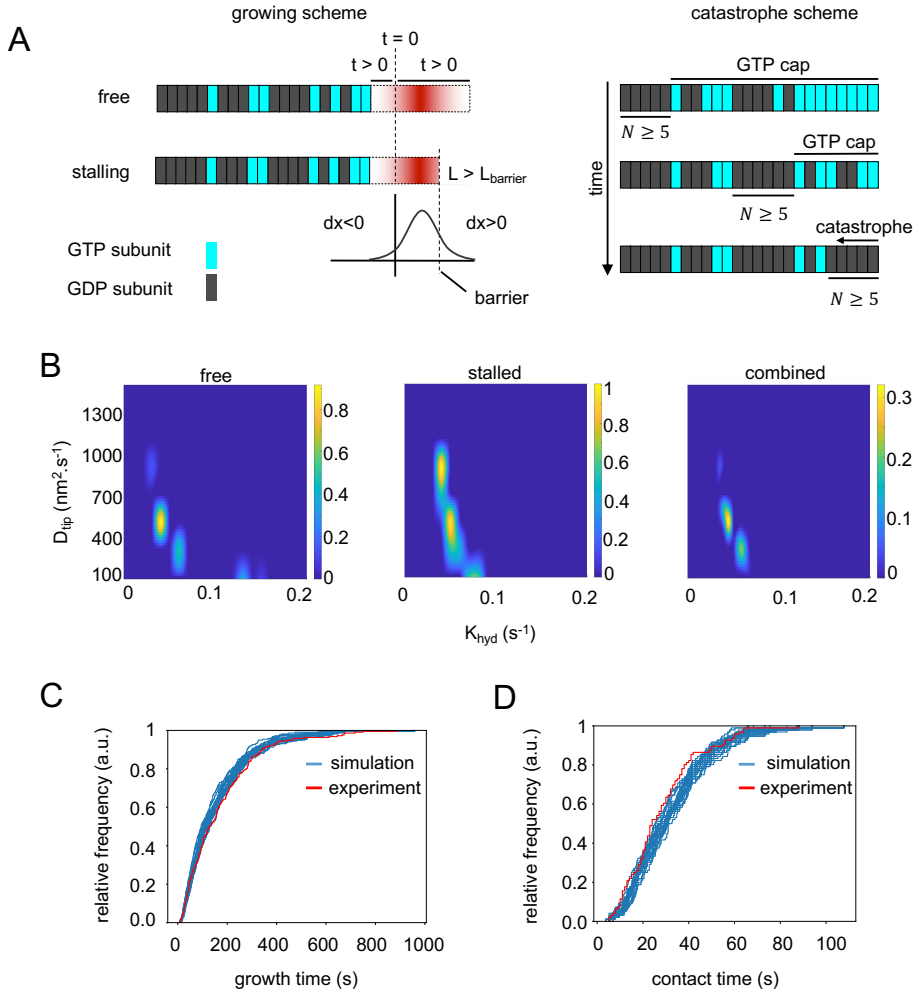


Figure 3.3: Catastrophe statistics from simulations based on a one-dimensional model: (A) A schematic depiction of the basic principles of the one-dimensional model recruited to simulate bMTs. (left) The size and direction of each step in the filament growth at $t > 0$ are determined by a normal probability density function. During each time step, incorporated GTP-bound subunits (cyan) randomly hydrolyze into GDP-bound subunits (gray) with a rate K_{kyd} . Once close to the barrier, the filament length increment is restricted to the distance between the seed and the barrier (L_{barrier}). (right) The cartoon represents the process which leads to a catastrophe. A filament undergoes a catastrophe when the number of adjacent GDP-subunits is equal to or larger than N_{unstable} ($N \geq N_{\text{unstable}}$). (B) A heatmap representation of the equality of the simulations and experimental data for free and stalled bMTs and the product of the two (combined). The graphs plot the p-value of a Kolmogorov-Smirnov test by comparing the empirical distribution of simulations of different hydrolysis rates and diffusion coefficients with the experimental data. (C) The empirical distribution of growth times of free bMTs. The experimental data (red) are compared to simulations (blue). 218 bMTs among 1000 simulated filaments were randomly selected and the cumulative distribution is plotted for 25 different selections. (D) The empirical distribution of contact times of stalled bMTs. The red plot and blue plots represent experiments and simulations, respectively. In this case, 25 samples of 96 bMTs among 1000 simulated stalling bMTs were chosen randomly and plotted.

STRUCTURAL PROPERTIES OF BACTERIAL MICROTUBULE ENDS

Dynamic properties of growing MTs have been related to structural properties of their ends. For example, it has been suggested microtubules in the pre-catastrophe states have extended tapers, or stretches of incompletely cylindrical lattice where lateral interaction sites between tubulin subunits are exposed. One hypothesis is that the absence of lateral contacts with neighboring protofilaments destabilizes these long tapers and leads to catastrophe [29, 58]. Note, however, that growing ends of eukaryotic microtubules were recently shown to be as flared as shortening ones, challenging the popular view that GTP- and GDP-tubulin have different curvatures [92]. To investigate whether the ends of bacterial microtubules resemble eukaryotic microtubules in their bent protofilaments and extended tapers, we turned to electron cryotomography (cryo-ET) and imaged samples containing bacterial microtubules frozen during growth (Figure 3.4A). Due to the fast depolymerization of bMTs, we were unable to make a sample with filaments frozen in a shortening state.

To determine the polarity of bMTs, we performed semi-automated particle picking along each filament, and then subtomogram averaging of these particles using dynamo [19] (see Materials and Methods for details). In the axial projections of averaged particles, we observed a mixture of bMTs containing three, four or five protofilaments (Figure 3.4B). While four- and five-protofilament bMTs appeared to have protofilaments equally spaced around the bMT axis, three-protofilament bMTs looked like four-protofilament bMTs with one protofilament missing, so they were also quantified as four-protofilament ones.

To analyze the unique shapes of bent protofilaments at the ends of bMTs, we denoised the reconstructed tomograms using cryoCARE [16], and then manually segmented the plus-ends to obtain 3D models of the terminal protofilaments [58, 102]. For comparison, we used plus-ends of eukaryotic microtubules frozen during growth or shortening (see Materials and Methods for details). This analysis revealed that the majority of bMT plus-ends had protofilaments terminating without a bent part (69%), unlike plus-ends of growing or shortening eukaryotic microtubules that contained 14% and 1% of protofilaments without a bent part, respectively. Focusing on the protofilaments that did terminate with a bent segment, we found that shortening eukaryotic microtubules carried longer bent segments than the growing ones, as reported previously (32.6 ± 1.6 nm and 24.9 ± 1.2 , respectively; Figure 3.4C and D) [58]. However, bent protofilaments at the plus-ends of bMTs were shorter than observed in both MT samples (16.5 ± 2.4 nm; Figure 3.4D). Although we did not find significant differences between the lengths of the plus-end tapers in growing: 44 ± 10 nm (mean \pm SEM) and shrinking: 32.2 ± 9.4 nm MT samples the average taper length of the plus-end of growing bMTs was found to be shorter than that of MTs (22.9 ± 5.1 nm; mean \pm SEM) (Figure 4.4D). We conclude that bacterial microtubules grow with mostly straight ends, unlike eukaryotic microtubules that grow and shrink with flared plus-ends.

MULTI-FILAMENT BUNDLE FORMATION OF BACTERIAL MICROTUBULES

In addition to individual bMT filaments we often observed bundles of various sizes in both cryo-ET and TIRFM images (Figure 3.5A). TIRFM images suggested that fila-

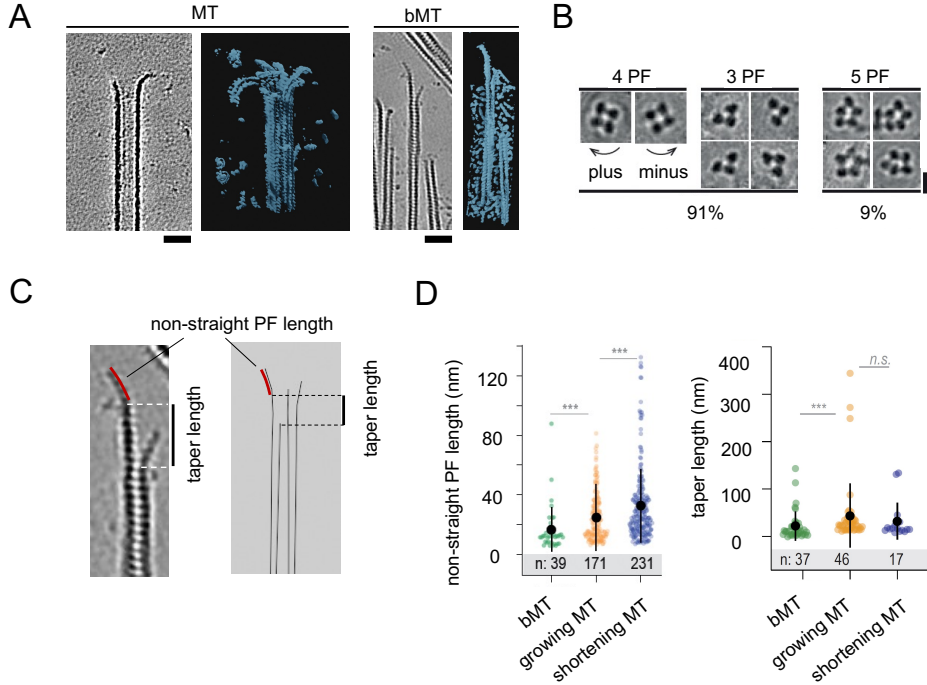


Figure 3.4: **Structural properties of bacterial microtubules ends:** (A) Single slices (grayscale, 0.7 nm thick) and 3D renders (color) of cryoCARE-denoised tomograms with eukaryotic (left) and bacterial (right) microtubules. (B) Axial views of averaged particles used to determine bMT polarity and protofilament number; representative particles for different number of protofilaments and corresponding occurrence of each variant are shown. Due to the asymmetric structure of three-stranded bMTs, we assumed that they were four-stranded which have lost one protofilament and therefore categorized them as four-stranded bMTs. (C) A single tomographic slice (left, 0.7 nm thick) and a schematic (right) of a tapered bMT plus end. Taper length and non-blunt protofilament length are defined. (D) (left) Length of the bent part of terminal protofilaments of growing bMTs (16.5 ± 2.4 nm (mean \pm SEM)) and that of growing and shrinking MTs (24.9 ± 1.2 and 32.6 ± 1.6 nm, respectively (mean \pm SEM)). (right) Plus end taper length of growing bMTs and growing and shrinking MTs. The difference observed between the taper length of eukaryotic and bacterial microtubules was significant.

ments in bundles may be dynamic, as is shown in Figure 3.5A both in the kymograph and the time series. Cryo-ET data analysis revealed that the filaments in bundles often resembled microtubule doublets, structures that were previously reported for axonemal MTs [52]. Bacterial microtubule doublets (bMTDs) were composed of a complete bacterial microtubule of either 4 or 5 protofilaments and an incomplete filament. Different types of doublet structures were observed as represented in Figure 3.5B. We hypothesize that bMTDs form by the growth of an incomplete bMT alongside a preformed complete bMT. According to our observations, bMT bundles may thus represent different forms of bMTDs as well as bundles of multiple complete bMTs. Note that we preferentially picked thinner bundles for the analysis in Figure 3.5B. Much thicker bundles are also present in our samples.

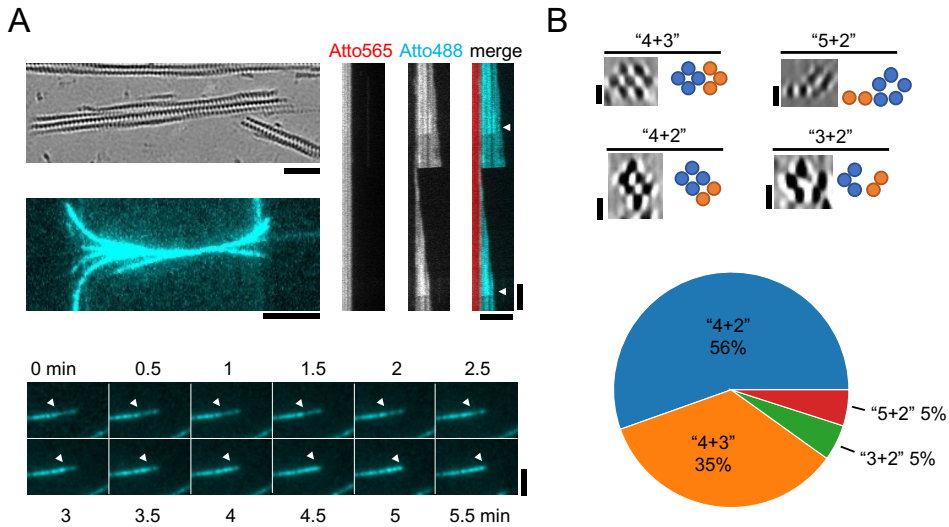


Figure 3.5: **Bacterial microtubules multi-filament bundle formation:** (A) A single 0.7 nm-thick tomographic slice of a bMT bundle (left-top). Scale bar = 50 nm. A TIRFM image of a bMT bundle growing from bundled seeds in the presence of barriers which cause the filaments bending (left-middle; the seeds are not shown). Scale bar = 5 μm . (bottom) A time series of a growing bMT in a bundle. The arrowheads show the growing tip of the filament in the bundle. Scale bar = 5 μm . (right) A kymograph of a dynamic bundle. The shrinking dynamic filaments are marked with arrowheads. Scale bars: horizontal = 5 μm , vertical = 1 min. The time series image is filtered by Kalman Stack Filter plugin <https://imagej.net/plugins/kalman-stack-filter> in ImageJ for better resolution. (B) (top) Axial view of cryoCARE-denoised tomograms showing various conformations of bacterial microtubule doublets and their interpretation. Scale bars = 10 nm. (bottom) A pie chart of the density of bMTD conformations with a sample size of 47 doublets. bMTDs of "5+3" and "4+1" were very rarely observed too.

3.3. DISCUSSION

In this paper, we studied the dynamic properties of force-generating bMTs and compared them with similar experiments performed for eukaryotic MTs, as discussed below. We also used our experiments to obtain approximate values for both the stall force and flexural rigidity of bMTs. The values we obtained, $F_{\text{stall}} = 1.63$ pN and $\chi_{\text{bMT}} = 2.62$ pN μm^2 , are consistent with values obtained for eukaryotic MTs considering that bacterial MTs only consist of 4-5 protofilaments instead of 13. Fewer protofilaments are expected to generate a lower force and thinner filaments are expected to be less stiff. One may therefore consider bMTs to be similar to eukaryotic MTs in terms of their mechanical properties.

To assess the dynamic properties of bMTs, we analyzed the catastrophe statistics for bMTs and asked whether they can be reconciled with catastrophe statistics of eukaryotic MTs within the framework of a simple 1-D model for dynamic instability. Note that in this study we did not vary protein concentration, which is also known to affect dynamic properties, as extensively studied for MTs [47, 113, 132] and to some extent also for bMTs [31]. Instead, we compared catastrophe data for freely growing bMTs for

a specific set of conditions with catastrophe data obtained when growth is completely stalled by a barrier, to be able to make a comparison with the effect that stalling has on the dynamics of eukaryotic MTs. We showed that the barrier-bMT interaction strongly enhances the catastrophe frequency of bMTs, as previously found for eukaryotic MTs. In fact, both the average contact time and the distribution of contact times were found to be very similar for stalled bMTs and stalled MTs in two previous studies [66, 74].

For growing filaments, we expect the average time until catastrophe to be influenced by the growth velocity: faster-growing filaments are expected to have a longer growth time [66]. To make a comparison between MTs and bMTs, we therefore ideally compare with eukaryotic MTs growing at the same velocity. It should be noted however that the relation between growth velocity and average growth time differs between different eukaryotic tubulin purifications. If we compare the growth time we find for growing bMTs to data obtained in one of our older studies [66], the results are comparable (although not identical) for similar growth velocities (Figure S1A), but in our more recent study [74], a similar growth time is found at a much higher growth velocity, indicating that these MTs were less stable than the ones in our older study (Figure S1A). As explained below, we believe that these differences can be reconciled within a simple model, assuming different effective model parameters.

We next employed a one-dimensional model to reconcile the catastrophe statistics of free and stalled bMTs. Similar to our previous findings for MTs [74], we were able to find fitting parameters where the model was able to reconcile both data sets. This suggests that the underlying process that governs the catastrophe statistics of bMTs is similar to that of MTs. To obtain the best possible fits, we had to assume that the number of adjacent GDP-bound subunits at the filament tip necessary for a catastrophe is $N_{\text{unstable}} = 5$, which corresponds to one layer of bTubAB dimers. This is in accordance with what was previously reported for MTs ($N_{\text{unstable}} = 15$, about one layer of tubulin dimers).

The first main fitting parameter, D_{tip} , which represents the diffusive or noisy growth of the filament, was found to be $D_{\text{tip}} = 500 \pm 151 \text{ nm}^2 \text{ s}^{-1}$. Interestingly, this is similar to the diffusion constant obtained from a model fit for MTs growing at a velocity comparable to that of our bMTs in our older study (see Figure 7C in [74] and Figure S1B). However, for the less stable and faster-growing MTs in our recent study, we find a much higher value for this parameter ($D_{\text{tip}} = 3720 \pm 310 \text{ s}^{-1}$) [74], which is consistent with a shorter growth time. For eukaryotic MTs this parameter could be independently verified by measuring tip fluctuations using fluorescently labeled EB1, a protein that follows growing ends of MTs [113]. Interestingly, experimentally obtained values for D_{tip} were of similar order of magnitude and also showed an increase in the growth velocity [47, 74, 113] (Figure S1B). Note that these data were again obtained for different tubulin batches, where corresponding catastrophe times were unfortunately not reported.

Interestingly, while we can reconcile the different growth times of freely growing MTs for our different data sets only by assuming different values for D_{tip} , it appears that the catastrophe statistics of stalled filaments is similar for all data sets (bMTs as well

as MTs for both our previous studies). As can be seen in Figure 3.3B (middle panel), the quality of the fit for stalled filaments is not very sensitive to the value of D_{tip} , but instead largely determined by the second fitting parameter (see also Figure 4A, middle panel in [74]). The second fitting parameter of the model is the hydrolysis rate K_{hyd} . This parameter was found to be of the same order of magnitude for both bMTs and MTs, consistent with similar catastrophe statistics for stalled filaments. The obtained value for bMTs, $K_{\text{hyd}} = 0.044 \pm 0.006 \text{ s}^{-1}$, is higher than the bulk hydrolysis rate previously measured by Diaz-Celis et al.: $K_{\text{hyd}} \approx 0.02 \text{ GTPs}^{-1} \cdot [\text{bTubAB}]^{-1}$ [33, 121]. This difference may be expected since the polymerization of bacterial tubulin is likely to catalyze the hydrolysis of GTP. The GTP hydrolysis rate for eukaryotic MTs has also been measured and was found to be at least: 0.04 s^{-1} [101].

We find that the growth times of free bMTs are exponentially distributed, which is contradictory to previous findings which suggested a lack of short events in the growth time distribution of free bMTs and hence a gamma-distributed growth time [31]. As can be seen from a sample kymograph of a bMT (Figure 3.1C) there are a considerable number of short (less than three pixels in length) filaments (cyan) growing from stabilized seeds (red). Although the length of these filaments was at the order of the resolution of the microscope (250 nm) their lifetimes were long enough to be measured. Fitting a linear function to the short events of the cumulative distribution of growth times (Figure S2A) reveals an R-square equal to 0.98. Moreover, the lowest Bayesian information criterion (BIC) for fitting a gamma distribution to the observed growth times tend to be 167 (Figure S2B) which is higher than the lowest BIC for the exponential fit: 124 (Figure 3.1D). The gamma fit revealed a gamma shape equal to 1.4 ± 0.1 whereas Gardner et al. [48] reported a gamma shape of about 3 for eukaryotic microtubules. In addition, we calculated the time-dependent catastrophe frequency using equation (1) in [48]. A linear fit to the catastrophe frequency revealed a slope equal to 5×10^{-6} which implies a constant catastrophe frequency over time (Figure S2C). These outcomes differ from Gardner's 2011 findings for MTs which suggested that the catastrophe rate for a MT is age-dependent [48], possibly related to the observation that the tapering length of the tip of a MT increases by its age [29]. Interestingly, the tapering length of bMT filaments appears independent of length and hence age (Figure S2D). Nevertheless, a slight negative correlation with a Spearman's correlation coefficient of -0.14 is noticeable which could be a result of the low number of data points. Also, note that the length range that could be measured for bMT filaments was limited: a high density of filaments and a limited field of view in our experiments make it difficult to track the full length of a filament.

Finally, bacterial microtubules are highly prone to form bundles (Figure 3.5B). We find that complete and incomplete bMTs may coexist in bacterial microtubule bundles. The combination of a complete and one or more incomplete bMTs forms bacterial microtubule doublets. bMTDs were observed and reported previously. However, these bundles were called "protofilament bundles" disregarding the presence of complete microtubules [118, 121]. How these structures are formed and whether each of these sub-structures is dynamic is not known. Schmidt-Cernohorska et al. [119] have recently shown that by discarding the C-terminal residues of $\alpha\beta$ -tubulin, a MT dou-

blet could form. Here we hypothesize that the main reason for bundling and forming BMTDs is the absence of highly acidic C-terminal tails in bTubA and B [87, 119].

3.4. METHODS AND MATERIALS

PROTEIN PURIFICATION

Bacterial tubulins A and B were purified and labeled as described in Chapter 2.

FABRICATION OF MICRO-BARRIERS

Micro-barriers were fabricated by adapting the procedure introduced by Kok et al. [74] and is described in detail in Chapter 2.

RECONSTITUTION OF BACTERIAL MICROTUBULE DYNAMICS

Bacterial microtubule dynamic assays were inspired by [31] and eukaryotic microtubule dynamic assays in [74]. bTubAB were stored in 50 mM HEPES-KOH pH 7 while the rest of the ingredients were dissolved and stored in MRB80 (80 mM PIPES pH 6.8, 4 mM MgCl₂, 1 mM EGTA). When necessary, the protein dilution was done in MRB80 as well.

- **bMT seeds:** With two main considerations in mind, *i.e.*, minimizing the bundling effect and maximizing the ultimate seed length, 3 μM bTubAB (67% unlabeled, 7% Atto-565-labeled, and 26% biotin-labeled bTubAB) in the presence of 10 mM KCl in MRB80 was centrifuged in an airfuge (Beckman) cold rotor at 30 psi for 5 min, the pellet was discarded, and the supernatant was polymerized in the presence of 0.5 mM GMPCPP for 10 min at 37 °C. The salt concentration is proved to be optimum to minimize bundling [33]. Seeds were made specifically for each experiment. 20 μl of polymerized seeds were added to the flow channels treated with PLL-PEG-biotin, Neutravidin, and α-casein as described in Chapter 2.
- **Dynamic filaments:** The so-called channel mix was prepared on ice for each experiment separately. 20 μl of tubulin mixture composed of 0.88 μM bTubAB (including 0.08 μM Atto-488 bTubAB), the oxygen scavenging system (Chapter 2), 0.5 mg mL⁻¹ α-casein, 1 mM GTP, and 0.2% methylcellulose was centrifuged in an airfuge (Beckman) in an ice-cold rotor at 30 psi for 5 min, warmed in hand and gently added to the flow channel containing immobilized GMPCPP-seeds. The channel was sealed with vacuum grease and imaged immediately afterwards.

IMAGING AND DATA ANALYSIS

All the images were acquired using a TIRF microscopy setup which is described in Chapter 2. TIRF imaging utility was equipped with a 150 mW 488 nm and a 100 mW 561 nm laser. Each image acquisition was performed at 1 Hz for 20 min at 20°C with an exposure time of 100 ms. The 100x objective was equipped with a 1.5x magnifier which reduced the pixel size to 107 nm. All the image acquisitions were performed within 90 min of the GTP-tubulin being added to the chamber. The drift assigned to the image stacks during image acquisition was removed by subpixel image registration through

cross-correlation using a custom-written MATLAB code. Corrected images were then used to measure the dynamics of bMTs utilizing Fiji (ImageJ) software. All kymographs were created by KymoResliceWide plugin with a straight line of 9 pixels ($0.95\ \mu\text{m}$) width drawn along the long axis of bMTs.

SIMULATIONS

Bacterial microtubules were simulated in both free-growing and stalling situations following the procedure introduced by Kok et al. [74]. To execute the simulations, we first embedded the fixed parameters: growth speed $v_g = 0.58\ \mu\text{m}/\text{min}$, subunit size $\delta = 2\ \text{nm}$, and an average distance of stalling filaments from the barriers $L_{\text{barrier}} = 1.45\ \mu\text{m}$, to the simulations. More precisely, L_{barrier} for each stalling filament was measured from the nucleating end of the corresponding seed. To measure L_{barrier} , bundled filaments were deliberately discarded from dataset.

Fitting parameters were then identified by comparing the growth time and contact time of simulated bMTs to the experimental data employing a Kolmogorov-Smirnov-test (KS-test) using a MATLAB (R2019) code. The test quantifies the equality of empirical cumulative distribution function of the two samples. The equality is then determined by a number (p-value) between 0 and 1 where a higher p-value represents a better fit. We first fixed the N_{unstable} at a few values (*i.e.*, 5, 8, 10, and 12) and ran the simulations for 500 filaments at fixed ranges of K_{hyd} and D_{tip} . The ranges for K_{hyd} and D_{tip} were inspired by the acknowledged values in literature and cubic interpolation was applied to those values. The fitting parameters which simultaneously satisfy free and stalled bMTs' behaviors refer to the highest value of the product of the p-values of the two situations (Figure 3.4B).

After exploring the best fitting parameters (Table 3.1), these parameters were recruited to simulate 1000 bMTs for each experimental situation *i.e.*, freely growing and stalling. To visualize the similarity between the results of simulations and experiments, we randomly sampled bMTs and plotted the empirical cumulative distribution for each sample (Figure 3.3C and D). Each sample had the same size as the experimental sample size for free and stalled bMTs *i.e.*, 218 and 96, respectively. The open-license simulations code is available on GitHub (<https://github.com/florian-huber/mtdynamics>).

SAMPLE PREPARATION FOR CRYO-ET

Bacterial microtubules were polymerized in 80 mM K-PIPES (pH 6.8, supplemented with 25 mM KCl, 1 mM EGTA, 4 mM MgCl_2 and 2 mM GTP). $20\ \mu\text{M}$ bTubAB were polymerized for 10 min at 23°C and then for about 5 min in presence of 5 nm gold beads. $3.5\ \mu\text{l}$ of this solution was added onto a freshly glow-discharged lacey carbon grid suspended in a chamber of a Leica EM GP2 plunger equilibrated at 98% relative humidity and 26°C , and immediately blotted from the back side for 4s, and plunge-frozen in liquid ethane. The grids were stored in LN2 until further use.

Growing eukaryotic microtubules were prepared by polymerizing $15\ \mu\text{M}$ tubulin in presence of freshly prepared GMPCPP-stabilized microtubule seeds for 15 min in a buffer containing 80 mM K-PIPES pH 6.9, supplemented with 80 mM KCl, 1 mM EGTA,

4mM MgCl₂ and 1 mM GTP. Grids were prepared as described above. Shortening eukaryotic microtubules were prepared by first attaching DIG-labelled, GMPCPP-stabilized microtubule seeds to freshly glow-discharged, holey carbon grids pre-incubated with anti-DIG IgG. After 1 min incubation with the seeds, a grid was suspended in the chamber of a Leica EM GP2 plunger equilibrated at 98% relative humidity and 35°C. Microtubules were polymerized on the grid following the addition of 3 µL of 20 µM tubulin in a buffer containing 80 mM K-PIPES pH 6.9, 1 mM EGTA, 4mM MgCl₂ and 1 mM GTP. After 10 min of growth, the shortening was initiated by diluting the tubulin on the grid using 30 µl of the same buffer with 5 nm gold beads but without tubulin, prewarmed at 37°C. The grids were blotted and plunge-frozen in liquid ethane 45s after the dilution to allow all microtubules to switch to shortening.

3

RECORDING, RECONSTRUCTION AND DENOISING OF TOMOGRAMS

Bacterial microtubules were imaged using a JEM 3200FSC microscope (JEOL) equipped with a Gatan K2 Summit electron detector and an in-column energy filter operated in zero-loss imaging mode with a 30 eV slit width. Images were recorded at 300 kV with a nominal magnification of 10000×, resulting in a pixel size of 3.668 Å at the specimen level. Automated image acquisition was performed using SerialEM 3.8.5. software [89]. Two samples of growing microtubules were imaged in the same way, while one sample was imaged using a Titan Krios microscope equipped with a Gatan K3 electron detector at the Netherlands Center for Electron Nanoscopy (NeCEN, Leiden, Netherlands). Images were recorded at 300 kV with a nominal magnification of 26000×, resulting in a pixel size of 3.28 Å at the specimen level. Automated image acquisition was performed using SerialEM. Shortening eukaryotic microtubules were imaged using a Titan Krios microscope equipped with a Gatan K2 electron detector (NeCEN). Energy filtering was performed at post-processing. Automated image acquisition was performed using Tomography software (Thermo Fisher). Images were recorded at 300 kV with a nominal magnification of 33000x, resulting in a pixel size of 4.24 Å at the specimen level. In all cases, we recorded bidirectional tilt series ranging from 0° to ±60° with tilt increment of 2°; a total dose of 100 e⁻/Å² and the target defocus set to -4 µm.

Tomograms were reconstructed and denoised as described previously [86]. In brief, motion was corrected using MotionCor2 [136], tomographic volumes were reconstructed using IMOD 4.11 [78] with twofold binning. Denoising was performed using cryoCARE [16] on tomographic volumes reconstructed using identical parameters from odd and even frames using python scripts (available at <https://github.com/NemoAndrea/cryoCARE-hpc04>).

ANALYSIS OF TOMOGRAMS

To determine the polarity of bacterial microtubules, subvolumes containing filaments of sufficient length were manually extracted from non-denoised tomographic volumes using 3dmod, and averaged using dynamo [19]. To create 3D averages, particles were cropped every 4 nm using a “Filament With Torsion” model, and subsequently averaged. Cross-sections of bMTs presented in Fig 5C show sum projections of particles averaged from a single filament. Based on this analysis, we were able to successfully

determine the polarity of 70 out of 89 filaments; filaments with unclear polarity were discarded from further analysis. The polarity of eukaryotic microtubules was determined by analysing their moiré patterns [27].

To determine protofilament lengths, denoised subvolumes containing plus-ends were manually segmented as described [58, 102]. Coordinates of tubulin subunits in a protofilament were manually placed on a 3D model in 3dmod by inspecting a subvolume opened in slicer and isosurface windows of 3dmod side by side, to monitor the accuracy of manual segmentation on a 3D rendered volume. Protofilament lengths were then extracted from manually segmented models using *howflared* and analysed using MATLAB scripts (<https://github.com/ngudimchuk/Process-PFs>). Taper length was determined as the distance between the first bent segments of the protofilaments bending closest to and farthest from the end of a filament.

AUTHOR CONTRIBUTION

R.A.H fabricated micro-fabricated barriers, performed experiments and analyzed the data, and ran the simulations. V.A.V. performed and analyzed cryo-ET experiments. All authors wrote the paper. M.D. coordinated the project.

ACKNOWLEDGMENTS

We thank Nemo Andrea for rendered figures, Anne Doerr for protein purification and labeling, Maurits Kok for providing some of the Matlab scripts, and Florian Huber for his assistance during working on simulations. We would like to thank Wiel Evers (TUDelft), and Christopher Diebold and Wen Yang (NeCEN) for their excellent technical assistance in data acquisition for cryo-ET. The cryo-ET data on bacterial microtubules were collected at the Netherlands Centre for Electron Nanoscopy (NeCEN) made possible through financial support from the Dutch Roadmap Grant NEMI (NWO.GWI.184.034.014). We also acknowledge Tomohiro Shima and Hanjin Liu for the discussions on cryo-ET experiments. This work was supported by The Netherlands Organization of Scientific Research (NWO/OCW) Gravitation program Building a Synthetic Cell (BaSyC) (024.003.019). V.A.V. acknowledges support from the QMUL Startup grant SBC2VOL8. VAV acknowledges support from the QMUL Startup grant SBC2VOL8.

SUPPLEMENTARY FIGURES

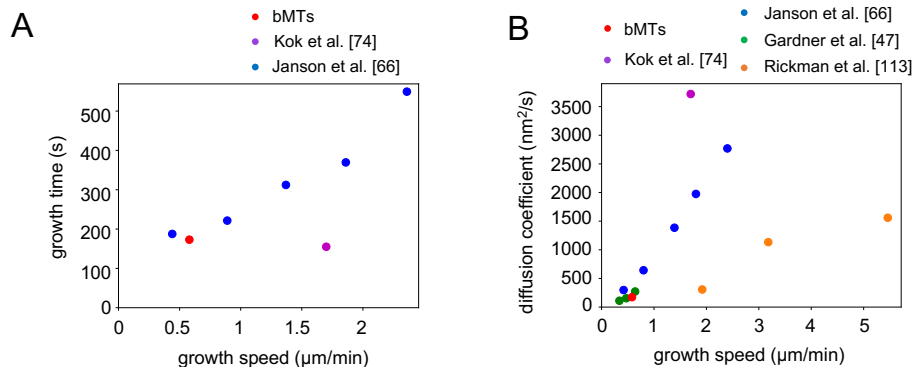


Figure S1: **(A)** Growth time versus growth speed of bMTs and MTs from various studies. The graph indicates that the average growth time of bMTs (red) is comparable to that of MTs for similar growth speeds in our older study [66] (blue). However, the growth time of MTs in our more recent study [74] (magenta) shows a much lower growth time at a higher growth speed. **(B)** Diffusion coefficient versus growth speed of bMTs and MTs from different studies. Diffusion coefficient for bMTs revealed from simulations in this study (red) is comparable to both measured [47] (green) and simulated diffusion coefficient using the measured growth times for MTs [66] (blue) of MTs at similar growth speed. Other data: MT diffusion coefficient revealed from simulations from [74] (magenta), and MT diffusion coefficient revealed from experimental measurements from [113] (orange).

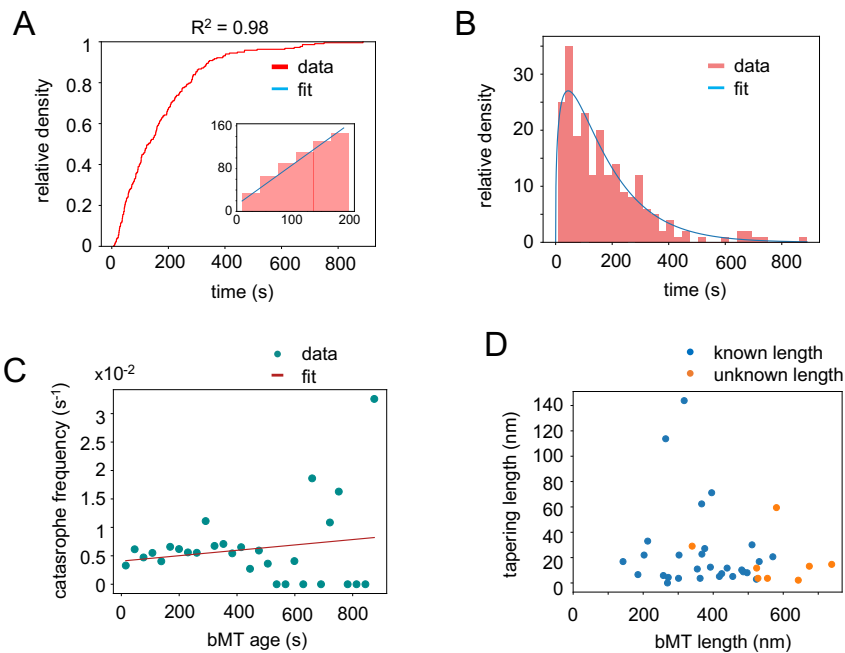


Figure S2: **Bacterial microtubule lifetime is age independent:** (A) A cumulative distribution of growth times of free bMTs. (inset) A zoom-in graph of the cumulative distribution at short times. The linear regression revealed an R-squared equal to 0.98. (B) A gamma distribution function is fitted to the observed growth times of free bMTs. The shape parameter of the gamma distribution was 1.4 ± 0.1 . (C) Time-dependent catastrophe frequency of free bMTs is plotted versus the age of filaments. A linear fit revealed a slope equal to 5×10^{-6} which shows a negligible correlation. (D) Tapering length of bMTs versus the filament's length. The sample included $20 \mu\text{M}$ GTP-bTubAB and was imaged by the cyro-ET technique. Blue circles refer to the filaments of full length and orange circles represent the bMTs which were longer than the field of view and the length refers to the length of the visible segment. The average tapering length was 34.4 ± 7.0 nm. A slight negative correlation (Spearman correlation coefficient = -0.14) is noticeable.

4

DESIGNING A MINIMAL DNA SEGREGATION SYSTEM FOR SYNTHETIC CELLS

Reza AMINI HOUNEJANI, Yash JAWALE, Eli O. VAN DER SLUIS, Beatriz OROZCO MONROY, and Marileen DOGTEROM

What I cannot create, I do not understand

Richard Feynman

Living cells have evolved various mechanisms to faithfully transfer their genomic material to the next generations. Chromosomal DNA segregation is often based on active segregation employing cytoskeletal filaments such as microtubules. In this Chapter, we are interested in designing a minimal system for active DNA segregation for the application in synthetic cells. Given that the eukaryotic mitotic spindle is highly complicated, we instead investigated the use of bacterial segregation systems. The possible employment of two bacterial cytoskeletal systems is investigated, bacterial microtubules (bMTs) and TubZ filaments, both systems are based on the tubulin-like proteins. For each system, we assessed several key requirements: the feasibility of in vitro reconstitution of dynamic filaments with the ability to bind DNA, the potential for encapsulation in liposomes, and the possibility of successful protein expression in PURE system. Based on our findings, we propose the use of a hybrid system based on a combination of the two systems in which an optogenetic tool may be employed for external control.

4.1. INTRODUCTION

Building a synthetic cell is a major area of interest in the field of synthetic biology. An enclosed cell-free gene expression system which can autonomously grow and divide, is called a synthetic cell. Multiple functional modules will be required to eventually build an autonomous synthetic cell, including machinery that is responsible for segregating the duplicated genetic material to the new daughter cells. The aim of this Chapter is to design an opto-controllable active DNA segregation system inspired by bacterial segregation systems. A cartoon of a fully functional version of our segregation system is depicted in Figure 4.1: after expression of the proteins utilizing the PURE system inside a liposome, filament formation leads to liposome elongation. Sample illumination, in turn, triggers expressed adapter proteins, which are composed of optogenetic proteins, and adhesion which leads to DNA-filament binding. Depolymerizing filaments then pull the attached DNA plasmids towards the cell poles and release them subsequently when the light is removed.

4

The two cytoskeletal systems we explored are bacterial microtubules (bMTs) and TubZ filaments. For our eventual design, we will require that the protein components can be expressed in the PURE system. To achieve successful expression of proteins in a cell-free gene expression system, the expression buffer should accomplish at least two main processes, *i.e.*, transcription and translation. The commercially available purified cell extract under the name PURE accommodates energy regeneration and tRNA aminoacylation components and performs transcription and translation for cell-free gene expression. Several studies have recently shown that functional protein expression is achievable with the PURE buffer [51, 69].

BACTERIAL MICROTUBULES

Bacterial microtubules (bMTs) are the closest prokaryotic counterparts to eukaryotic microtubules (MTs) [31, 33, 69]. Although the role of bMTs is still unidentified, based on their microtubule-like properties we decided to investigate the feasibility of designing a segregation system based on bMTs. Dynamic features, such as treadmilling and dynamic instability as well as chaperon-independent expression of bacterial tubulins A and B (bTubA and bTubB), make bMTs attractive cytomotive filaments for synthetic cell uses. In contrast, eukaryotic $\alpha\beta$ -tubulin proteins are incompatible with cell-free expression assays due to their chaperon-dependent folding and necessary post-translational modifications. In addition, previous studies have shown that bTubA and bTubB are expressible in the PURE-based cell-free gene expression system [69].

Performing a DNA segregation with this system, however, remains a standing challenge. The main reason why bMTs can currently not be used for a DNA segregation system is that there is no DNA-binding bMT-associated protein discovered. The specific objective of our study was therefore to either discover or design a potential DNA-binding adapter protein to perform segregation with bMT filaments. First, we used co-sedimentation assays to explore the *Rhodothecobacter debontii* cell lysate for adapter proteins. As these assays were unsuccessful, we then focused on a possible design employing the only known bacterial microtubule-associated protein bacterial tubulin C (bTubC). bTubC has been shown to bind to the bMT lattice and alter the dynamics of

the filaments. Although no significant dynamic alteration was observed in our experiments, we observed that the fluorescently labeled bTubC binds to the lattice of bMTs and might be able to follow shrinking bMTs. These results provide the basis for the possible use of this protein in a hybrid system.

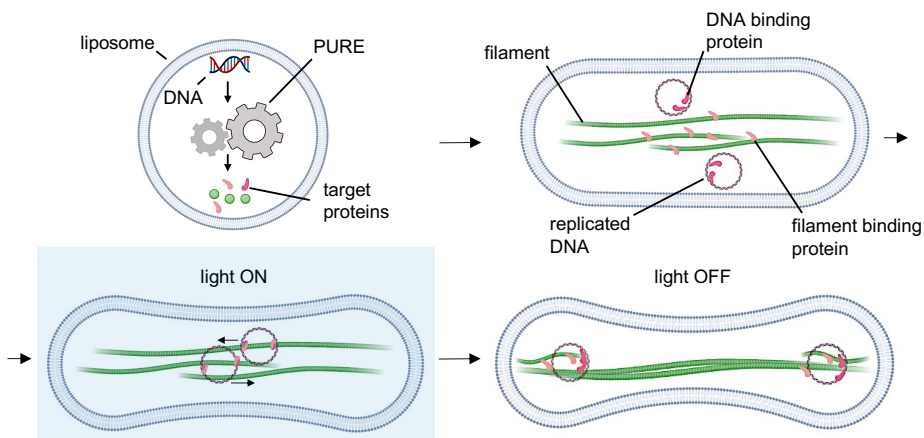


Figure 4.1: **DNA segregation in a synthetic cell with external control:** Schematic depiction of a DNA segregation system in a synthetic cell with light-inducible external control. In a liposome, the proteins expressed with PURE system polymerize, elongating the liposome in the presence of GTP. Expressed adapter proteins bind the filaments and replicated DNA. The illumination of the sample with blue light triggers the association of the two adapter proteins and hence the binding of the DNA to the filaments. Shrinking filaments pull the bound DNA towards the cell poles and the DNA is released after the illumination is turned off. Created with BioRender.com

TUBZ FILAMENTS

As mentioned in Chapter 1, tubulin-like proteins build the family of type-III segregation systems in bacteria. Among all the known tubulin-like proteins, previous works have hypothesized that TubZ from *B. thuringiensis* or *C. botulinum* phage c-st plays the transporter role in the DNA segregation system in the original or host cell [9, 82, 98, 104]. TubZ expression is chaperon-independent and has been purified together with TubR (the DNA binding adapter protein of TubZ). Furthermore, transportation of TubRC segrosome has been reconstituted *in vitro* [43], although the formation and DNA segregation by this system inside the original bacterial cells has not been observed yet. It has been shown that the TubR adapter protein forms a nucleoprotein complex known as the segrosome by binding to the tubC DNA sequence [7, 104]. The binding of TubR twists tubC in a way that the complex forms either a single or double twist loop [88]. *In vitro* observations have revealed that a TubRC complex binds to a TubZ filament and follows the shrinking minus end of the filament [43]. *In vivo*, on the other hand, it has been hypothesized that the TubRC complex may be pulled by treadmilling filaments to the cell poles, where the interaction with the cell membrane may cause DNA release [98]. In this Chapter, the application of TubZRC as a DNA segregation system in synthetic cells is explored. We observed that despite successful TubZ

expression in PURE, these expressed proteins were unable to polymerize into TubZ filaments in the presence of GTP; however, the successful binding of TubR to tubC DNA provides the second ingredient for the possible design of a hybrid system.

OPTO-CONTROL OF A HYBRID SYSTEM

In addition to studying the possible protein components of artificial segregation systems, we focused on finding a way to control these systems externally. Optogenetics can provide accurate and specific external spatiotemporal control over biological processes. Optogenetic tools have been recently utilized in various *in vivo* [100] and *in vitro* [124] applications as well as more specifically in the field of synthetic cells, for instance in cell-cell signaling [2, 25]. Both temporal and spatial controls are critical features that should be considered in designing and building a synthetic cell. Here, we propose a method to achieve control over the segregation system of a synthetic cell using light. We employed an improved light-inducible dimerization (iLID) system composed of a light-oxygen-voltage 2 (LOV2) domain and a bacterial SsrA peptide with the SsrA binding partner SspB [59]. The iLID complex is sensitive to blue light (450-490 nm) in a reversible manner [71]. Upon blue light illumination, an α -helix which is responsible for light-sensitivity undergoes a specific conformational change, thereby releasing the interaction of the LOV2 domain with SsrA, thus allowing the iLID-SspB complex to form (Figure 4.2). In order to control a potential hybrid DNA segregation system, iLID was fused to the bTubC from bTubABC and the SspB protein was fused to the TubR from the TubZRC DNA segregation systems. As neither the bTubABC nor the TubZRC system possessed all desired properties (see above), this hybrid system was designed to take advantage of favorable properties of the two separate systems. We show that the bTubC-iLID binds to bMTs and SspB-TubR forms the nucleoprotein complex with tubC. Our findings represent first steps towards the design of an externally controllable artificial DNA segregation system. However, this thesis does not yet provide a fully functional DNA segregation system that could be directly used in a synthetic cell.

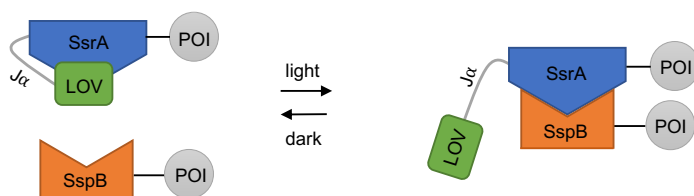


Figure 4.2: **Light-inducible iLID-SspB system:** Schematic depiction of the iLID-SspB optogenetic tool which is used in this Chapter. The schematic depicts the state of the proteins in the dark (left) and in the presence of blue light (right). In the dark state, the interaction between the SsrA and LOV2 domains inhibits the SsrA-SspB interaction, while upon illumination with blue light, the conformational changes in the $J\alpha$ allows the SsrA-SspB interaction.

4.2. RESULTS

Below we present, for each of the two cytoskeletal systems: i) the *in vitro* reconstitution of dynamic filaments, together with candidate adapter proteins for DNA binding, ii) the results of protein expression and filament formation in the PURE system, and iii) our efforts to encapsulate the filament systems in liposomes.

Bacterial microtubule reconstitution in the presence of bTubC:

To evaluate the bMT-bTubC interaction, bTubAB and eGFP-bTubC were purified and labeled as described in Chapter 2. Two different approaches were adopted to investigate this interaction. Firstly, in a co-sedimentation assay, 85 μM unlabeled bTubAB and 2.6 μM eGFP-bTubC were incubated in the presence of 2.8 mM GTP for 10 min at 37°C and centrifuged in a Beckman airfuge (see Methods Materials and Methods section). We observed bTubC in the final supernatant of the last rotation, confirming the co-sedimentation with bMTs as was shown before [3]. In addition, a considerable fraction of the bTubC was seen in the final pellet (cold pellet), a demonstration of the high aggregation affinity of the protein (Figure S1A). Secondly, we performed dynamic bMT assays in the presence of bTubC to assess the interaction between bMTs and bTubC (Figure 4.3A). 1.1 μM (1:10 labeled to unlabeled ratio) bTubAB was mixed with 2 μM eGFP-bTubC and added to immobilized seeds in a flow chamber in the presence of 1 mM GTP and imaged immediately. bMTs were dynamic in this situation (see also Chapter 3) and the images revealed a clear co-localization of the filaments with eGFP-bTubC indicating a significant bMT-bTubC interaction. We observed that bTubC binds to both dynamic filaments (with a lattice binding preference) and GMPCPP stabilized seeds (Figure 4.3B).

An ideal adapter protein for a segregation system based on bMTs, would be able to follow either shrinking or growing bMTs. Our experiments revealed no clear bTubC end-tracking at polymerizing nor depolymerizing bMT ends. Explorations with polystyrene beads coated with eGFP-bTubC showed binding to the filaments and in one anecdotal case a depolymerizing bMT appeared to briefly pull on the bead (Figure S1B). Further experiments using for example optical tweezers would be needed to further verify this type of end-tracking behavior. In addition to filament-binding affinity, an adapter protein (or protein construct) should have DNA binding activity. Although a-priori is not very likely, we first checked whether bTubC has any DNA-binding affinity. bTubC accommodates a TPR domain of 11 helices which bind dominantly to the bTubB [31]. Combining a literature-search with the HHpred tool of the MPI Bioinformatics Toolkit, no DNA-binding domain was found for the bTubC protein. Although a handful of DNA-binding proteins that share high sequence identity with bTubC were identified, their DNA-binding domain was mainly located elsewhere and the TPR domain was not involved in DNA-binding.

Next, we decided to look for other possible bMT-associated proteins in the bacterial cells from which our bTubC originated, *Prostheco bacter debontii*. Co-sedimentation assays followed by mass spectrometry were used to investigate the interaction of bMTs with any protein from *P. debontii* lysates. *P. debontii* cell culture was purchased from DSMZ. A 400 mL cell culture was grown in 628 MMB medium (www.bacmedia.dsmz.de)

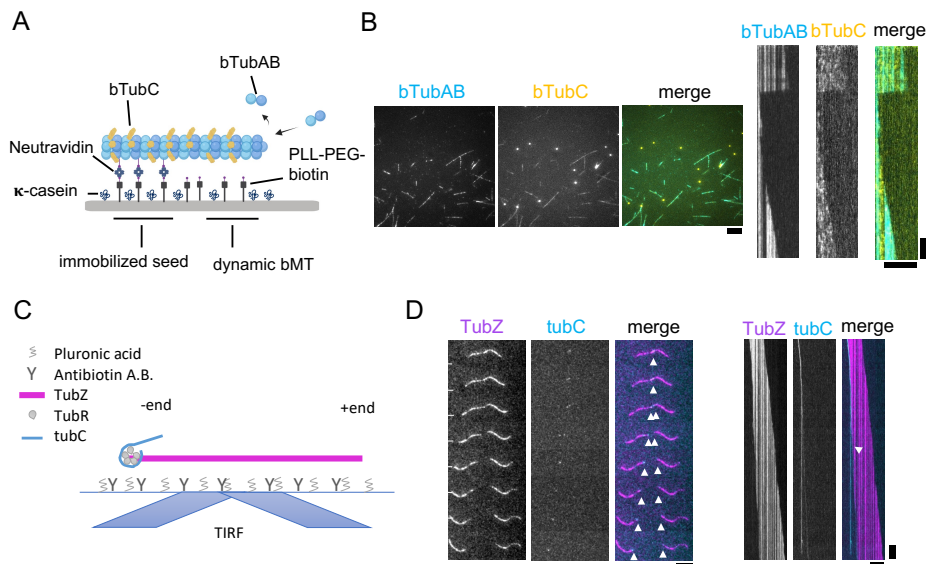


Figure 4.3: Dynamics assays: (A) Schematic depiction of the experimental setup for bacterial microtubule (blue) dynamic assays in the presence of bTubC (yellow). The glass surface of coverslips was treated sequentially with PLL-PEG-biotin, Neutravidin, and κ -casein. Biotinylated bMT seeds were immobilized due to the interaction with the surface-coated Neutravidin and the dynamic bMTs could grow from the immobilized seeds. Created with BioRender.com (B) TIRF images (left) and kymographs (right) of $1.1 \mu\text{M}$ bTubAB which formed dynamic filaments in the presence of $2 \mu\text{M}$ eGFP-bTubC and GTP showing co-localization of bTubC (yellow) and the dynamic bMTs (cyan). The kymographs show that bMTs were dynamic in the presence of bTubC which covers the filament lattice. Yellow spots show that the purified eGFP-bTubC was highly prone to aggregation. (C) Schematic depiction of the dynamic TubZRC system experimental setup. A TubZ filament (magenta) pulls a TubRC (cyan) complex while treadmilling on a surface-coated by anti-biotin antibody and Pluronic acid. (D) TubZRC dynamic assays where filaments (magenta) were formed from $1 \mu\text{M}$ purified TubZ in the presence of 100 nM TubR and 100 pM tubC and carried TubRC segrosomes (cyan) while treadmilling. (left) The time series of two treadmilling TubZ filaments which pull a TubRC complex while treadmilling and sliding over each other. Arrowheads mark the position of the minus end of the treadmilling filaments. (right) A kymograph of a treadmilling TubZ filament where the DNA loses the interaction with the filament. The moment when the centromeric DNA loses its connection with the filament is marked with an arrowhead. The stacks were smoothed by applying Kalman filter. scale bars: horizontal = $10 \mu\text{m}$, vertical = 1 min .

at 30°C for more than 7 days ($\text{OD} = 0.11$), harvested and lysed using a French press apparatus in 50 mM HEPES-KOH pH-7 supplemented with 0.1 mM PMSE. We concentrated the lysate ten times. Then $60 \mu\text{l}$ of $150 \mu\text{M}$ bTubAB was added to $40 \mu\text{l}$ of the concentrated lysate in the presence of 2 mM GTP and incubated for 10 min at 37°C . Another $2 \mu\text{l}$ of 100 mM GTP was added afterwards and centrifuged immediately with a Beckman airfuge (see Materials and Methods section). Mass spectrometry of the SDS-PAGE gel bands (marked with arrowheads in Figure S1C) revealed two major uncharacterized proteins: a protein with 24.6% identity with Kinesin39 from *Micractinium conductrix*, and an ATPase DNA helicase RecQ-like (bRecQL) protein. Surprisingly, no bTubC was found in the mass spectrometry results.

Because DNA binding is a major requirement for the adapter protein in our assays, we focused on the bRecQL DNA-helicase. To verify the protein's binding to bMTs, again two different approaches were adopted. First, 19 μM bTubAB was used to co-sediment with 1 μM purified bRecQL protein in the presence of 1 mM GTP and 2 mM ATP. All assays were performed in a HEPES buffer since the high PIPES concentration in MRB80 could abolish the interaction between the filament and adapter proteins [20]. Unfortunately, we observed no significant binding of bRecQL to the filamentous bTubAB on SDS-PAGE (Figure S1D). Additionally, the sharp bRecQL band in the cold pellet lane in Figure S1D suggests bRecQL is prone to aggregation. The interaction was furthermore tested with YFP-bRecQL in TIRF assays. Similar to the co-sedimentation assays, the interaction between the protein and the filaments was weak and only bRecQL aggregates were observed to weakly bind to bMTs (data not shown).

TubZRC system reconstitution:

To consider an alternative to the bTubABC system, we investigated the TubZRC system (*B. thuringiensis*). First, we reconstituted filament dynamics and DNA binding in a flow chamber made with silanized coverslips that were passivated with anti-biotin antibodies and 1% Pluronic acid F-127 (Figure 4.3C). We mixed 1 μM TubZ (80% AF(Alexa Fluor)488-labelled and 20% unlabeled) with 100 nM TubR and 100 nM full-length Atto647-tubC in the presence of 0.5 mM GTP, before adding it to the flow chamber to image with a TIRF microscope (Figure 4.3D). The high percentage of labeled TubZ was necessary due to issues with labeling yield which means the actual final labeling ratio might have been lower than 20%. We observed TubZ treadmilling as well as TubRC complexes following shrinking minus ends of TubZ filaments as was reported before [43] (Figure 4.3D). Furthermore, filaments were seen to slide over each other in a bundle while carrying TubRC complexes (Figure 4.3D; left). Moreover, it was observed that, possibly due to interaction with the surface, minus end-bound DNA can be released during TubZ filament treadmilling (Figure 4.3D; right). Dynamic assays were performed in the absence of TubR as well. Interestingly, we sometimes observed tubC binding to TubZ filaments even without TubR (Figure S2A).

bTubABC system is fully expressible in the PURE system:

The next step in verification of the suitability of a system for our synthetic cell is to identify whether the system is expressible in the PURE system. Expressing in a background of the PURE*frex2.0* system, Kattan et al. [69] already showed that bTubA and bTubB are expressible from the corresponding genes which subsequently self-assemble into bMTs in the presence of GTP (Figure 4.4A). Both treadmilling and dynamic instability was observed for expressed bMTs. bTubC expression and its interaction with bMTs was also reported in the PURE*frex2.0* [69].

Expressed TubZ forms no filaments in PURE:

Here we also evaluated the expression of the TubZRC system with PURE*frex2.0*. To do so, we incubated 5 nM linear tubZ and tubR DNA constructs (both including a T7 promoter and a T7 terminator) in the presence of BODIPY[®]-FL GreenLys tRNA for 3 hours at 37°C. The samples were then loaded on a protein gel (Figure 4.4B). Sharp bands in the Cy2 channel (488 nm laser) channel and the corresponding bands on the coomassie blue-stained image suggest that the proteins were successfully expressed.

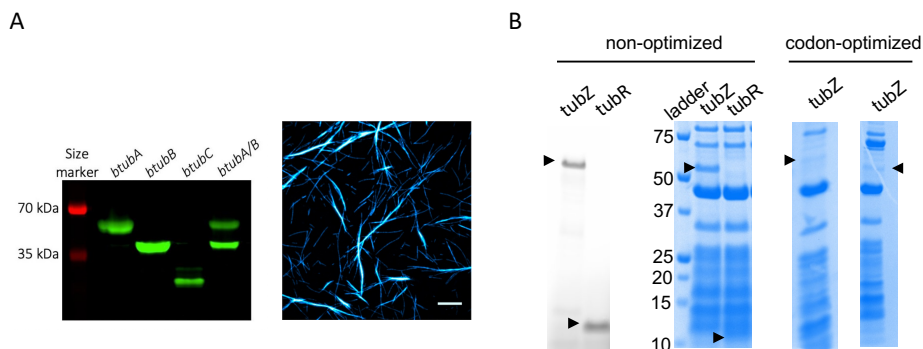


Figure 4.4: cell-free gene expression: (A) (left) Protein gel image of expressed bTubA, bTubB, bTubC and bTubAB proteins in a PURE/*frx*2.0 system supplemented with GreenLys reagent. (right) A TIRF image of the expressed bTubAB in the presence of GTP which forms long and bundled bMTs. Images from [69]. (B) (non-optimized) Protein gel image of TubZ and TubR proteins expressed from 5 nM tubZ and tubR pcr constructs, respectively, in the PURE/*frx*2.0 system in the presence of GreenLys reagent. The image of fluorescently labeled proteins (left) is compared to the image of the same gel after Coomassie blue-staining (right). The arrowheads mark TubZ (top) and TubR (bottom). (codon-optimized) The Coomassie blue-stained protein gel for expression of sequence-optimized tubZ in the absence (left) and presence (right) of 1 μ l of DnaK mix. Expressed TubZ bands are marked with arrowheads.

4

The expressed TubZ was then tested in TubZRC dynamic assays in the presence of a trace amount of labeled purified TubZ (300 nM), 100 nM purified TubR, 100 pM labeled tubC, and 1 mM GTP. Unfortunately, no filament formation was observed in the assays with expressed TubZ. As expressed TubZ might be misfolded, we added DnaK mix, which has been shown to enhance protein folding and activity [51, 69], to the expression solution. However, the addition of DnaK had no significant effect on filament formation by expressed TubZ. We also checked the activity of expressed TubR in the same assays with 500 μ M labeled TubZ. Although no filament forms in the absence of TubR at this TubZ concentration, we observed filament formation which could suggest that the expressed TubR was active and able to enhance TubZ filament formation [104].

Next, we employed the sequence-optimization method described by Godino et al. [51], Kattan et al. [69] and expressed the codon-optimized tubZ gene in gene expression assays as described before. Unfortunately, no filaments were observed in dynamic assays with codon-optimized tubZ either. We loaded the expression products onto a protein gel to visualize their expression yield. Figure 4.4B (right) shows two gels from two separate experiments where 5 nM codon-optimized tubZ linear constructs were expressed in the absence (left) and presence (right) of DnaK. Interestingly, the expression yield was lower in both cases compared to non-sequence-optimized tubZ products.

Expression of btubAB genes leads to the formation of bMT filaments in liposomes:

Another requirement of a synthetic cell is encapsulation. We thus tested whether various properties of our cytoskeletal systems were reproducible inside liposomes. The encapsulation of btubA and B constructs in PURE/*frx*2.0 were shown to successfully

generate bTubAB proteins which in the presence of GTP formed long bMT bundles in liposomes (Figure 4.5A) [69]. Kattan et al. [69] furthermore showed that bMT bundle formation inside liposomes can cause vesicle deformation.

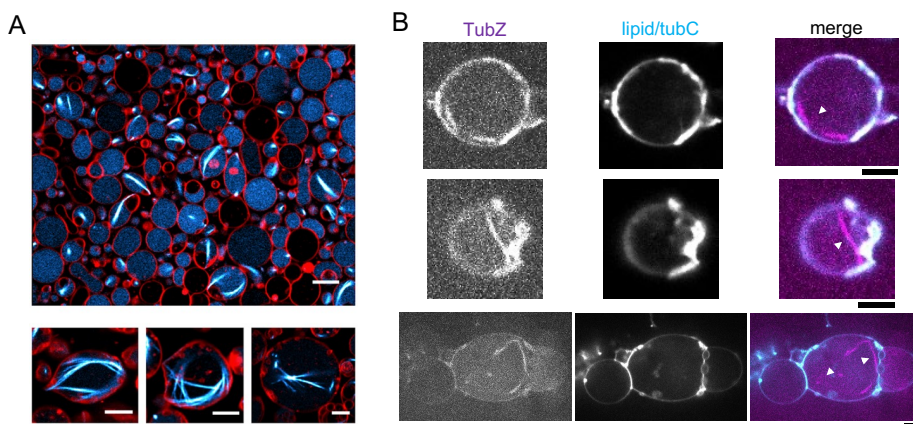


Figure 4.5: **Encapsulation:** (A) A confocal microscopy image of expressed bMTs in GUVs. bMTs (cyan) form multi-filament bundles and reshape the liposomes (red). A closer view of the bundled bMTs and reshaped liposomes is available at the bottom image. scale bars = 10 μm (top) and 5 μm (bottom). Images from [69]. (B) Spinning-disk confocal microscopy images of purified TubZRC encapsulated in liposomes (cyan). A sample containing 6.5 μM purified TubZ in the presence of 100 nM purified TubR and 100 pM tubC was encapsulated in liposomes utilizing a swelling method. The filaments (in magenta) are marked with arrowheads. Lipids and tubC were visible in the same emission wavelength. Scale bars = 5 μm

Purified TubZ proteins form filaments inside liposomes:

To assess the encapsulation of the TubZRC system, we used the swelling liposome preparation method. Lipid molecules were biotin-PEG labeled, so we treated the surface of the flow chamber with BSA:BSA-biotin and then with NeutrAvidin to immobilize the liposomes on the surface. A sample including 6.5 μM TubZ (60% labeled and 40% unlabeled), 100 nM TubR, and 100 pM Atto647-tubC was mixed with 1 mM GTP and encapsulated in Giant Unilamellar Vesicles (GUVs) through a swelling process. The vesicles were then added to the chamber and after 5 min washed with 20 μl BRB80. A spinning-disk confocal microscopy setup was used to image the liposomes. Although the quantitative analysis was impossible due to insufficient data, we were able to confirm encapsulation and formation of the filaments inside the liposomes (Figure 4.5). Inside liposomes, the TubZ filaments were mostly observed in bundled form and, in the absence of crowding agents, diffusing throughout the vesicles. Since both lipids and DNA had fluorescent labels which emit at the same wavelength, it was not possible to spot the DNA co-localization with the TubZ filaments inside the liposomes.

Towards a hybrid system with spatiotemporal control: Given the above-mentioned strengths and weaknesses of the two cytoskeletal systems we next designed a light-inducible hybrid system by fusing proteins of various systems to that of the iLID-SspB system. More specifically, we fused bTubC to iLID via a leucine zipper and TubR to SspB via a GGGGATAGAGG linker (Figure 4.6A). To evaluate the activity of our light-

inducible system, we purified the proteins bTubC-iLID and SspB-TubR and assessed their interaction with bMT filaments, the DNA sequence (tubC), and with each other. First, we tested the bTubC-iLID interaction with polymerized bMTs. In a channel with immobilized seeds, we polymerized 0.9 μM bTubAB (20% labeled and 80% unlabeled) in the presence 83 nM AF568-bTubC-iLID and 1 mM GTP. Significant bMT lattice coverage by the AF568-bTubC-iLID was observed (Figure 4.6B). We observed dynamic bMT filaments in these assays and AF568-bTubC-iLID aggregation was considerably lower than observed for eGFP-bTubC. Next, we verified the complex formation of SspB-TubR with full-length tubC with a gel Electrophoretic Mobility Shift Assay (EMSA). In a test tube, 1 nM Atto647-tubC was mixed with wild-type TubR or various concentration of SspB-TubR according to the assays described by Fink and Lowe [43]. As can be seen in Figure 4.6C, the more we added SspB-TubR proteins, the more DNA was shifted providing evidence for the SspB-TubR interaction with the tubC DNA sequence. Note however, that the interaction was not as efficient as with wild-type TubR.

4

Then we tested bTubC-iLID and SspB complex formation upon photo-activation. The experimental setup is schematically depicted in Figure 4.6D. We assessed the binding of SspB-nano-mOrange to bMT seeds covered with biotin-bTubC-iLID while activated by blue light. The biotin was expected to have no significant effect on the experiments. The main advantage of using seeds is that stable filaments make long image acquisitions feasible. First, we incubated 1 μM bTubAB (including 10% Atto488-bTubAB) in the presence of 0.5 mM GMPCPP at 37°C for 5 min in a test tube. Then 80 nM biotin-bTubC-iLID and 500 nM SspB-nano-mOrange were added to the test tube and the whole mixture was added to the flow chamber. We observed that during blue light illumination, SspB-mOrange accumulated on bMT seeds in a reversible manner (Figure 4.6D). Despite a significant amount of (decreasing) background signal, an increment in fluorescence intensity upon illumination is clearly visible in the intensity graph in Figure 4.6D, which is due to the light emitted from the SspB-nano-mOrange being recruited to bMT seeds over time. Although labeled with Atto-488, bMT seeds were visible while imaging with a 561 nm laser (Figure 4.6D, bottom-left). We later found out that the biotin-bTubC-iLID sample was contaminated with a 561 fluorescent dye. We have also tested the complex formation of bTubC-iLID with SspB-TubR upon blue light illumination, however, due to some technical issues (like SspB-TubR aggregation at high concentrations) we have not yet been able to observe the interaction.

4.3. DISCUSSION

In this Chapter, we investigated two different systems *i.e.*, bacterial microtubules and TubZRC as well as their integration into a hybrid system by using an optogenetic tool composed of the light-inducible iLID-SspB complex to build an externally controllable active DNA segregation system. Previous studies already reported the *in vitro* features of each system [31, 43, 69]. Here we first focused on the ability of each system to recruit DNA as required for our synthetic cell.

In our experiments, we reconstituted the dynamic properties of the two systems: bTubABC and TubZRC. We showed that labeled bTubC proteins bind to the lattice of bacterial microtubules. To assess the transport of any cargo by bMTs, we coated polystyrene

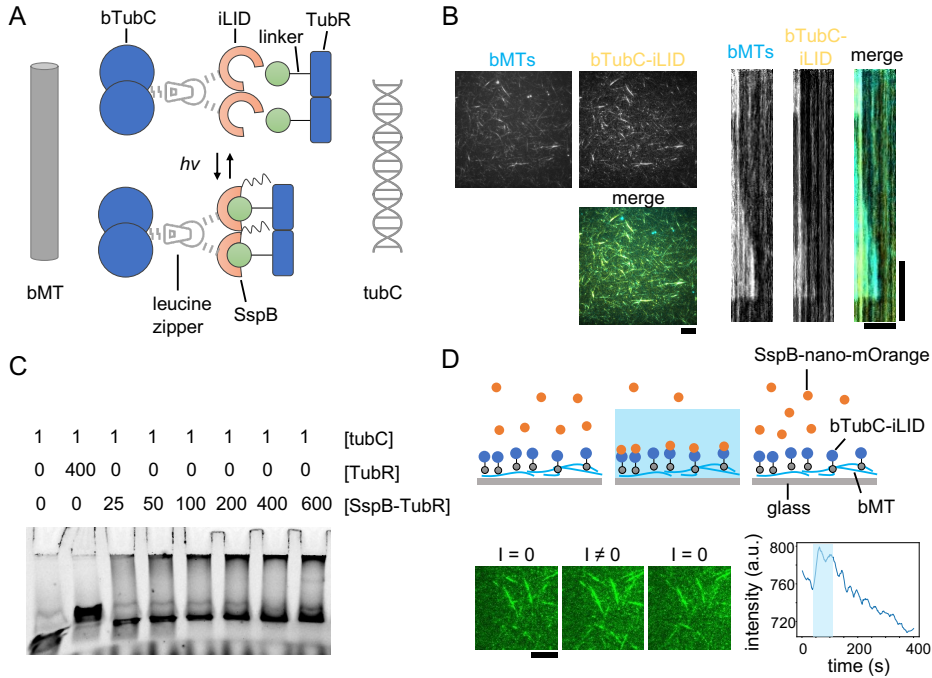


Figure 4.6: Light-induced interaction of bTubC-iLID with SspB-TubR: (A) Schematic depiction of the light-inducible bTubABC-TubRC hybrid system. Two bTubC proteins are fused to two improved Light-Inducible Dimer (iLID) through a leucine zipper, a complex designed to interact with bMTs. On the other hand, TubR is fused through a linker to a SspB protein where the SspB-TubR complex is expected to bind to tubC DNA in a dimerized form. Through a reversible process and upon blue light (488 nm) illumination, bTubC-iLID switches to its active form and binds to SspB-TubR. (B) A TIRF image of a bMT dynamic assay where $0.8 \mu\text{M}$ bTubAB filaments grow from immobilized GMPCPP seeds in the presence of 83 nM AF568-bTubC-iLID (left; scale bar = $10 \mu\text{m}$) and a kymograph of a dynamic bMT in the same experiment. (right; scale bars: horizontal = $5 \mu\text{m}$, vertical = 1 min) (C) An EMSA gel image of 1 nM full-length tubC interaction with 400 nM wild-type TubR and a dilution gradient of SspB-TubR from 25 - 600 nM on a 6% polyacrylamide gel. (D) (top) A schematic depiction of SspB-nano-mOrange recruitment to bMT seeds via bTubC-iLID upon blue light illumination. (bottom) TIRF images of bMT seeds in the presence of 80 nM biotin-bTubC-iLID and 500 nM SspB-nano-mOrange. The seeds were first imaged with a 561 nm laser ($I = 0$), then, at a certain point the 488 nm laser was turned on ($I \neq 0$) which later was reduced to zero ($I = 0$) again. In the presence of blue light ($I \neq 0$), the brightness of the filaments increased due to SspB-nano-mOrange accumulation. bMT seeds are visible in the TIRF images before the SspB-nano-mOrange accumulation due to a 561 nm dye contamination in biotin-bTubC-iLID samples. A Graph of the mOrange signal on bMT seeds over time is shown on the right. The plot is smoothed using Savitzky-Golay filter. The highlighted segment indicates $I \neq 0$. Scale bar = $5 \mu\text{m}$.

beads with purified bTubC and observed that depolymerizing bMTs may carry bTubC-coated beads. Nevertheless, due to a lack of enough data caution must be applied and other techniques *e.g.*, optical tweezers might be needed to confirm the pulling phenomenon. In addition, we conducted a search on the possible DNA binding affinity of bTubC using a MPI (Max Planck Institute) bioinformatics toolkit which revealed no DNA binding for bTubC. We also found that other possible bMT adapter proteins which were discovered exploiting co-sedimentation assays were not reliable, due to

weak interactions with bMTs. Therefore, no suitable candidate proteins were identified to mediate the filament-DNA interaction in a bacterial microtubule-based DNA segregation system.

Next, we considered the TubZRC system which has been hypothesized to be responsible for faithful DNA partitioning in several species [9, 98, 104]. To assess the adequacy of the TubZRC system, we reconstituted the system in flow chambers. We observed that treadmilling filaments are able to carry the minus end binding TubRC complex which has been reported previously [43]. Besides treadmilling, TubZ filaments displayed bundling as well as sliding within a bundle and we observed that TubRC segrosomes might lose the interaction with the filament during treadmilling.

4

Subsequently, the possibilities of cell-free gene expression and liposome encapsulation were investigated for both systems. Kattan et al. [69] showed that bTubA and B are expressible in PURE $_{flex}$ 2.0 and form dynamic filaments in a flow chamber in the presence of GTP. In their study, they successfully encapsulated the expression system inside GUVs which in the presence of the btubA and btubB genes synthesized the proteins of interest and formed bMT bundles which were able to reshape the liposomes. They also showed that the only known bMT-associated protein, bTubC, is expressible in the same manner. On the other hand, although the expression of TubZ proteins in the PURE system did not lead to an active form of the protein in our experiments, we showed that using a swelling method we can encapsulate purified TubZ filaments inside GUVs. While the TubZ filaments formed bundles inside the liposomes, no dynamics was observed which was likely due to the high tubulin concentration. Hence further optimization is required for functional DNA or cargo transport inside liposomes. Moreover, under our conditions the encapsulated filaments were not observed to deform the liposomes in contrast to MTs and bMTs [40, 69].

To overcome the drawbacks of each system, we designed a hybrid system which exploits various parts of the two systems. The design is composed of fundamental components of a minimal DNA partitioning system, namely a cytomotive filament (bacterial microtubule), an adapter protein (bTubC-TubR), and the centromeric DNA sequence (tubC). bMTs from *Prosthecobacter* were chosen since they are expressible in the PURE system inside liposomes. bTubC, which is a bMT binding protein, was fused to an iLID protein complex to enable the recruitment of a DNA binding complex upon blue light activation. We showed that bTubC-iLID, indeed, binds to bMT filaments and tends to recruit SspB-nano-mOrange proteins on the bMTs upon the illumination by blue light (Figure 4.6). For binding to DNA, we used TubR from *B. thuringiensis* and linked TubR to a SspB domain which could bind to bTubC-iLID upon activation with blue light. Using EMSA, we showed that the SspB-TubR complex binds to the tubC DNA sequence when the connection between the two peptides is mediated by a linker. Despite these promising achievements, steps remain to be taken to build a functional controllable DNA segregation system for our synthetic cell. Further work is required to assess the interaction between bTubC-iLID and SspB-TubR in the presence of bMTs and tubC, and establish the expression and liposome encapsulation of the entire system.

Although our hybrid optogenetic system is designed to allow for temporal control over a DNA partitioning system, spatial control is equally important as random segregation may carry the cargo to unwanted locations. We hypothesize that the ability of bMTs to elongate liposomes might break the symmetry of a spherical liposome and bring the replicated plasmids to the ends of the elongated cell during segregation (Figure 4.1). Bundled bMTs contain dynamic filaments which may transport the DNA while the bundle deforms the liposome. Further work is required to establish the viability of our hybrid system, including the expression and liposome encapsulation of the entire system.

4.4. MATERIALS AND METHODS

Proteins used in this Chapter are stored in the buffers indicated in the purification processes in Chapter 2. Other ingredients are stored in MRB80 (80 mM PIPES, 4 mM MgCl₂, 1 mM EGTA, pH 6.8) unless it is stated otherwise.

PROTEIN PURIFICATION

Proteins used in this Chapter, bTubA, bTubB, bTubC, TubZ, TubR, bTubC-iLID, and SspB-TubR, were purified and labeled as described in Chapter 2.

CO-SEDIMENTATION ASSAYS

The co-sedimentation assays were done to test the bMTs interaction with eGFP-bTubC, bRecQL, and proteins in *P. debontii* lysate. Here we explain the protocol for bTubC, however, in the first step the concentrations could be replaced with either 1 μM bRecQL for bRecQL assays or 40 μl cell lysate for lysate co-sedimentation assays.

85 μM unlabeled bTubAB was mixed with 2.6 μM eGFP-bTubC and supplemented with 10 mM MgCl₂, 50 mM KCl, and 3 mM GTP to a finale volume equal to 105 μl and incubated for 10 min at 37°C. The sample was then centrifuged at 30 psi on a Beckman airfuge for 5 min at room temperature. The supernatant was collected for the gel (warm supernatant). The pellet was resuspended in 50 μl of 50 mM HEPES-KOH pH 7.0 and incubated for 30 min on ice with occasional pipetting to depolymerise the filaments. Since during the process, the formation of protein aggregates is not completely avoidable, we centrifuged the solution on a cold rotor once more to discard any aggregates. The supernatant was run on a SDS-PAGE gel (cold supernatant). The pellet was resuspended in 20 μl buffer and run on the gel (cold pellet) (Figure S1).

TIRF DYNAMIC ASSAYS

bTubABC reconstitution assays:

Using parafilm straps, 10 μl flow chambers were made with base piranha (H₂O₂:NH₄OH:H₂O with 1:1:5 ratio) cleaned coverslips. The glass surface of the channels was treated with PLL-PEG-biotin, Neutravidin, and α-casein as described in Chapter 2 for stalling assays. Seeds were made by 10 min 37°C incubation of 13.5 μM (10 μM unlabeled, 1 μM 561-labeled, and 2.5 μM biotin-labeled) bTubAB in the presence of 10 mM KCl and 1 mM GMPCPP. Seeds were then diluted 50 times in warm MRB80 and incubated in the channels for 5 min. A mixture of 1.1 μM (1 μM unlabeled and 0.1 μM

561-labeled) bTubAB and 2 μM eGFP-bTubC in the presence of oxygen scavenging system, 0.2% methyl-cellulose, 0.5 mg mL^{-1} α -casein, 100 mM KCl, and 1 mM GTP was added to the channels, sealed and imaged immediately.

TubZRC reconstitution assays:

TubZRC dynamic assays were inspired by the experiments done by Fink and Lowe [43]. To minimize the bundling effect these experiments were done in BRB80 pH 7.2 (80 mM PIPES, 1 mM MgCl_2 , 1 mM EGTA) background. 10 μl flow chambers were made with silanized coverslips using parafilm straps. Coverslips were silanized with *repel-silane* (2% dichlorodimethylsilane in trichloroethylene or octamethylcyclotrasilane) solution according to the procedure described by Nick Maleki et al. [99]. The channels were made wider than normal to ensure easy flow of viscous fluid. The silanized surface then was treated with 10% anti-biotin antibody (Sigma-Aldrich) for 10 min. Free anti-biotin was removed by two times wash with BRB80 pH 7.2 and 50 μl 1% Pluronic acid F127 was added to the channel and incubated for 15 min. A channel mix of 1 μM (80% AF488-labeled and 20% unlabeled) TubZ, 100 nM TubR and 100 pM 647-tubC supplemented with an oxygen scavenging system, 2 mg mL^{-1} BSA, 0.01% TWEEN20, 0.6% methyl-cellulose and 0.5 mM GTP was made meanwhile on ice. Channels were washed with 50 μl of BRB80 then 20 μl BRB80 containing the oxygen scavenging system. The channel mix was then added to the channels, and channels were sealed with vacuum grease and imaged immediately.

Hybrid system reconstitution assays:

For dynamic assays which were used to test bMT-bTubC-iLID interaction (Figure 4.6B) the channels were made with piranha-cleaned coverslips and treated with 10% anti-biotin antibody (10 min), and 5 mg mL^{-1} BSA (10 min). bMT GMPCPP-seeds were made as described before, diluted 40 times, and added to the channel and incubated for 3 min. A channel mix containing 0.9 μM bTubAB (20% 488-labeled and 80% unlabeled) and 83 nM Alexa-Fluor-568-bTubC-iLID in the presence of the oxygen scavenging system, 3 mg mL^{-1} BSA, 0.2% methyl-cellulose, and 1 mM GTP was added, sealed, and imaged immediately.

To assess the interaction between bTubC-iLID and SspB-TubR from the hybrid system, we first used SspB-nano-mOrange instead of SspB-TubR (Figure 4.6D). In a channel made by silanized coverslips, 5 mg mL^{-1} BSA was incubated for 10 min followed by two times wash with MRB80. A channel mix containing 1 μM bTubAB (10% 488-labeled and 90% unlabeled) supplemented with 3 mg mL^{-1} BSA, 0.1% methyl-cellulose, 50 mM KCl, oxygen scavenging system, and 0.5 μM GMPCPP, was incubated for 5 min at 37°C. 80 nM biotin-bTubC-iLID and 500 nM SspB-nano-mOrange was added to the mix and the sample was added to the channel. The channel was sealed and imaged immediately.

IMAGING

TIRF and confocal imaging were performed using the methods described in Chapter 2. Microscopy setups were equipped with a 150 mW 488 nm, a 100 mW 561 nm, and a 110 mW 642 nm laser. The imaging was acquired at 1 Hz and with 100 ms exposure time.

PREPARATION OF DNA CONSTRUCTS

The DNA sequences were equipped with the T7 promoter, ribosome binding site (RBS), and T7 terminator sequences and synthesized and cloned in the pUC57 plasmid (GenScript, United States). The plasmids pED61 and pED62, and btTubZ_CO_IDT gene which express TubZ, TubR, and (codon-optimized) TubZ proteins, respectively, were amplified in standard polymerase chain reaction (PCR) process and were checked on a 1% agarose gel. PCR constructs were then purified with Wizard SV Gel kit (Promega) and the concentration and purity were determined by NanoDrop 2000, Thermo Fisher. The btTubZ_CO_IDT construct which is a codon optimization of tubZ DNA sequence was designed according to the process explained in [69]. The sequence for each of the DNA constructs can be found at the end of this Chapter.

CELL-FREE GENE EXPRESSION ASSAY

Cell-free expression assays were performed in PURE $_{flex}$ 2.0 (GeneFrontier Corporation, Chiba) according to the protocol described by Kattan et al. [69]. The expression was performed with 5 nM of linear tubZ or tubR construct with and without 1 μ l DnaK chaperon mix (GeneFrontier Corporation). A total volume of 20 μ l was incubated for 3 h at 37°C in pcr tubes. To visualize the expressed proteins on protein gels, 1 μ l GreenLys solution (FluoroTect, Promega) was added to the expression mixture before the incubation. Expressed proteins were also used in TubZRC reconstitution assays as described before. To check the filament formation by expressed TubZ, TubZ in the reconstitution assays was replaced by expressed TubZ and a trace amount (300-500 nM) of AF488-TubZ to visualize the filaments. To maximise the amount of expressed proteins in dynamic assays, we only used essential components *i.e.* 100 nM purified TubR, 100 pM 647-tubC, 1 mM GTP, and 0.1% methyl-cellulose and no crowding agent or oxygen scavenging system.

LIPOSOME ASSAYS

In this Chapter we mainly utilized the swelling method for liposome preparation. In a swelling method, liposomes swell from lipid-coated beads dipped in the sample solution. The swelling method was selected for its high encapsulation efficiency and the fact that no detergents are involved in the whole process. Another advantage of using this method is that it allows liposome production in low solution volume which is favorable for precious samples of PURE. Glass beads were coated with lipid molecules according to the process explained by Kattan et al. [69]. After drying in desiccator beads were stored at -20°C for later use. About 20 mg of beads were added to a test tube. The protein mix was added to the tube and incubated for 2 h on ice in dark. During incubation, the tube was gently rotated while keeping it at 60° angle (3-4 times in total). After 2 h incubation, four complete cycles of freeze-thaw were performed by dipping the tube in LN₂ using plastic tweezers and then thawing at room temperature. The sample should not heat up to room temperature. Meanwhile on base piranha-cleaned coverslips, 10 μ l channels were made with parafilm then treated with BSA:BSA-biotin (1 mgmL⁻¹) for 10 min followed by a washing step with 20 μ l BRB80. Then, 10 μ l 1 mgmL⁻¹ NeutrAvidin was added and incubated for 10 min. After two times wash with BRB80, the liposome mixture was added to the channel which fol-

lowed by another two-time wash after 5 min incubation. The sample was imaged with a spinning-disk confocal setup.

AUTHOR CONTRIBUTION

R.A.H., Y.J., K.v.G., and B.O.M. performed experiments and analyzed the data. E.O.v.d.S. designed, purified and labeled the proteins. R.A.H., E.O.v.d.S. and M.D. wrote the paper. M.D. coordinated the project.

ACKNOWLEDGEMENTS

We thank Elisa Godino for her assistance on cell-free gene expression assays and performing the codon optimization on *tubZ* sequence, Christophe Danelon for the gift of PURE*frex2.0* system, Johannes Kattan for preparation of the swelling lipid-coated beads, and Anne Doerr for protein purification. We thank Kaj Verheij for his exploratory experiments as part of his bachelor end project. This work was supported by The Netherlands Organization of Scientific Research (NWO/OCW) Gravitation program Building a Synthetic Cell (BaSyC) (024.003.019).

4

SUPPLEMENTARY MATERIALS

sequence of *tubZ* construct

```
TAATACGACTCACTATAGGGGAATTGTGAGCGGATAACAATTCCCCTCTAGAAATAAT
TTTGTTTAACTTTAAGAAGGAGATATACATATGGCTAGCATGACTGGTGGACAGCAAA
TGGGTATGTTATTAACAGTAATGAACTAGAACATATCCATTCAACTAACCATAGTGT
AAATGATATTAGTATACGATGGGGAGTTATTGGTGCTGGTCAAAAAGGTAATAAAGAG
GCTGATTTATTCGCAGGTTACAAGTTTTCGAATGGAAGTACTTGCTATCCGACATTAG
CTGTTAACTTTGCAGAGTCAGATATGATGCATTTACAAAATATTATTAAGAAGATCG
TATTCATTTTGACGGTTAAAGGGGGCTGCACGTACACCTTCTGTAGTTACTGACTTA
TTTGACCCTGAACTAATCCTAATGCTAATGGATACCTTGATAAATTAGCCCAAGAGC
TCGGTCGAAAGTTTACAAATGAAGAGGGAGAAGTAATTGTAGACCAATTCTTAATTTG
TCTTGGAGCTGGTGGTGGCGTTGGAACAGGTTGGGGTTCACCTGTTTTACAATTAAT
TCGTGAACAGTTTTTCCCTTGTCCAGTATCTATGCTTATTTCTTTACCATCCGGTGAT
CCTGATGAAATTAACAATGCACTTGTATTACTAAGTGAATTGATGAATTTATGAGAG
AGCAAGACAGATTATTTGAAATTCGATATAAAGCCTTAGCAAATGTAATTGTAAAT
GATAATACGCAAATGCAACGTATAATTGAGTCACAAAAGGCACGAAAGATCTGAAAA
ACAGATATGTAACTGGAAAGAAGTTGCGAACGATAATGTAGTGAGTACTTTACATGA
AATAAACATAATCCCAGAGAACTATGGTTCTGATAACGTTACATACGCCATCGGAT
TTAATAAAACTATTAAGTATTCCAGGACGTTTCTTACAAATTGAAAAGCGAGAATTG
CTAAATTCGATTTACATTCACCTTGAAAATAGTATTAACGAAGCTTAGATGAGGGATT
CTTCTCAGCGAACATCAATTTGAAACAGCAACAATGTATGGTGGTTTTCGTTTTAAGA
CCTTCTAACGCAGACTTCTTCAAAGATGTTAATACGAAAATAGAATTCGTAATACCT
TAGGAGAGTATAAACGATTAGATGAAATCGCTGGTAAATTTGGAGATCCAATTTGGGA
TAATGAATATGCGGTTTGCTACACTATATTTGCTGGTATGACAATGCCTAAACGCTAT
ATATCTTTGCGCGAGAAGGAAAAGAGTTGGCTGAAAAACAAGAGCAATTAAGAGCA
GAAGCTCAACGTAACAGGACGAAGAAAAAGTAGATATTTCTTTTGCAACAAATCGTG
```

TTCAAAAAACACATTCAATCCTTATAATAAAAAACCAAGGATTTGGCGGGGCATCAAG
 ATTCAGTGGTGGTAAAACTCTGCATTTAAACGTCAGACTAGTGAAGCTACTTCAACA
 CAAAATCAACAAGAAGAAGAGAATATTATTAGCACTCTTAAAACTTCAAATCCATTTAA
 AAAACGTTAACAAAGCCCAGAAAGGAAGCTGAGTTGGCTGCTGCCACCGCTGAGCAAT
 AACTAGC

sequence of optimized tubZ construct

TAATACGACTCACTATAGGGGAATTGTGAGCGGATAACAATCCCCTCTAGAAATAAT
 TTTGTTAACTTTAAGAAGGAGATATACATATGGCTAGCATGACTGGTGGACAGCAA
 TGGGTATGTTACTAACTCAAATGAATTGGAGCACATCCATTCCACTAACCACAGCGT
 CAACGACATTTCTATCCGTTGGGGTGTATTGGTGCTGGTCAGAAAAGGTAATAAGGA
 GGCGGATCTTTCGCGGGTTACAAGTTCAGCAATGGTACCACCTGCTACCCGACGCT
 GGCGGTCAACTTTGCGGAATCAGATATGATGCATCTGCAGAACATTATCAAGGAGGA
 TCGTATCCACTTTGATGGTCTGAAGGGGGCAGCACGTACACCGTCTGTTGTGACCGA
 TCTGTTGACCCGAAAACCCGAATGCTAACGGCTATCTGGATAAATTGGCGCA
 AGAGCTGGGCCGTAAGTTCACCAATGAAGAAGGCGAGGTTATCGTGGACCAGTTCCT
 GATTTGCCTGGGCGCAGGTGGCGGTGTGGGTACCGGCTGGGGCAGCCTTGTCCCTG
 CAACTGATTCGGGAGCAGTTTTTTCCGTGCCCCGTTTCAATGCTGATAAGCTTGCCG
 TCCGGCGATCCAGATGAGATTAACAACGCACTGGTTCTGCTGAGCGAGATCGATGAG
 TTTATGAGAGAACAAGATCGCTTGTTCGGCAACTCCGACATCAAACCGCTGGCGAAC
 GTGATCGTTAATGACAATACCCAAATGCAGCGTATCATTGAAAGCCAGAAGGGTACAA
 AAGATCTTAAGAACCGTTACGTGAACTGGAAGAGGTGGCCAATGACAATGTTGTAA
 GCACCTTGATGAAATCAACATCATTCCGGAGAATTACGGTTCTGACAACGTGACCTA
 TGATCCATCTGACTTGATCAAGCTGTTATCGATCCCGGGTCGTTTTCTGACCATTGGT
 AAGGCACGTATTGCGAAATTCGATCTCCACAGCCTGGAAAATCCATTAAACGTAGCT
 TGGACGAAGGTTTCTTCAGCGCCGAGCACCAGTTTGAAACCGCAACGATGTATGGTG
 GCTTCGTGCTGCGTCCGAGCAATGCTGACTTCTTCAAGGACGTTAACACGGAAAACC
 GCATCCGCAATACCCTGGGCGAATACAAGCGTCTGGACGAGATTGCTGGCAAATTCG
 GCGACCCGATTTGGGATAACGAGTATGCGGTGTGTTACACCATTTTTGCGGGCATGA
 CCATGCCGAAACGCTACATTAGCTTGGCGCGGAGGGTAAAGAACTTGCTGAGAAAC
 AAGAACAACCTGCGTGCGGAGGCTCAACGCAAGCAGGACGAGGAAAAAGTGGACATC
 TCGTTGCCACGAACCGCGTTCAGAAAAACACGTTTAACCCTTATAACAAGAATCAGG
 GTTTCGGTGGCGCCAGCCGTTTTTCGGGTGGCAAAAACAGCGCGTTAAGCGCCAG
 ACCAGCGAAGCTACCTCCACCCAAAACCAGCAAGAGGAAGAGAATATCATCTCGACT
 CTGAAAACCTCTAACCCGTTAAGAAACGTTAACAAAGCCCGAAAGGAAGCTGAGTTG
 GCTGCTGCCACCGCTGAGCAATAACTAGC

sequence of tubR construct

TAATACGACTCACTATAGGGGAATTGTGAGCGGATAACAATCCCCTCTAGAAATAAT
 TTTGTTAACTTTAAGAAGGAGATATACATATGGCTAGCATGACTGGTGGACAGCAA
 TGGGTatgAATAGGGATCACTTTTATACGTTAAACATTGCAGAAAATTGCAGAAAGAATT
 GGTAATGATGATTGTGCTATCAAGTATTAATGGCATTATCAATGAAAATGGTGAAG

CGCAAATGCTGAATAAAACGGCTGTGGCAGAAATGATACAGCTAAGTAAACCGACTG
TTTTTGCAACCGTAAATAGTTTTTATTGTGCgGGATATATTGATGAAACTAGGGTAGG
AAGGTCTAAGATTTATACCTTATCGGATTTAGGTGTAGAAATAGTAGAGTGTFTTAAA
CAAAAAGCAATGGAAATGCGTAATTTATAACAAAAGCCCGAAAGGAAGCTGAGTTGGCT
GCTGCCACCGCTGAGCAATAACTAGC

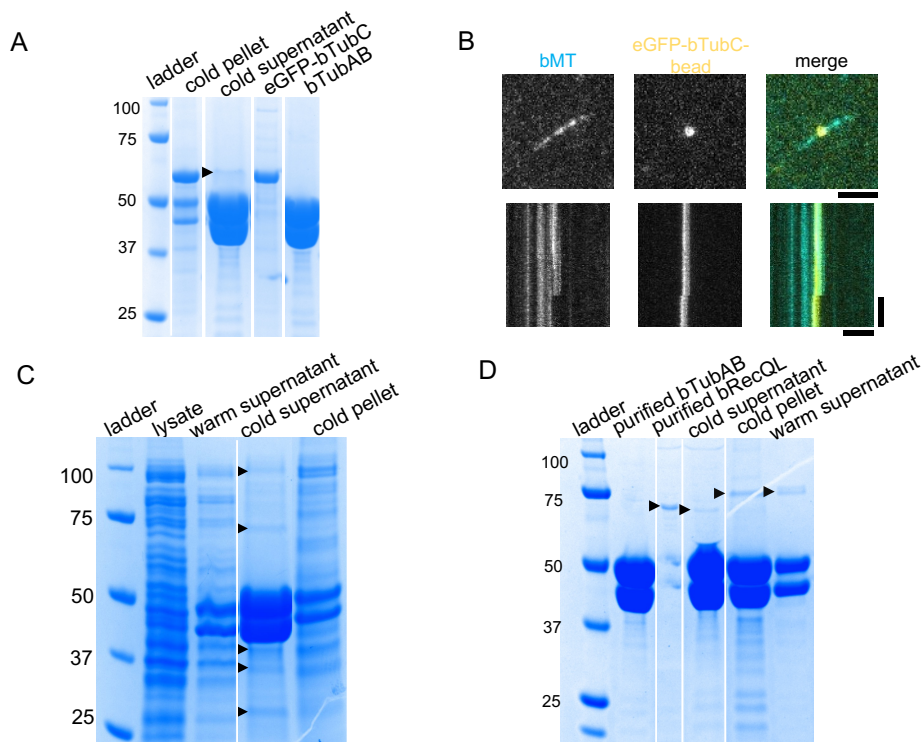


Figure S1: **Bacterial microtubule-associated proteins:** (A) Coomassie-stained protein gel of the co-sedimentation assay of $85\mu\text{M}$ bTubAB and $2.6\mu\text{M}$ eGFP-bTubC loaded with the pellet ("cold pellet") and supernatant ("cold supernatant") after high-speed centrifugation on an ice-cold rotor (after bMTs depolymerization). For comparison, purified proteins were loaded on the gel. We observed eGFP-bTubC (marked with arrowheads) both in the supernatant and in cold pellet. (B) (top) A TIRF image of the interaction of a polystyrene bead coated with eGFP-bTubC (yellow) with a bMT (cyan). (bottom) A kymograph of an eGFP-bTubC coated bead displacement while following the depolymerization of a bMT. scale bars: horizontal = $5\mu\text{m}$, vertical = 30 s. (C) Coomassie-stained protein gel of possible adapter proteins expressed naturally in the *Prostheco bacter debontii* after co-sedimentation with $85\mu\text{M}$ bTubAB with $40\mu\text{l}$ of the lysate in the presence of GTP. The arrowheads mark the bands which were analyzed with mass spectrometry. The large number of bands in "warm supernatant" and "cold pellet" indicates that most of the proteins have no binding affinity to bMTs and either remained in the solution or were in aggregation form, respectively. (D) Coomassie-stained protein gel of a co-sedimentation assay of $1\mu\text{M}$ purified bRecQL and $83\mu\text{M}$ bTubAB. The arrowheads show the bRecQL in different lanes. Sharper bRecQL bands in "cold pellet" and "warm supernatant" compared to "cold supernatant" shows weak interaction.

4

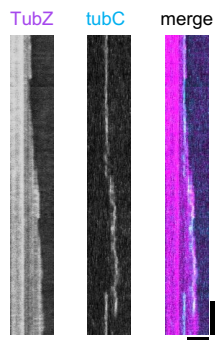


Figure S2: **TubZ and tubC interaction in the absence of TubR:** (A) Kymograph depiction of the interaction between a TubZ filament and tubC in the presence of $1\ \mu\text{M}$ TubZ and $100\ \text{pM}$ tubC. tubC centromeric DNA diffuses on the filament lattice in the absence of TubR. scale bars: horizontal = $5\ \mu\text{m}$, vertical = 1 min.

5

In vitro RECONSTITUTION OF FORCE-GENERATING PHUZ FILAMENTS

Catalina IJSPEERT^{*}, Reza AMINI HOUNEJANI^{*}, and Marileen DOGTEROM

The only true wisdom is in knowing you know nothing.

Socrates

PhuZ proteins have been shown to assemble into a head-to-tail polar structure displaying dynamic instability. It has been shown that the plus ends of PhuZ filaments exert pushing forces for phage nucleus positioning while the minus ends are anchored at the cell poles. Employing microfabricated barriers we repeated the stalling assays to investigate the effect of pushing forces on the dynamics of PhuZ filaments. Here we show that growth-opposing forces enhance catastrophes for a dynamic PhuZ filament which results in less stable PhuZ filaments. We hypothesize that at high PhuZ concentrations, minus end growth in combination with an unstable plus end may lead to treadmilling PhuZ filaments. While studying dynamics of PhuZ filaments, we observed unexpected aster-like structures of PhuZ bundles which may help us to better understand the process of phage nucleus positioning inside the host cells.

5.1. INTRODUCTION

Microtubules (MTs) and microtubule-like filaments are fundamental to intracellular organization and transport. For instance, MTs are involved in nucleus positioning and the transport of cell polarity factors in fission yeast cells [108]. Moreover, it has been shown that viruses of eukaryotes recruit MTs to traffic towards the cell nucleus, where they exploit the host cell replication machinery to replicate their DNA [28, 36]. Tubulin-like proteins such as bTubAB from *P. dejongei* and TubZ from *B. thuringiensis* form dynamic filaments with features closely related to microtubules [9, 31, 43, 110]. A phage-encoded tubulin-like protein (PhuZ), which forms a unique three-stranded dynamic filament, has been shown to facilitate phage nucleus positioning and capsid trafficking during cell infection (Figure 5.1) [23, 24, 122, 135]. PhuZ has been shown to be conserved among some *Pseudomonas* jumbo phages e.g., 201 ϕ 2-1, ϕ KZ, and ϕ PA3 [21].

Upon DNA injection into the host cell in the initial stages of phage infection, a self-assembling proteinaceous shell forms around the phage DNA to protect it from the host CRISPR-Cas and any other immune mechanism which targets DNA [24, 94]. Meanwhile, polar PhuZ filaments (with a more dynamic plus end and a minus end which anchors at the cell poles) form the so-called phage spindle (Figure 5.1B) [41, 77], a behavior which is reminiscent of the mitotic spindle setup by eukaryotic microtubule organizing centers (MTOCs) [129]. The so-called phage nucleus is then positioned to the center of the cell by pushing forces exerted by growing PhuZ plus ends. It has been shown that during phage nucleus positioning, PhuZ filaments display the dynamic instability behavior [23, 41]. Dynamic instability, which is a characteristic property of eukaryotic microtubules, refers to the random transition between growth and shrinkage of a filament. During growth, GTP-bound subunits are being added to the tip of the filament upon which the incorporated GTP-tubulin hydrolyzes to GDP-tubulin. The intrinsic time-difference between the two events creates a GTP-enriched region at the growing tip of the filament which is called a GTP-cap. It is now well established that the stability of the filament is compromised as the GTP-cap is lost and the filament exhibits a transition to shrinkage, an event termed a catastrophe [57].

Dynamic PhuZ filaments generate pushing forces which drive a unique rotation in the centered phage nucleus [22]. The phage DNA is being replicated utilizing host cell replication machinery inside the phage nucleus while it is rotating in the cell center. Later in the infection process, capsids, which have formed on the cell membrane, are transported to the cell center where they dock on the rotating nucleus for newly replicated phage DNA encapsulation utilizing the PhuZ pathway [23]. It has been observed that the PhuZ filaments switch from dynamic instability to treadmilling to facilitate capsid transport [23]. During treadmilling, subunits are being added to one end and removed from the other end of a filament simultaneously. Non-confined treadmilling PhuZ filaments may grow at their plus ends and shrink at their minus ends, which results in an apparent motion towards the plus end of the filaments [41]. However, time-lapse fluorescence images of anchored PhuZ filaments, confined between the cell pole and the phage nucleus, have suggested that PhuZ filaments exhibit a backward treadmilling which is a result of minus end growth and plus end shrinkage. This creates

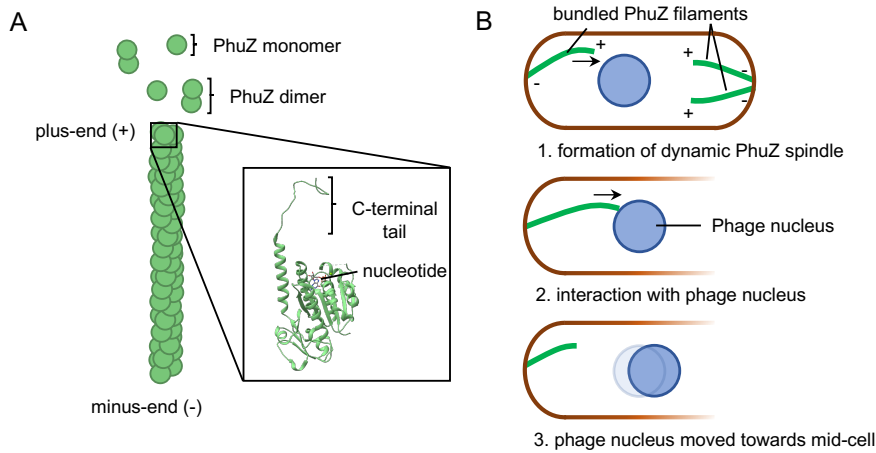


Figure 5.1: **Structural properties of PhuZ filaments and their role during phage infection *in vivo*.** (A) Schematic depiction of the 3-D structure of a PhuZ filament and the single protein X-ray structure of the PhuZ from phage 201 ϕ 2-1 [77]. PhuZ assembles into a helical three-stranded filament by the polymerization of GTP-bound monomers and dimers. Subunits are oriented such that the C-terminal tails are exposed at the plus-end of the filament. (B) Schematic depiction of PhuZ filaments contributing to nucleus positioning *in vivo*. Upon phage infection, PhuZ is expressed and assembles into a dynamic spindle extending from the cell poles. The filaments, albeit bundled, are directed with their plus-ends towards the mid-cell and exhibit dynamic instability. By the interaction of the two opposing dynamically unstable PhuZ bundles with the phage nucleus, the phage nucleus is ultimately positioned at mid-cell, followed by further continuation of the infection process.

a net movement towards the cell center [23]. Although Kraemer et al. [77] originally suggested a critical role for the phage spindle and PhuZ filaments in the efficiency of phage production, more recent work has proposed "only a modest impact" [56].

In this chapter, we study some of the unique dynamic features of PhuZ filaments that are essential for their biological role. Using *in vitro* reconstitution assays, we determined the dynamic instability properties of PhuZ filaments. We also observed treadmilling, annealing, and bundled PhuZ filaments. We observed that unlike other tubulin-like filaments, PhuZ filaments are more prone to bundle in a parallel fashion which may assure unidirectional capsid transport inside host cells. Moreover, to assess the effect of pushing forces generated during phage nucleus positioning on the dynamics of PhuZ filaments, we performed barrier experiments similar to experiments previously performed with eukaryotic MTs [66, 74] and bacterial MTs in Chapter 3 of this thesis. Analysis revealed that similar to eukaryotic and bacterial MTs, an obstacle may stall PhuZ filament growth and enhance catastrophes resulting in unstable plus ends. At a high PhuZ concentration, minus end growth was observed as well. This leads us to hypothesize that at a high PhuZ concentration the dynamic instability phase may switch to treadmilling by stalling growth at the plus end and allowing growth at the minus end.

5.2. RESULTS

In vitro RECONSTITUTION OF DYNAMIC PHUZ FILAMENTS

To study the dynamics of isolated PhuZ filaments, *in vitro* experiments were performed both in the presence and absence of GMPCPP-stabilized seeds using total internal reflection fluorescence microscopy (TIRFM). In the absence of PhuZ seeds, 4 μM PhuZ (20% Cy3-labeled, 1% biotin-PhuZ, and 80% unlabeled) in the presence of 4 mM GTP was added to flow cells treated with α -casein. We observed that PhuZ forms dynamic filaments which exhibit net-growth at the plus-end of the filament and net-shrinkage at the minus-end or treadmilling (Figure 5.2A, left). Moreover, end-to-end annealing of two PhuZ filaments was observed (Figure 5.2A, right). These two features were reported previously by Erb et al. [41]. Treadmilling filaments occasionally seemed to fluctuate in length (Figure 5.2A, left - marked with arrows on the kymograph). We hypothesized that at higher PhuZ concentration the net shrinkage at minus end of filaments may turn to net growth which in turn causes the length increment during treadmilling. By increasing the PhuZ concentration, we indeed managed to observe minus end growth of GMPCPP PhuZ filaments (Figure 5.2B).

5

Erb et al. [41] showed that PhuZ filaments exhibit dynamic instability both *in vivo* and *in vitro*. To investigate the dynamic instability properties of these filaments, biotinylated GMPCPP-stabilized seeds were added to functionalized flow cells. The experimental setup is depicted schematically in Figure 5.2C. Initially, 1.3 μM Cy3-labeled PhuZ (20% labeled, 80% unlabeled) was polymerized in the presence of 4 mM GTP from immobilized Cy5-labeled seeds (20% Cy5-labeled, 5% biotin-PEG-labeled, 75% unlabeled, $[\text{PhuZ}] = 2 \mu\text{M}$). PhuZ filaments grew from the seeds and dynamic instability was observed. However, GMPCPP PhuZ seeds depolymerized within about 5 min, substantially limiting the time duration and accuracy of the acquisitions.

While analyzing dynamics of filaments growing from immobile seeds, unexpected aster-like structures from which PhuZ filaments could radially grow were observed (Figure 5.2D). Although GMPCPP PhuZ seeds were relatively unstable, these aster-like bundled PhuZ seeds were observed to increase the stability of the seeds (Figure 5.2D; also see Figure 5.3C). To further examine the formation and behavior of these structures we repeated the single-color experiments (without seeds) with different concentrations of PhuZ in the presence of either GTP or GMPCPP on a surface with or without biotin-PhuZ (see single-color assays on section 5.4). First, our observations revealed that surface attachment is necessary for these structures to form as no aster-like structures were observed in the absence of biotin-PhuZ (Figure 1.2E). In addition, the number of these aster-like structures increased by increasing the PhuZ concentration (Figure 5.2E). 5 μM GTP-PhuZ with a trace amount of biotin-PhuZ (1%) on a surface treated with Neutravidin, on the other hand, formed dynamic aster-like structure where treadmilling filaments emerged from an apparent point-source (Figure 5.2F). This was only observed at PhuZ concentration higher than or equal to 5 μM .

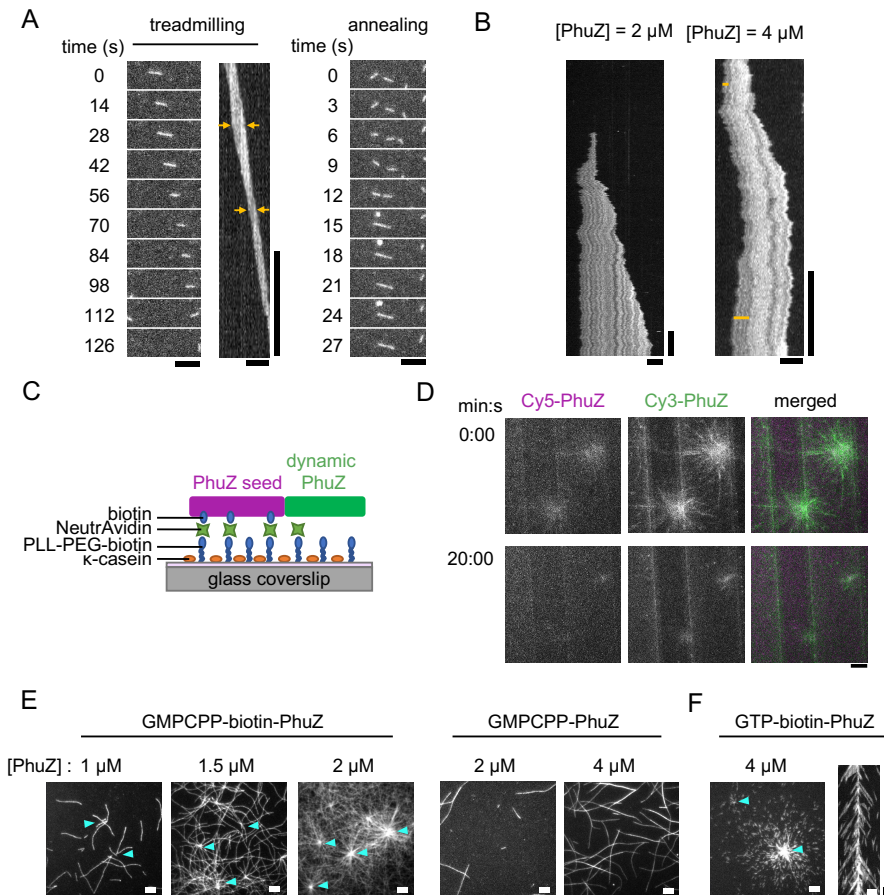


Figure 5.2: *In vitro* reconstitution of dynamic PhuZ filaments: (A) A time series image of a PhuZ filament in 4 μ M GTP-PhuZ that exhibits treadmilling and the time-position graph (kymograph) of the same filament. The arrows indicate differences in length of the treadmilling filament. (right) A time series image of an end-to-end annealing event of two treadmilling filaments in 4 μ M GTP-PhuZ. (B) Kymographs of treadmilling filaments at different GMPCPP-PhuZ concentrations. While no minus end growth was observed at 2 μ M GMPCPP-PhuZ, at 4 μ M minus end growth is visible as marked by yellow lines of different lengths. (C) Schematic depiction of dual-color PhuZ assays. A glass surface is treated by PLL-PEG-biotin, Neutravidin, and α -casein. Stabilized seeds which are labeled with biotin are immobilized on the surface and dynamic PhuZ filaments grow from them. (D) TIRF images of dual-color assays in the presence of GMPCPP-seeds. The aster-like structures expand the lifetime of the GMPCPP-seeds (magenta). Dynamic PhuZ filaments (green) grow radially from these bundled seeds. A Kalman Stack Filter plugin <https://imagej.net/plugins/kalman-stack-filter> in ImageJ is used to improve the resolution of the image. (E) TIRF images of different concentration of GMPCPP-PhuZ filaments in the presence and absence of surface attachment. In the presence of surface attachment, aster-like structures form and the number of them increase by increasing the PhuZ concentration. However, in the absence of biotin-PhuZ and thus surface attachment, no asters form even at high PhuZ concentrations. (F) A TIRF image of a dynamic aster-like structure formed by GTP-PhuZ in the presence of surface attachment (left) and a kymograph of a random line along the aster which shows how tiny treadmilling PhuZ filaments emerge from an apparent point-source (right). The kymograph is drawn from the aster-like structure on top left of the left image. Scale bars: horizontal = 5 μ m, vertical = 20 s.

EGS-STABILIZED SEEDS ENABLE EXTENDED IMAGE ACQUISITION

Unstable GMPCPP seeds led to detachment of the filaments from the surface in the dynamic instability experiments (Figure 5.3B and C). To be able to study the dynamic instability of PhuZ over a longer time span, we developed a protocol based on a method described by Fanara et al. [42]. By employing this method, we additionally stabilized GMPCPP-PhuZ seeds with the chemical crosslinker ethylene glycol bis (succinimidyl succinate) (EGS) (Figure 5.3A). A GMPCPP-PhuZ mixture (0.5 mM GMPCPP, 20% Cy5-labeled, 5% biotin-PEG-labeled, 75% unlabeled, [PhuZ] = 2 μ M) was immediately thoroughly mixed with EGS at a final concentration of 0.375 μ M. The PhuZ-EGS mixture was incubated first on ice and then at room temperature to allow for proper filament nucleation followed by further filament growth and lattice crosslinking (see Methods and Materials section). Finally, the crosslinking reaction was quenched by mixing the solution with a quenching buffer, containing K-glutamate. EGS-stabilized GMPCPP-PhuZ seeds were freshly prepared each day prior to experiments. We observed that additionally crosslinking GMPCPP-PhuZ yields sufficiently stable seeds (stable throughout 1 h of overall image acquisition) which can nucleate filaments for an extended time interval compared to non-crosslinked seeds. PhuZ filaments were observed to polymerize from these EGS-seeds and display dynamic instability (Figure 5.3D).

5

GROWTH TIMES OF PHUZ FILAMENTS ARE EXPONENTIALLY DISTRIBUTED

To determine the parameters of dynamic instability of PhuZ filaments, we analyzed the kymographs of 1.3 μ M Cy3-labeled PhuZ (20% labeled, 80% unlabeled) nucleating from EGS-stabilized seeds in the presence of 4 mM GTP (Figure 5.4A). These experiments were done in the presence of micro-fabricated barriers yet away from any barrier. Kymographs showing variations in intensities, which indicate the presence of a bundle of filaments, were excluded from analysis. We found that single PhuZ filaments show a relatively high (higher than MTs [74]) average growth speed of $2.77 \pm 0.06 \mu\text{m min}^{-1}$ (Table 5.1). The average growth time, the time interval a filament spends in the growing state before a catastrophe, was 46 ± 2 s (mean \pm SEM). Some growth events were too short for growth speed analysis (due to the size of the filaments). However, to obtain a representative distribution of PhuZ growth times, these events were still included for PhuZ growth time measurements (Figure 5.4B). We fitted the growth times with an exponential fit, yielding an R-squared equal to 0.98 for a linear fit to the cumulative distribution at short times (Figure 5.4 C and D).

STALLING AT A BARRIER ENHANCES PHUZ FILAMENT CATASTROPHES

To gain insight into the effect of force on the dynamics of PhuZ filaments (such as relevant during phage nucleus positioning), we performed *in vitro* dynamic assays with in-house designed rigid micro-barriers fabricated onto a glass coverslip according to a protocol described in Chapter 2 and [74]. This design allows for high-resolution imaging of filament behavior upon barrier contact using TIRFM (Figure 5.5). We polymerized 1.3 μ M PhuZ from immobilized EGS-PhuZ seeds in the presence of 4 mM GTP (data acquired from samples in previous section). Upon barrier contact, we observed three types of events, *i.e.* stalling, sliding and sliding followed by breakage of the filament (Figure 5.5C). Stalling and sliding filaments were most often observed; however,

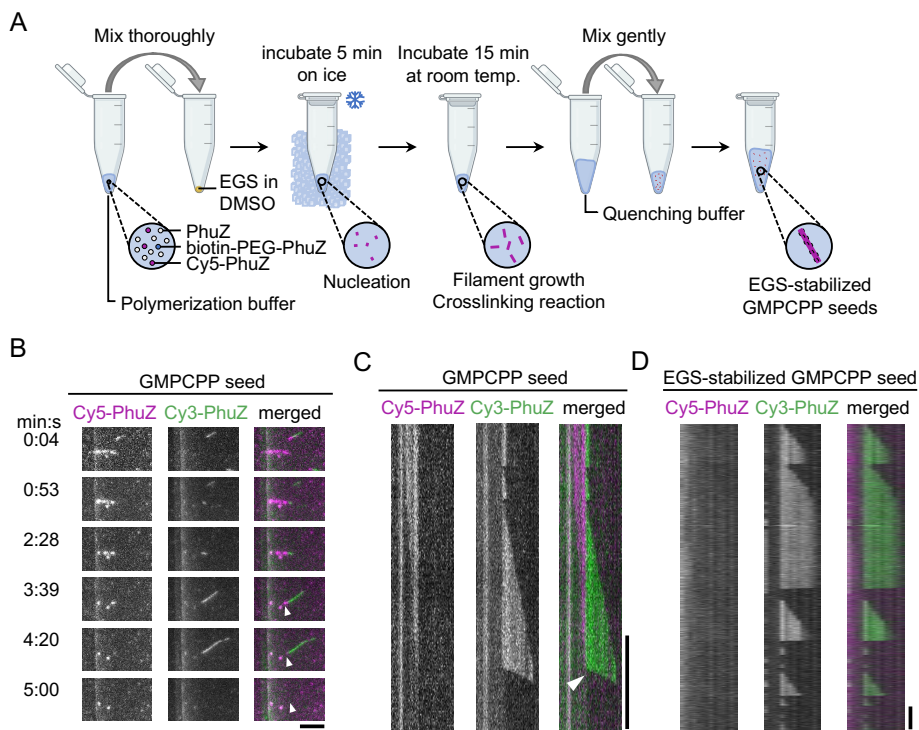


Figure 5.3: EGS-stabilized seeds enable extended image acquisition: (A) Schematic sketch of protocol for stabilizing GMPCPP-PhuZ seeds with ethylene glycol bis (succinimidyl succinate) (EGS) (see Materials and Methods). (B) A time series image of a dynamic PhuZ filament (green) polymerizing at $1.3 \mu\text{M}$ GTP-PhuZ from an unstable GMPCPP-PhuZ seed (magenta). Arrowheads indicate the depolymerizing minus-end of the GMPCPP-PhuZ seed. GMPCPP-seeds depolymerize on average within 5 min from the beginning of imaging. (C) Kymograph of the filament corresponding to (B), showing full depolymerization from the minus-end of the nucleated filament after full depolymerization of the GMPCPP seed. (D) A kymograph image of a PhuZ filament (green) polymerizing at $1.3 \mu\text{M}$ GTP-PhuZ from an EGS-stabilized GMPCPP-PhuZ seed (magenta). Scale bars: horizontal = $5 \mu\text{m}$, vertical = 60 s.

interestingly, we did not observe any buckling events possibly due to very short contact times. Buckling for a filament like a microtubule happens when the filament keeps growing even after it reaches the obstacle without sliding [35]. To assess the stalling behavior of PhuZ filaments, we analysed the kymographs of stalling filaments and measured the time duration of the barrier contact before catastrophe, called contact time. We found that PhuZ filaments stall for an average time duration of 8.3 ± 0.6 s (mean \pm SEM) (Table 5.1). We also employed the MT one-dimensional model which we used for bacterial microtubules in Chapter 3 aiming at reconciling the growth and contact times of PhuZ filaments; however, no significant correlation was found between the simulations and experimental results.

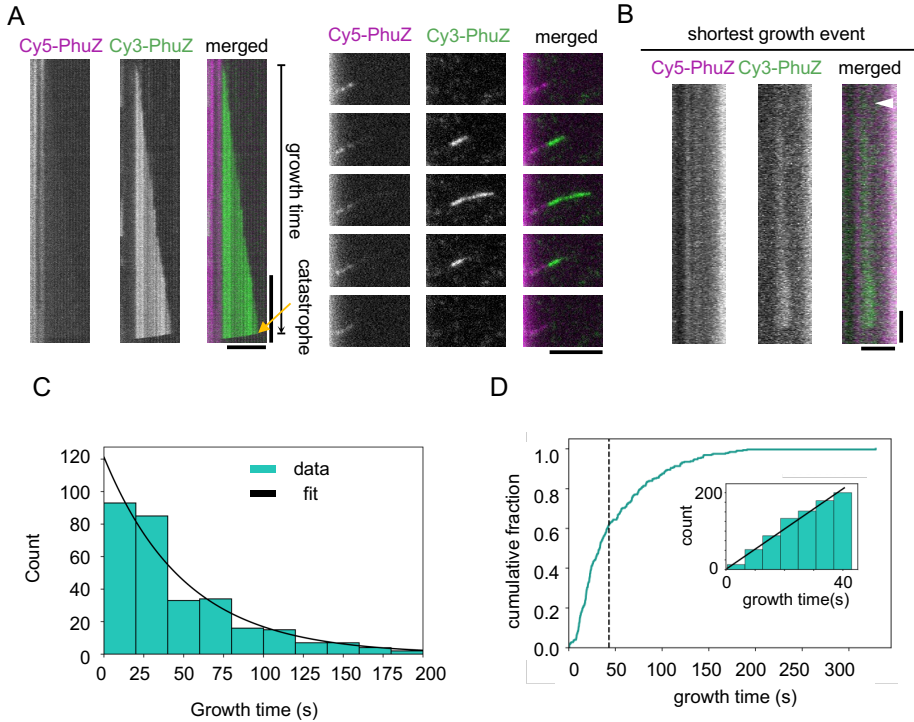


Figure 5.4: **Growth times of PhuZ filaments are exponentially distributed:** (A) (left) A kymograph of a freely growing PhuZ filament at 1.3 μM GTP-PhuZ (green) polymerizing from an EGS-stabilized GMPCPP PhuZ seed (magenta), exhibiting dynamic instability. PhuZ growth times are measured as the time interval between nucleation and the onset of catastrophe of the filament. (right) The corresponding time series image of the kymograph on the left. A Kalman filter is used for the time series image to improve the resolution of the image. Scale bars: horizontal = 5 μm , vertical = 30 s. (B) A kymograph of the filament corresponding to the shortest measured PhuZ growth time (450 ms) (marked with the arrowhead). Although impossible to precisely measure the growth rate for these filaments, the growth times were long enough to include in the dataset of growth times. Scale bars: horizontal = 2 μm , vertical = 3 s. (C) Histogram of experimentally measured PhuZ growth times fitted with an exponential curve (black). (D) Cumulative distribution of PhuZ growth times. (inset) Cumulative counts of short growth times (≤ 48 s) are fitted with a linear regression ($R^2 = 0.98$).

5.3. DISCUSSION

In this chapter, we investigated the dynamics of PhuZ filaments to better understand their role in localization of the phage nucleus and the transport of capsids in their host cell. Treadmilling and end-to-end annealing of PhuZ filaments were observed in our experiments as reported previously [41]. Both features have been observed for MTs as well [115, 132]. In addition, when interacting with the surface, PhuZ filaments form aster-like structures which seem to stabilize the GMPCPP-PhuZ seeds. Relatively unstable PhuZ GMPCPP-stabilized seeds were stabilized using an old MT seed stabilizing technique involving EGS crosslinkers. With this technique, the analysis of PhuZ dynamics analysis was possible over a longer time span. By using these longer image

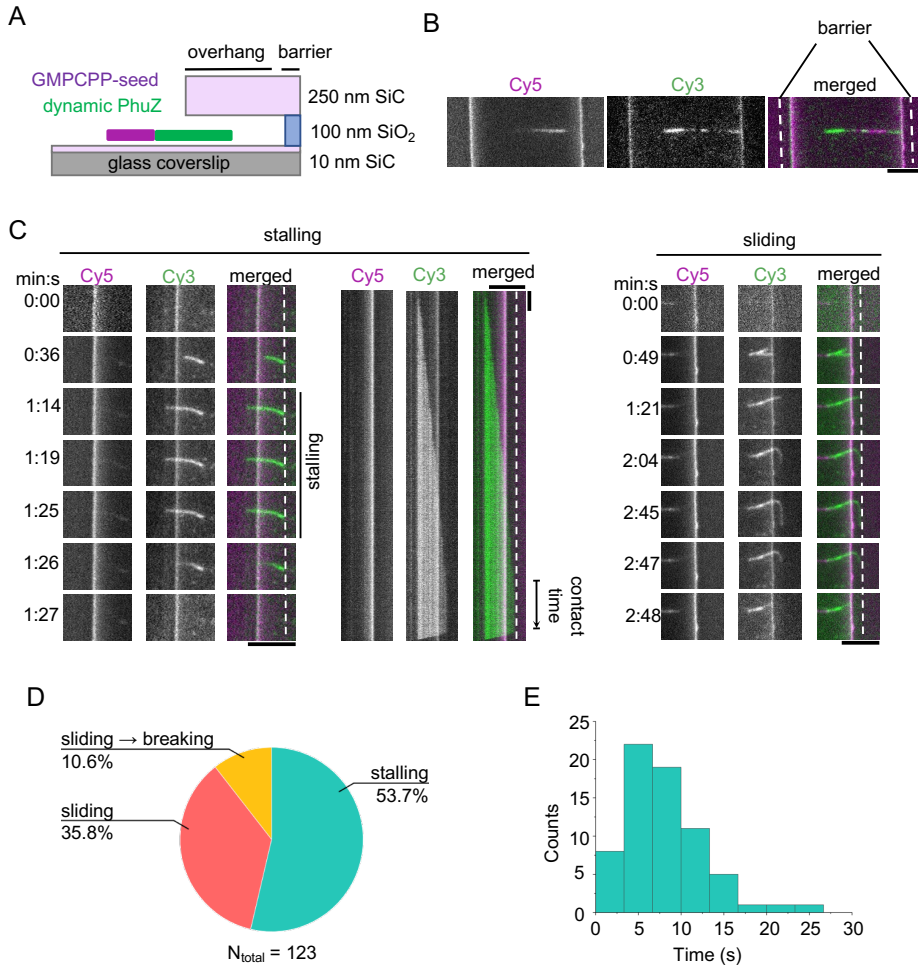


Figure 5.5: Stalling at a barrier enhances PhuZ filament catastrophes: (A) Schematic depiction of the experimental setup to study the behavior of PhuZ filaments upon barrier contact. Flow channels are made with coverslips onto which microbarriers have been fabricated prior to experiments. GTP-PhuZ filaments (green) nucleate from immobilized EGS seeds (magenta) and polymerize towards the barrier. (B) A TIRF image of a sample as shown in (A). Dashed lines indicate the position of the barriers. Bright vertical lines in the TIRF image are the edges of the overhang. (C) A time series image of a PhuZ filament stalling at a barrier and the corresponding kymograph (left). Stalling duration, which is called contact time, is marked with lines. A time series image of a PhuZ filament sliding upon barrier contact. Dashed lines mark the barriers. (D) Observed occurrences of stalling ($n = 68$), sliding ($n = 44$) and sliding followed by breaking ($n = 13$) events of PhuZ filaments upon filament-barrier contact. (E) A histogram of experimentally observed PhuZ filament contact times. The average contact time equals 8.3 ± 0.6 s (mean \pm SEM). Scale bars: horizontal = $5 \mu\text{m}$, vertical = 5 s. To improve the resolution of the images, a Kalman filter is applied to the TIRF images.

Table 5.1: **Characteristics of PhuZ filaments in comparison to eukaryotic microtubules:** The assays were done at 1.3 μM PhuZ and 15 μM eukaryotic tubulin in the presence of barriers. PhuZ shows higher growth speed and catastrophe frequency, and shorter lifetime and contact time compared to MTs. Additionally, stalling PhuZ filaments show an increased catastrophe frequency compared to free PhuZ filaments. The values are: growth speed for PhuZ filaments: mean \pm SEM, and for MTs: mean \pm std; growth time and contact time for PhuZ filaments: mean \pm SEM, and for MTs: median \pm SE. MTs data from [74].

	growth speed ($\mu\text{m}/\text{min}$)	shrinkage speed ($\mu\text{m}/\text{min}$)	catastrophe frequency free (min^{-1})	catastrophe frequency stalling (min^{-1})	growth time (s)	contact time (s)
MTs	1.7 ± 0.7	-	0.39 ± 0.04	1.95 ± 0.17	155 ± 15	30.8 ± 1.3
PhuZ	2.77 ± 0.6 (n = 263)	133 ± 4	1.39 ± 0.09 (n = 323)	7.3 ± 0.9 (n = 68)	46 ± 2	8.3 ± 0.6

stacks, the dynamic properties of PhuZ filaments could be measured. We showed that they are generally faster growing and more dynamic compared to eukaryotic and bacterial microtubules (Table 3.1 and Table 5.1 of Chapter 5). Moreover, we found that the interaction with a rigid obstacle enhances the catastrophe frequency of dynamic PhuZ filaments. This property was also reported for MTs and bMTs [74] (Chapter 3).

Our data show that even at a higher growth speed compared to MTs and bMTs, the growth time of PhuZ filaments is much shorter (46 ± 2 s) than that of MTs (155 ± 15 s) and bMTs (173 ± 10 s; see Chapter 3). The growth time distribution of freely growing PhuZ filaments follows an exponential distribution function. An exponential growth time distribution indicates that these filaments undergo catastrophes randomly. This random catastrophe behavior is similar to the behavior of bacterial microtubules (Chapter 3), while catastrophes for eukaryotic microtubules appear age-dependent for short growth times resulting in a gamma-like distribution [48]. In addition, we showed that the interaction with a rigid obstacle enhances the instability of PhuZ filaments by nearly sevenfold resulting in an average contact time of 8.3 ± 0.6 s. This contact time is relatively short compared to 30.8 ± 1.3 s for MTs [74] and 27.9 ± 1.6 s for bMTs (Chapter 3), and suggests that on average a PhuZ filament may push a phage nucleus only for several seconds towards the cell center. A possible explanation for this short contact time could be that the GTP cap of a PhuZ filament is much easier lost than that of a MT or a bMT.

A short contact time may not be efficient for positioning of the phage nucleus inside a bacterial dense environment. However, our experiments showed that bundling increases the stability of PhuZ filaments. *In vivo*, bundling of PhuZ filaments may thus compensate for the short contact times of dynamically unstable individual PhuZ filaments. In the presence of surface attachment, we observed unique structures formed by spontaneous PhuZ filaments bundling, which for MTs has only been reported in the presence of associated crosslinker proteins (Figure 5.2) [60]. On a surface treated with Neutravidin, biotinylated GMPCPP-PhuZ filaments formed aster-like structures of bundled filaments (Figure 5.5). Erb et al. [41] showed that PhuZ proteins expressed in non-infected *P. chlororaphis* cells form short filaments throughout the cells. How-

ever, long PhuZ bundles form after phage infection while being anchored at the cell poles, indicating the importance of interaction with a surface and possibly a minus end stabilizer for the bundling and stability of filaments. By contrast GTP-PhuZ filaments formed asters which were much more dynamic. Small treadmilling filaments were observed to emerge from point-source-like spots at the center of these dynamic asters (Figure 5.2F). By increasing the PhuZ concentration, the number of these spots increased. The formation of the aster-like structures suggests that majority of the filaments bundle in a parallel manner. Bundling in a parallel way may facilitate unidirectional transport of capsids to the center of the cell [23]. The underlying mechanism of the parallel bundling and the formation of aster-like structures remains to be understood.

Chaikeratisak et al. [23] have reported that the concentration of PhuZ increases throughout the infection process. Based on our observations, we hypothesize that this might explain the treadmilling behavior in the capsid transport stage. It is known that a treadmilling filament grows from its minus end and shrinks at its plus end during capsid transport [23]. We showed that the interaction between a filament and a barrier, such as the shell, may induce filament shrinkage at its plus end (Table 5.1). Moreover, our results showed that only at higher PhuZ concentration, a PhuZ filament may grow from its minus ends (Figure 5.2B, right). Since the catastrophe rate of a stalling filament is independent of subunit concentration [66], at higher concentrations the filament experiences similar shortening at the plus end while it is growing at the minus end, resulting in treadmilling. The minus end-membrane interaction at the cell pole remains to be identified, which could include adapter proteins to stabilize this end.

5.4. METHODS AND MATERIALS

In the experiments presented below, all the ingredients other than the proteins are dissolved in MRB80 (80 mM PIPES, 4 mM MgCl₂, 1 mM EGTA, pH 6.8) unless it is stated otherwise. However, the experiments are performed in BRB80 (80 mM PIPES, 1 mM MgCl₂, 1 mM EGTA, pH 7.2) background.

PROTEIN PURIFICATION

Protein purification and labeling was performed according to the procedure explained in Chapter 2. As mentioned in Chapter 2, PhuZ protein is stored in 50 mM HEPES-KOH pH 8.0, 250 mM KCl, 1 mM MgCl₂, 10% glycerol buffer.

STABILIZING PHUZ SEEDS WITH ETHYLENE GLYCOL BIS(SUCCINIMIDYL SUCCINATE) (EGS)

In order to form stable seeds that can function as nucleation sites, GMPCPP-PhuZ filaments were additionally crosslinked with the NHS ester ethylene glycol bis(succinimidyl succinate) (EGS) (Thermo Fisher Scientific), according to the following adaptation of the protocol by Fanara et al. [42], Koshland et al. [76]. 2 μ M PhuZ (80% unlabeled, 20% Cy5-labeled, 5% biotin-PEG-labeled), was supplemented with 100 mM KCl, 0.5% methylcellulose and 0.5 mM GMPCPP. The PhuZ mixture was immediately thoroughly mixed with EGS at a final concentration of 0.375 μ M and incu-

bated for 5 min on ice, followed by 15 min at room temperature in the dark. By adding EGS before polymerization, the amount of mixing was limited as much as possible, to yield maximum seed length. The crosslinking reaction/excess EGS was quenched diluting the crosslinked seed mixture into 200 μ l of quenching buffer, consisting 10 mM K-glutamate and 0.1 mM GMPCPP in BRB80 pH 7.2. Crosslinked seeds were used solely on the same day of preparation for dynamic assays.

SINGLE-COLOR ASSAY

Single-color assays were inspired by the single-color experiments described in [41]. A flow chamber was made with parafilm and base piranha-cleaned coverslips. The surface of the chamber was treated in three 10 min consecutive steps with 0.2 mg mL^{-1} PLL-PEG-biotin, 0.5 mg mL^{-1} Neutravidin, and 0.5 mg mL^{-1} α -casein at room temperature. In the assays done in the absence of surface attachment, the surface was treated with 0.2 mg mL^{-1} PLL-PEG followed by two times wash with imaging buffer (0.5 mg mL^{-1} α -casein, 100 mM KCl, and 0.5% methyl-cellulose) with 10 min incubation. In both cases, following each step, the channel was washed two times with BRB80 pH 7.2. The reaction mix with different protein concentrations was made in imaging buffer in the presence of 4 mM GTP and the oxygen scavenging mix (Chapter 2) was added to the channel. The channel was sealed with vacuum grease and imaged immediately.

DUAL-COLOR ASSAY

Dual-color assays were done with the coverslips containing barriers. Flow chamber preparation is described in Section 2.3 of Chapter 2. For dual-color assays, EGS-stabilized seeds were diluted twice in imaging buffer and subsequently introduced to the functionalized channel. After incubating the seeds in the channel for 5 min at room temperature, the reaction mixture, containing 1.3 μ M PhuZ (80% unlabeled, 20% Cy3-labeled) supplemented with 4 mM GTP and oxygen scavenger mix in imaging buffer, was consecutively added to the channel. Lastly, the flow channels were sealed with vacuum grease before subsequently imaging at ambient temperature with a TIRF setup.

IMAGING AND IMAGE ANALYSIS

TIRF image acquiring and analysis are described in Chapter 2. The TIRF setup used for stalling assays was equipped with a 140 mW 568 nm and a 110 mW 642 nm laser and the images were acquired in 2% and 5% of those laser powers, respectively. The exposure time was set to 50 ms. The light emitted from the specimen was collected at the outlet of a Nikon eclipse Ti2 microscope and split utilizing an OptoSplit II ByPass (Carin research). At the expense of smaller field of view, the splitter reduced the frame time to 75 ms by making simultaneous dual laser imaging feasible. Each field of view contained two images from the two lasers which prior to data analysis were aligned utilizing an image of a reference microscope slide containing Tetraspeck beads. The total magnification for dual- and single-color assays yielded a pixel size of 83 nm and 160 nm, respectively. Additionally, drift correction was performed using the ImageJ GDSC SMLM plugin <https://gdsc-smlm.readthedocs.io/en/latest/index.html>.

AUTHOR CONTRIBUTION

R.A.H. fabricated micro-fabricated barriers and ran the simulations. R.A.H. and C.IJ. performed experiments and analyzed the data. All authors wrote the paper. M.D. coordinated the project.

ACKNOWLEDGMENTS

We thanks Eli O. van der Sluis and Anne Doerr for protein purification and labeling. We thank Marie-Anne de Gier for her exploratory experiments at the beginning of the PhuZ project as part of her bachelor end project. This work was supported by The Netherlands Organization of Scientific Research (NWO/OCW) Gravitation program Building a Synthetic Cell (BaSyC) (024.003.019).

6

CONCLUSION AND OUTLOOK

In a living cell, various actions need to be undertaken to accomplish the growth and reproduction. For a reliable proliferation all the information in the genomic material of a cell should be transferred to the next generation. Several DNA segregation machineries have evolved into highly precise active mechanisms to ensure faithful gene transfer. Mitosis in eukaryotic cells, for instance, employs a highly controlled apparatus called the mitotic spindle to partition chromosomal DNA during cell division [91].

Bacterial cells possess simpler DNA segregation systems which include fewer components compared to the mitotic spindle. Active DNA segregation in bacterial cells is used to separate precious low copy plasmids. Interestingly, many of these plasmids encode for their own segregation systems. In *E. coli*, plasmid R1 encodes for an actin-like protein, namely ParM which forms double-stranded filaments. In the presence of the ParRC segrosome ParM filaments form aster-like structures. Interaction between two nearby asters enhances the ParM filament growth which results in segregation by pushing the plasmids to the opposite sides of the cell. Other minimal DNA segregation systems were discovered to be encoded by pBtoxis plasmid in *B. thuringiensis* [43, 82], c-st phage of *C. botulinum* [104], pBET131 plasmid in *B. subtilis* [10, 85] and many more.

In this thesis the central aim was to design a minimal DNA segregation system for synthetic cells. A synthetic cell includes a 3-D container (like a liposome) which hosts basic components for cell reproduction like a transcription-translation machinery. Our results provide feasible ideas for a hybrid system based on multiple bacterial cytoskeletal systems which may be externally controlled by light and which could be used for DNA segregation in a synthetic cell. Components of this hybrid system were examined for expression in PURE system and encapsulation in GUVs. We also studied each cytoskeletal system separately, focusing on their (biophysical) properties. Our findings provide insights to the structural and dynamic properties of bMTs, which also has relevance for eukaryotic MTs. A third prokaryotic cytoskeletal filament, PhuZ, was also

studied for its dynamic properties. Here we suggest a mechanism for the transition between the dynamic instability and treadmilling of PhuZ filaments during cell infection.

In Chapter 3 we compared different features of bacterial microtubules with eukaryotic microtubules. We showed that stalling forces generated by the interaction with an obstacle increase the catastrophe rate of bMT filaments which is in accordance with MT behavior under the same condition. The second major finding was that theoretical models which have been developed for eukaryotic MTs might explain dynamics of bMTs as well. Using cryo-ET we showed that bMTs have simpler structures with four protofilaments and less curved plus ends. We also observed that bMTs can form bacterial microtubule doublets inside bundles. In comparison with microtubule doublets we concluded that the lack of long acidic C-terminal tails in bTubA and bTubB is a possible explanation for the formation of bundles and bMTDs.

Due to the high depolymerization rate of bMTs, it was impossible to image these filaments in a shrinking state with a cryo-ET setup in a buffer condition similar to growing bMTs (in the buffer containing PIPES (see Materials and Methods section of Chapter 3)). However, using a high PEG concentration (5%) in 50 mM HEPES-KOH pH 7.7 for dilution before freezing the sample, inhibited the fast shrinkage in a way that cryo-ET imaging was achievable. Plus end analysis then revealed no significant difference in the curvature of the protofilaments in shrinking compared to that of growing protofilaments (Figure 6.1B). It is known however that the flared ends of shrinking eukaryotic microtubules are significantly longer than that of growing MTs (Figure 6.1B).

6

The aim of Chapter 4 was to examine the recruitment of bacterial cytoskeletal systems in a system for synthetic cells with the final goal of DNA segregation. The investigation of two filament-based systems showed that neither of the two are suitable for building a DNA segregation system for a synthetic cell. As a result, we assessed a combination of the two systems. Our experiments confirmed that the design which includes an optogenetic tool might be a good candidate for DNA segregation as various parts of the system are expressible in PURE buffer, the system is observed to be encapsulated in GUVs, and the optogenetic tool provides an external functional control.

On our design for the synthetic DNA segregation, several questions however still remain to be answered. A logical next step of this work is to investigate the interaction between the bTubC-iLID and SspB-TubR complexes in the presence of blue light. Next, the activity of the optogenetic tools should be assessed with the expressed proteins in the PURE system. To do so, the iLID and SspB proteins should be expressed from the corresponding genes and their interaction should be examined in the presence of blue light for instance by the means of an iSCAT (interferometric scattering microscopy) setup. Although no filaments formed from expressed TubZ in PURE, one way which could be employed to increase the chance of correct folding of a globular protein is to express it at a lower temperature (*e.g.* 20°C) for longer time (*e.g.* 5 h). The external control could then be implemented to the TubR by placing a LOV domain in a way that deactivates the protein upon light illumination. We have already designed this protein and it is ready to be tested.

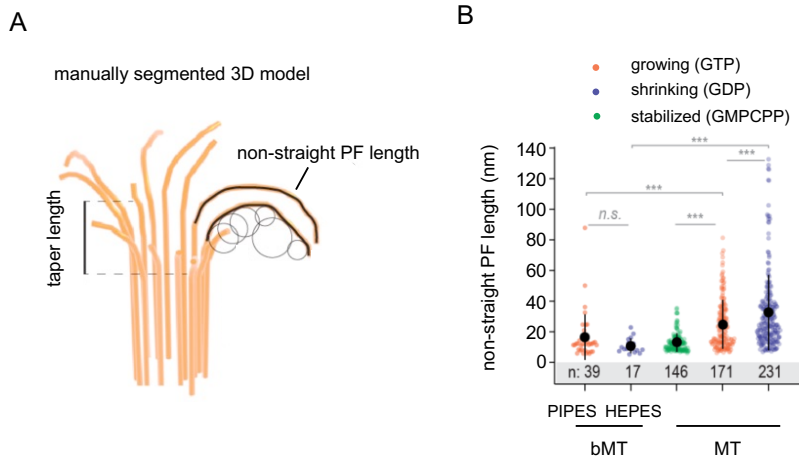


Figure 6.1: Non-straight protofilament (PF) length of plus end of bMTs and MTs in different nucleotide states: (A) A schematic 3D model of a MT end. The flared end length is the length of a protofilament which is not straight from the point the curvature starts. Image from [126]. (B) A comparison between flared end length of growing and shrinking bMTs and GMPCPP-, growing and shrinking MTs. Although there is a significant difference between flared end length of different nucleotide states of MTs, no significant difference was observed between the two states of bMTs, given that the buffer condition of the two samples was not similar. Cryo-ET experiments and image analysis of shrinking bMTs (HEPES) were performed in a collaboration with Tomohiro Shima, Vladimir Volkov, and Hanjin Liu.

Following a slightly different approach, we also designed a light-inducible ParMRC system by splitting ParR into a filament binding domain (ParR^C) and a DNA binding domain (ParR^N) and fused the photoreceptors to each of these distinct domains of ParR forming proteins we call ParR^N-iLID and SspB-ParR^C (Figure 6.2A). In this design, both parts of the photo-inducible adapter protein are forced to make dimers by a leucine zipper. A linker in each fragment is implemented to reduce the steric hindrance of these bulky proteins while squeezing into the ParR^C helix. Preliminary results showed two promising aspects of this system. First, the *in vitro* assays with AMPPNP-ParM formed asters of ParM-SspB-ParR^C similar to those we observed with wild type ParR (Figure 6.2B). Second, the EMSA results showed a shift in the parC height on a 6% polyacrylamide gel with ParR^N-iLID (Figure 6.2C). Despite these promising results, further work is required to establish the viability of the application of this system in synthetic cells.

In Chapter 5 we evaluated the PhuZ filaments' interaction with barriers. The most relevant finding to emerge from this study is that stalling forces exerted to a PhuZ filaments due to interaction with a rigid obstacle enhance filament catastrophes. In addition, we showed that PhuZ filament minus end growth has a higher critical concentration compared to its plus end and was observed at high PhuZ concentrations. Taken together, these results suggest that at later stages of infection, high PhuZ concentration might

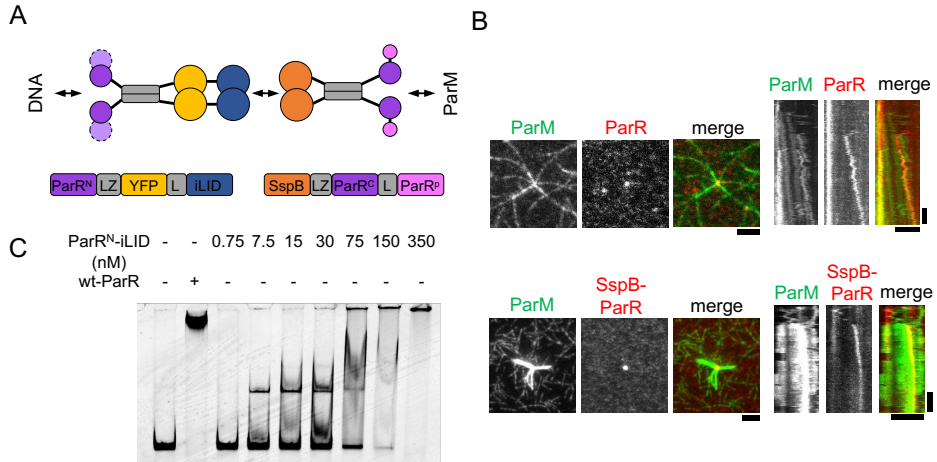


Figure 6.2: ParMRC opto-controllable system: (A) Schematic depiction of light-inducible ParMRC system. Different domains of ParR are fused to the iLID-SspB system which is supposed to induce the ParM-parC recruitment upon blue light illumination. (B) (top) A TIRF image of a ParM (green) aster formed around a wt-ParR (red) oligomer and a kymograph of the pushing event which happens while two asters approach each other. (bottom) A TIRF image of a ParM (green) aster formed with a SspB-ParR^C (red) oligomer in the center and a kymograph which shows a separation when two asters approach each other. (C) A polyacrylamide gel of an EMSA which was performed to examine the effect of ParR^N-iLID on tubC. Atto647-tubC is mixed with 75 nM wt-TubR and various concentration of ParR^N-iLID as indicated, incubated for 30 min at room temperature and ran on the gel. Scale bars: horizontal = 5 μ m, vertical = 30 s. The optogenetic system was designed and purified by Eli van der Sluis and the experiments were performed by Koen van Gent.

lead to treadmilling in a way that results in capsid transportation towards the cell center.

Our results revealed additional details about the PhuZ behavior in a filamentous form, however, several questions still remain to be answered. The precise mechanism of a phage spindle needs more information on PhuZ adapter proteins. PhuZ adapter proteins could be investigated by searching through the bioinformatics of the phage genome and by co-sedimentation assays. We have carried out bioinformatics-based research to find adapter proteins by comparing the loci close to *phuZ* of 201- ϕ 2-1 which revealed an interesting candidate closely related to gelsolin which is an actin binding protein. However, further analysis showed that the filament binding domain on the phage gelsolin is absent. All in all, preliminary results revealed no significant sequence similarity between PhuZ or shell protein's neighboring genes and all known MT associated proteins, TubR, bTubC, and ParR from various species.

7

BIBLIOGRAPHY

- [1] David W. Adams and Jeff Errington. Bacterial cell division: assembly, maintenance and disassembly of the z ring. *Nature Reviews Microbiology*, 7(9):642–653, 2009. URL <https://doi.org/10.1038/nrmicro2198>.
- [2] O. Adir, M. R. Albalak, R. Abel, L. E. Weiss, G. Chen, A. Gruber, O. Staufer, Y. Kurman, I. Kaminer, J. Shklover, J. Shainsky-Roitman, I. Platzman, L. Gepstein, Y. Shechtman, B. A. Horwitz, and A. Schroeder. Synthetic cells with self-activating optogenetic proteins communicate with natural cells. *Nat Commun*, 13(1):2328, 2022. URL <https://doi.org/10.1038/s41467-022-29871-8>.
- [3] L. Akendengue, S. Trepout, M. Grana, A. Voegelé, C. Janke, B. Raynal, A. Chenal, S. Marco, and A. M. Wehenkel. Bacterial kinesin light chain (bklc) links the btub cytoskeleton to membranes. *Sci Rep*, 7:45668, 2017. ISSN 2045-2322 (Electronic) 2045-2322 (Linking). URL <https://doi.org/10.1038/srep45668>.
- [4] A. Akhmanova and M. O. Steinmetz. Tracking the ends: a dynamic protein network controls the fate of microtubule tips. *Nat Rev Mol Cell Biol*, 9(4): 309–22, 2008. ISSN 1471-0080 (Electronic) 1471-0072 (Linking). URL <https://doi.org/10.1038/nrm2369>.
- [5] Jun F. Allard and Eric N. Cytrynbaum. Force generation by a dynamic z-ring in *Escherichia coli* cell division. *Proceedings of the National Academy of Sciences*, 106(1):145–150, 2009. URL <https://doi.org/10.1073/pnas.0808657106>.
- [6] T. Antal, P. L. Krapivsky, S. Redner, M. Mailman, and B. Chakraborty. Dynamics of an idealized model of microtubule growth and catastrophe. *Phys Rev E Stat Nonlin Soft Matter Phys*, 76(4 Pt 1):041907, 2007. URL <https://doi.org/10.1103/PhysRevE.76.041907>.

- [7] C. H. Aylett and J. Lowe. Superstructure of the centromeric complex of tubzrc plasmid partitioning systems. *Proc Natl Acad Sci U S A*, 109(41):16522–7, 2012. ISSN 1091-6490 (Electronic) 0027-8424 (Linking). URL <https://doi.org/10.1073/pnas.1210899109>.
- [8] Lucia Baldauf, Lennard van Buren, Federico Fanalista, and Gijse Hendrika Koenderink. Actomyosin-driven division of a synthetic cell. *ACS Synthetic Biology*, 11(10):3120–3133, 2022. URL <https://doi.org/10.1021/acssynbio.2c00287>.
- [9] D. Barilla. One-way ticket to the cell pole: plasmid transport by the prokaryotic tubulin homolog tubz. *Proc Natl Acad Sci U S A*, 107(27):12061–2, 2010. ISSN 1091-6490 (Electronic) 0027-8424 (Linking). URL <https://doi.org/10.1073/pnas.1007331107>.
- [10] Eric Becker, Nick C Herrera, Felizza Q Gunderson, Alan I Derman, Amber L Dance, Jennifer Sims, Rachel A Larsen, and Joe Pogliano. Dna segregation by the bacterial actin alfa during bacillus subtilis growth and development. *The EMBO Journal*, 25(24):5919–5931, 2006. URL <https://doi.org/10.1038/sj.emboj.7601443>.
- [11] D. Blanken, D. Foschepoth, A. C. Serrao, and C. Danelon. Genetically controlled membrane synthesis in liposomes. *Nat Commun*, 11(1):4317, 2020. URL <https://doi.org/10.1038/s41467-020-17863-5>.
- [12] H. Bowne-Anderson, M. Zanic, M. Kauer, and J. Howard. Microtubule dynamic instability: a new model with coupled gtp hydrolysis and multistep catastrophe. *Bioessays*, 35(5):452–61, 2013. ISSN 1521-1878 (Electronic) 0265-9247 (Linking). URL <https://doi.org/10.1002/bies.201200131>.
- [13] C. P. Brangwynne, F. C. MacKintosh, S. Kumar, N. A. Geisse, J. Talbot, L. Mahadevan, K. K. Parker, D. E. Ingber, and D. A. Weitz. Microtubules can bear enhanced compressive loads in living cells because of lateral reinforcement. *J Cell Biol*, 173(5):733–41, 2006. URL <https://doi.org/10.1083/jcb.200601060>.
- [14] G. J. Brouhard, J. H. Stear, T. L. Noetzel, J. Al-Bassam, K. Kinoshita, S. C. Harrison, J. Howard, and A. A. Hyman. Xmap215 is a processive microtubule polymerase. *Cell*, 132(1):79–88, 2008. ISSN 0092-8674 (Print) 0092-8674 (Linking). URL <https://doi.org/10.1016/j.cell.2007.11.043>.
- [15] L. Brun, B. Rupp, J. J. Ward, and F. Nedelec. A theory of microtubule catastrophes and their regulation. *Proc Natl Acad Sci U S A*, 106(50):21173–8, 2009. URL <https://doi.org/10.1073/pnas.0910774106>.
- [16] T. O. Buchholz, A. Krull, R. Shahidi, G. Pigino, G. Jekely, and F. Jug. Content-aware image restoration for electron microscopy. *Methods Cell Biol*, 152:277–289, 2019. URL <https://doi.org/10.1016/bs.mcb.2019.05.001>.

-
- [17] Matthew T. Cabeen and Christine Jacobs-Wagner. The bacterial cytoskeleton. *Annual Review of Genetics*, 44(1):365–392, 2010. URL <https://doi.org/10.1146/annurev-genet-102108-134845>.
- [18] L. Cassimeris, N. K. Pryer, and E. D. Salmon. Real-time observations of microtubule dynamic instability in living cells. *J Cell Biol*, 107(6 Pt 1):2223–31, 1988. ISSN 0021-9525 (Print) 0021-9525 (Linking). URL <https://doi.org/10.1083/jcb.107.6.2223>.
- [19] D. Castano-Diez, M. Kudryashev, M. Arheit, and H. Stahlberg. Dynamo: a flexible, user-friendly development tool for subtomogram averaging of cryo-em data in high-performance computing environments. *J Struct Biol*, 178(2):139–51, 2012. URL <https://doi.org/10.1016/j.jsb.2011.12.017>.
- [20] M. Castoldi and A. V. Popov. Purification of brain tubulin through two cycles of polymerization-depolymerization in a high-molarity buffer. *Protein Expr Purif*, 32(1):83–8, 2003. URL [https://doi.org/10.1016/S1046-5928\(03\)00218-3](https://doi.org/10.1016/S1046-5928(03)00218-3).
- [21] V. Chaikerasak, K. Nguyen, M. E. Egan, M. L. Erb, A. Vavilina, and J. Pogliano. The phage nucleus and tubulin spindle are conserved among large pseudomonas phages. *Cell Rep*, 20(7):1563–1571, 2017. ISSN 2211-1247 (Electronic). URL <https://doi.org/10.1016/j.celrep.2017.07.064>.
- [22] V. Chaikerasak, K. Nguyen, K. Khanna, A. F. Brilot, M. L. Erb, J. K. Coker, A. Vavilina, G. L. Newton, R. Buschauer, K. Pogliano, E. Villa, D. A. Agard, and J. Pogliano. Assembly of a nucleus-like structure during viral replication in bacteria. *Science*, 355(6321):194–197, 2017. ISSN 1095-9203 (Electronic) 0036-8075 (Linking). URL <https://doi.org/10.1126/science.aal2130>.
- [23] V. Chaikerasak, K. Khanna, K. T. Nguyen, J. Sugie, M. E. Egan, M. L. Erb, A. Vavilina, P. Nonejuie, E. Nieweglowska, K. Pogliano, D. A. Agard, E. Villa, and J. Pogliano. Viral capsid trafficking along treadmilling tubulin filaments in bacteria. *Cell*, 177(7):1771–1780 e12, 2019. ISSN 1097-4172 (Electronic) 0092-8674 (Linking). URL <https://doi.org/10.1016/j.cell.2019.05.032>.
- [24] V. Chaikerasak, E. A. Birkholz, and J. Pogliano. The phage nucleus and phuz spindle: Defining features of the subcellular organization and speciation of nucleus-forming jumbo phages. *Front Microbiol*, 12:641317, 2021. ISSN 1664-302X (Print) 1664-302X (Linking). URL <https://doi.org/10.3389/fmicb.2021.641317>.
- [25] T. Chakraborty and S. V. Wegner. Cell to cell signaling through light in artificial cell communities: Glowing predator lures prey. *ACS Nano*, 15(6):9434–9444, 2021. ISSN 1936-086X (Electronic) 1936-0851 (Linking). URL <https://doi.org/10.1021/acsnano.1c01600>.
- [26] Y. Chen and H. P. Erickson. In vitro assembly studies of ftsz/tubulin-like proteins (tubz) from bacillus plasmids: evidence for a capping mechanism. *J Biol Chem*,

- 283(13):8102–9, 2008. ISSN 0021-9258 (Print) 0021-9258 (Linking). URL <https://doi.org/10.1074/jbc.M709163200>.
- [27] D. Chretien, J. M. Kenney, S. D. Fuller, and R. H. Wade. Determination of microtubule polarity by cryo-electron microscopy. *Structure*, 4(9):1031–40, 1996. URL [https://doi.org/10.1016/s0969-2126\(96\)00110-4](https://doi.org/10.1016/s0969-2126(96)00110-4).
- [28] S. Cohen, S. Au, and N. Pante. How viruses access the nucleus. *Biochim Biophys Acta*, 1813(9):1634–45, 2011. ISSN 0006-3002 (Print) 0006-3002 (Linking). URL <https://doi.org/10.1016/j.bbamcr.2010.12.009>.
- [29] C. E. Coombes, A. Yamamoto, M. R. Kenzie, D. J. Odde, and M. K. Gardner. Evolving tip structures can explain age-dependent microtubule catastrophe. *Curr Biol*, 23(14):1342–8, 2013. URL <https://doi.org/10.1016/j.cub.2013.05.059>.
- [30] Richard A. Daniel and Jeff Errington. Control of cell morphogenesis in bacteria: Two distinct ways to make a rod-shaped cell. *Cell*, 113(6):767–776, 2003. URL [https://doi.org/10.1016/S0092-8674\(03\)00421-5](https://doi.org/10.1016/S0092-8674(03)00421-5).
- [31] X. Deng, G. Fink, T. A. M. Bharat, S. He, D. Kureisaite-Ciziene, and J. Lowe. Four-stranded mini microtubules formed by prosthecobacter btubab show dynamic instability. *Proc Natl Acad Sci U S A*, 114(29):E5950–E5958, 2017. ISSN 1091-6490 (Electronic) 0027-8424 (Linking). URL <https://doi.org/10.1073/pnas.1705062114>.
- [32] S. Deshpande and C. Dekker. Synthetic life on a chip. *Emerg Top Life Sci*, 3(5): 559–566, 2019. URL <https://doi.org/10.1042/ETLS20190097>.
- [33] C. Diaz-Celis, V. I. Risca, F. Hurtado, J. K. Polka, S. D. Hansen, D. Maturana, R. Lagos, R. D. Mullins, and O. Monasterio. Bacterial tubulins a and b exhibit polarized growth, mixed-polarity bundling, and destabilization by gtp hydrolysis. *J Bacteriol*, 199(19), 2017. ISSN 1098-5530 (Electronic) 0021-9193 (Linking). URL <https://doi.org/10.1128/JB.00211-17>.
- [34] M. Dogterom and B. Yurke. Measurement of the force-velocity relation for growing microtubules. *Science*, 278(5339):856–60, 1997. URL <https://doi.org/10.1126/science.278.5339.856>.
- [35] M. Dogterom, J. W. Kerssemakers, G. Romet-Lemonne, and M. E. Janson. Force generation by dynamic microtubules. *Curr Opin Cell Biol*, 17(1):67–74, 2005. ISSN 0955-0674 (Print) 0955-0674 (Linking). URL <https://doi.org/10.1016/j.ceb.2004.12.011>.
- [36] K. Dohner, A. Wolfstein, U. Prank, C. Echeverri, D. Dujardin, R. Vallee, and B. Sodeik. Function of dynein and dynactin in herpes simplex virus capsid transport. *Mol Biol Cell*, 13(8):2795–809, 2002. URL <https://doi.org/10.1091/mbc.01-07-0348>.

-
- [37] O. Draper, M. E. Byrne, Z. Li, S. Keyhani, J. C. Barrozo, G. Jensen, and A. Komeili. Mamk, a bacterial actin, forms dynamic filaments in vivo that are regulated by the acidic proteins mamj and limj. *Mol Microbiol*, 82(2):342–54, 2011. URL <https://doi.org/10.1111/j.1365-2958.2011.07815.x>.
- [38] C. Duellberg, N. I. Cade, D. Holmes, and T. Surrey. The size of the eb cap determines instantaneous microtubule stability. *Elife*, 5, 2016. ISSN 2050-084X (Electronic) 2050-084X (Linking). URL <https://doi.org/10.7554/eLife.13470>.
- [39] Sophie Dumont and Timothy J. Mitchison. Force and length in the mitotic spindle. *Current Biology*, 19(17):R749–R761, 2009. URL <https://doi.org/10.1016/j.cub.2009.07.028>.
- [40] V. Emsellem, O. Cardoso, and P. Tabeling. Vesicle deformation by microtubules: A phase diagram. *Physical Review E*, 58(4):4807–4810, 1998. ISSN 1063-651x. URL <https://doi.org/DOI10.1103/PhysRevE.58.4807>.
- [41] M. L. Erb, J. A. Kraemer, J. K. Coker, V. Chaikerasitak, P. Nonejuie, D. A. Agard, and J. Pogliano. A bacteriophage tubulin harnesses dynamic instability to center dna in infected cells. *Elife*, 3, 2014. ISSN 2050-084X (Electronic) 2050-084X (Linking). URL <https://doi.org/10.7554/eLife.03197>.
- [42] P. Fanara, B. Oback, K. Ashman, A. Podtelejnikov, and R. Brandt. Identification of minus, a small polypeptide that functions as a microtubule nucleation suppressor. *EMBO J*, 18(3):565–77, 1999. ISSN 0261-4189 (Print) 0261-4189 (Linking). URL <https://doi.org/10.1093/emboj/18.3.565>.
- [43] G. Fink and J. Lowe. Reconstitution of a prokaryotic minus end-tracking system using tubrc centromeric complexes and tubulin-like protein tubz filaments. *Proc Natl Acad Sci U S A*, 112(15):E1845–50, 2015. ISSN 1091-6490 (Electronic) 0027-8424 (Linking). URL <https://doi.org/10.1073/pnas.1423746112>.
- [44] H. Flyvbjerg, T. E. Holy, and S. Leibler. Microtubule dynamics: Caps, catastrophes, and coupled hydrolysis. *Phys Rev E Stat Phys Plasmas Fluids Relat Interdiscip Topics*, 54(5):5538–5560, 1996. URL <https://doi.org/10.1103/physreve.54.5538>.
- [45] Matthew J. Footer, Jacob W. J. Kerssemakers, Julie A. Theriot, and Marileen Dogterom. Direct measurement of force generation by actin filament polymerization using an optical trap. *Proceedings of the National Academy of Sciences*, 104(7):2181–2186, 2007. URL <https://doi.org/10.1073/pnas.0607052104>.
- [46] A. Fragasso, N. De Franceschi, P. Stommer, E. O. van der Sluis, H. Dietz, and C. Dekker. Reconstitution of ultrawide dna origami pores in liposomes for transmembrane transport of macromolecules. *ACS Nano*, 15(8):12768–12779, 2021. URL <https://doi.org/10.1021/acsnano.1c01669>.
- [47] M. K. Gardner, B. D. Charlebois, I. M. Janosi, J. Howard, A. J. Hunt, and D. J. Odde. Rapid microtubule self-assembly kinetics. *Cell*, 146(4):582–92, 2011. ISSN

- 1097-4172 (Electronic) 0092-8674 (Linking). URL <https://doi.org/10.1016/j.cell.2011.06.053>.
- [48] M. K. Gardner, M. Zanic, C. Gell, V. Bormuth, and J. Howard. Depolymerizing kinesins kip3 and mcak shape cellular microtubule architecture by differential control of catastrophe. *Cell*, 147(5):1092–103, 2011. ISSN 1097-4172 (Electronic) 0092-8674 (Linking). URL <https://doi.org/10.1016/j.cell.2011.10.037>.
- [49] E. C. Garner, C. S. Campbell, and R. D. Mullins. Dynamic instability in a dna-segregating prokaryotic actin homolog. *Science*, 306(5698):1021–5, 2004. URL <https://doi.org/10.1126/science.1101313>.
- [50] N. J. Gaut and K. P. Adamala. Reconstituting natural cell elements in synthetic cells. *Adv Biol (Weinh)*, 5(3):e2000188, 2021. URL <https://doi.org/10.1002/adbi.202000188>.
- [51] E. Godino, J. N. Lopez, D. Foschepoth, C. Cleij, A. Doerr, C. F. Castella, and C. Danelon. De novo synthesized min proteins drive oscillatory liposome deformation and regulate ftsa-ftsZ cytoskeletal patterns. *Nat Commun*, 10(1):4969, 2019. URL <https://doi.org/10.1038/s41467-019-12932-w>.
- [52] S. C. Goetz and K. V. Anderson. The primary cilium: a signalling centre during vertebrate development. *Nat Rev Genet*, 11(5):331–44, 2010. URL <https://doi.org/10.1038/nrg2774>.
- [53] C. Gogou, A. Japaridze, and C. Dekker. Mechanisms for chromosome segregation in bacteria. *Front Microbiol*, 12:685687, 2021. URL <https://doi.org/10.3389/fmicb.2021.685687>.
- [54] E. L. Grishchuk, M. I. Molodtsov, F. I. Ataulkhanov, and J. R. McIntosh. Force production by disassembling microtubules. *Nature*, 438(7066):384–8, 2005. URL <https://doi.org/10.1038/nature04132>.
- [55] J. Guan and J. Bondy-Denomy. Intracellular organization by jumbo bacteriophages. *J Bacteriol*, 203(2), 2020. URL <https://doi.org/10.1128/JB.00362-20>.
- [56] J. Guan, A. Oromi-Bosch, S. D. Mendoza, S. Karambelkar, J. D. Berry, and J. Bondy-Denomy. Bacteriophage genome engineering with crispr-cas13a. *Nat Microbiol*, 7(12):1956–1966, 2022. URL <https://doi.org/10.1038/s41564-022-01243-4>.
- [57] N. B. Gudimchuk and J. R. McIntosh. Regulation of microtubule dynamics, mechanics and function through the growing tip. *Nat Rev Mol Cell Biol*, 22(12):777–795, 2021. ISSN 1471-0080 (Electronic) 1471-0072 (Linking). URL <https://doi.org/10.1038/s41580-021-00399-x>.

-
- [58] N. B. Gudimchuk, E. V. Ulyanov, E. O'Toole, C. L. Page, D. S. Vinogradov, G. Morgan, G. Li, J. K. Moore, E. Szczesna, A. Roll-Mecak, F. I. Ataullakhanov, and J. Richard McIntosh. Mechanisms of microtubule dynamics and force generation examined with computational modeling and electron cryotomography. *Nat Commun*, 11(1), 2020. URL <https://doi.org/10.1038/s41467-020-17553-2>.
- [59] G. Guntas, R. A. Hallett, S. P. Zimmerman, T. Williams, H. Yumerefendi, J. E. Bear, and B. Kuhlman. Engineering an improved light-induced dimer (ilid) for controlling the localization and activity of signaling proteins. *Proc Natl Acad Sci U S A*, 112(1):112–7, 2015. ISSN 1091-6490 (Electronic) 0027-8424 (Linking). URL <https://doi.org/10.1073/pnas.1417910112>.
- [60] Gil Henkin, Wei-Xiang Chew, François Nédélec, and Thomas Surrey. Crosslinker design determines microtubule network organization by opposing motors. *bioRxiv*, page 2022.04.22.488007, 2022. URL <https://doi.org/10.1101/2022.04.22.488007>.
- [61] L. Hu, A. G. Vecchiarelli, K. Mizuuchi, K. C. Neuman, and J. Liu. Brownian ratchet mechanisms of para-mediated partitioning. *Plasmid*, 92:12–16, 2017. URL <https://doi.org/10.1016/j.plasmid.2017.05.002>.
- [62] P. J. Huis In 't Veld, V. A. Volkov, I. D. Stender, A. Musacchio, and M. Dogterom. Molecular determinants of the ska-ndc80 interaction and their influence on microtubule tracking and force-coupling. *Elife*, 8, 2019. ISSN 2050-084X (Electronic) 2050-084X (Linking). URL <https://doi.org/10.7554/eLife.49539>.
- [63] D. Hurtgen, S. M. Murray, J. Mascarenhas, and V. Sourjik. Dna segregation in natural and synthetic minimal systems. *Adv Biosyst*, 3(6):e1800316, 2019. URL <https://doi.org/10.1002/adbi.201800316>.
- [64] Linda A. Amos Jan Löwe. *Prokaryotic Cytoskeletons: Filamentous Protein Polymers Active in the Cytoplasm of Bacterial and Archaeal Cells*. Springer Cham, 2017. URL <https://doi.org/10.1007/978-3-319-53047-5>.
- [65] M. E. Janson and M. Dogterom. Scaling of microtubule force-velocity curves obtained at different tubulin concentrations. *Phys Rev Lett*, 92(24):248101, 2004. URL <https://doi.org/10.1103/PhysRevLett.92.248101>.
- [66] M. E. Janson, M. E. de Dood, and M. Dogterom. Dynamic instability of microtubules is regulated by force. *J Cell Biol*, 161(6):1029–34, 2003. URL <https://doi.org/10.1083/jcb.200301147>.
- [67] Premkumar Jayaraman, Jing Wui Yeoh, Sudhaghar Jayaraman, Ai Ying Teh, Jingyun Zhang, and Chueh Loo Poh. Cell-free optogenetic gene expression system. *ACS Synthetic Biology*, 7(4):986–994, 2018. URL <https://doi.org/10.1021/acssynbio.7b00422>.

- [68] C. Jenkins, R. Samudrala, I. Anderson, B. P. Hedlund, G. Petroni, N. Michailova, N. Pinel, R. Overbeek, G. Rosati, and J. T. Staley. Genes for the cytoskeletal protein tubulin in the bacterial genus *prostheco*bacter. *Proc Natl Acad Sci U S A*, 99(26):17049–54, 2002. URL <https://doi.org/10.1073/pnas.012516899>.
- [69] J. Kattan, A. Doerr, M. Dogterom, and C. Danelon. Shaping liposomes by cell-free expressed bacterial microtubules. *ACS Synth Biol*, 10(10):2447–2455, 2021. ISSN 2161-5063 (Electronic) 2161-5063 (Linking). URL <https://doi.org/10.1021/acssynbio.1c00278>.
- [70] Johannes Kattan. *Biosynthesis of protein filaments for the creation of a minimal cell*. PhD thesis, Delft University of Technology, May 2020. URL <https://doi.org/10.4233/uuid:724f70a9-efd9-4598-9a24-064aa77db509>.
- [71] J. S. Khamo, V. V. Krishnamurthy, S. R. Sharum, P. Mondal, and K. Zhang. Applications of optobiology in intact cells and multicellular organisms. *J Mol Biol*, 429(20):2999–3017, 2017. ISSN 1089-8638 (Electronic) 0022-2836 (Linking). URL <https://doi.org/10.1016/j.jmb.2017.08.015>.
- [72] S. Kohyama, A. Merino-Salomon, and P. Schwille. In vitro assembly, positioning and contraction of a division ring in minimal cells. *Nat Commun*, 13(1):6098, 2022. URL <https://doi.org/10.1038/s41467-022-33679-x>.
- [73] Maurits Kok. *The dynamics of microtubule stability: A reconstitution of regulated microtubule assembly under force*. PhD thesis, Delft University of Technology, April 2019. URL <https://doi.org/10.4233/uuid:5cb3dd60-78ab-4272-a820-7a754c2cc6a0>.
- [74] Maurits Kok, Florian Huber, Svenja-Marei Kalisch, and Marileen Dogterom. Eb3-informed dynamics of the microtubule stabilizing cap during stalled growth. *bioRxiv*, page 2021.12.07.471417, 2021. URL <https://doi.org/10.1101/2021.12.07.471417>.
- [75] K. Kolar, C. Knobloch, H. Stork, M. Znidaric, and W. Weber. Optobase: A web platform for molecular optogenetics. *ACS Synth Biol*, 7(7):1825–1828, 2018. URL <https://doi.org/10.1021/acssynbio.8b00120>.
- [76] D. E. Koshland, T. J. Mitchison, and M. W. Kirschner. Polewards chromosome movement driven by microtubule depolymerization in vitro. *Nature*, 331(6156):499–504, 1988. ISSN 0028-0836 (Print) 0028-0836 (Linking). URL <https://doi.org/10.1038/331499a0>.
- [77] J. A. Kraemer, M. L. Erb, C. A. Waddling, E. A. Montabana, E. A. Zehr, H. Wang, K. Nguyen, D. S. Pham, D. A. Agard, and J. Pogliano. A phage tubulin assembles dynamic filaments by an atypical mechanism to center viral dna within the host cell. *Cell*, 149(7):1488–99, 2012. ISSN 1097-4172 (Electronic) 0092-8674 (Linking). URL <https://doi.org/10.1016/j.cell.2012.04.034>.

-
- [78] J. R. Kremer, D. N. Mastrorarde, and J. R. McIntosh. Computer visualization of three-dimensional image data using imod. *J Struct Biol*, 116(1):71–6, 1996. ISSN 1047-8477 (Print) 1047-8477 (Linking). URL <https://doi.org/10.1006/jสบi.1996.0013>.
- [79] M. Kurokawa, S. Seno, H. Matsuda, and B. W. Ying. Correlation between genome reduction and bacterial growth. *DNA Res*, 23(6), 2016. URL <https://doi.org/10.1093/dnares/dsw035>.
- [80] L. Laan, J. Husson, E. L. Munteanu, J. W. Kerssemakers, and M. Dogterom. Force-generation and dynamic instability of microtubule bundles. *Proc Natl Acad Sci U S A*, 105(26):8920–5, 2008. URL <https://doi.org/10.1073/pnas.0710311105>.
- [81] L. D. Landau, E. M. Lifshitz, A. M. Kosevich, and L. P. Pitaevskii. *Theory of elasticity*. Course of theoretical physics. Pergamon Press, Oxford Oxfordshire ; New York, 3rd english edition, 1986. ISBN 0080339174 0080339166 (soft).
- [82] R. A. Larsen, C. Cusumano, A. Fujioka, G. Lim-Fong, P. Patterson, and J. Pogliano. Treadmilling of a prokaryotic tubulin-like protein, tubz, required for plasmid stability in bacillus thuringiensis. *Genes Dev*, 21(11):1340–52, 2007. ISSN 0890-9369 (Print) 0890-9369 (Linking). URL <https://doi.org/10.1101/gad.1546107>.
- [83] Thomas G. Laughlin, Amar Deep, Amy M. Prichard, Christian Seitz, Yajie Gu, Eray Enustun, Sergey Suslov, Kanika Khanna, Erica A. Birkholz, Emily Armbruster, J. Andrew McCammon, Rommie E. Amaro, Joe Pogliano, Kevin D. Corbett, and Elizabeth Villa. Architecture and self-assembly of the jumbo bacteriophage nuclear shell. *Nature*, 608(7922):429–435, 2022. URL <https://doi.org/10.1038/s41586-022-05013-4>.
- [84] A. A. Levesque, L. Howard, M. B. Gordon, and D. A. Compton. A functional relationship between numa and kid is involved in both spindle organization and chromosome alignment in vertebrate cells. *Mol Biol Cell*, 14(9):3541–52, 2003. URL <https://doi.org/10.1091/mbc.e03-02-0082>.
- [85] Y. Li, A. Dabrazhynetskaya, B. Youngren, and S. Austin. The role of par proteins in the active segregation of the p1 plasmid. *Mol Microbiol*, 53(1):93–102, 2004. URL <https://doi.org/10.1111/j.1365-2958.2004.04111.x>.
- [86] Renu Maan, Louis Reese, Vladimir A. Volkov, Matthew R. King, Eli O. van der Sluis, Nemo Andrea, Wiel H. Evers, Arjen J. Jakobi, and Marileen Dogterom. Multivalent interactions facilitate motor-dependent protein accumulation at growing microtubule plus-ends. *Nature Cell Biology*, 2022. URL <https://doi.org/10.1038/s41556-022-01037-0>.
- [87] A. J. Martin-Galiano, M. A. Oliva, L. Sanz, A. Bhattacharyya, M. Serna, H. Yebenes, J. M. Valpuesta, and J. M. Andreu. Bacterial tubulin distinct loop

- sequences and primitive assembly properties support its origin from a eukaryotic tubulin ancestor. *J Biol Chem*, 286(22):19789–803, 2011. URL <https://doi.org/10.1074/jbc.M111.230094>.
- [88] B. Martin-Garcia, A. Martin-Gonzalez, C. Carrasco, A. M. Hernandez-Arriaga, R. Ruiz-Quero, R. Diaz-Orejas, C. Aicart-Ramos, F. Moreno-Herrero, and M. A. Oliva. The tubr-centromere complex adopts a double-ring segrosome structure in type iii partition systems. *Nucleic Acids Res*, 46(11):5704–5716, 2018. ISSN 1362-4962 (Electronic) 0305-1048 (Linking). URL <https://doi.org/10.1093/nar/gky370>.
- [89] D. N. Mastronarde. Automated electron microscope tomography using robust prediction of specimen movements. *J Struct Biol*, 152(1):36–51, 2005. ISSN 1047-8477 (Print) 1047-8477 (Linking). URL <https://doi.org/10.1016/j.jsb.2005.07.007>.
- [90] A. C. McCue and B. Kuhlman. Design and engineering of light-sensitive protein switches. *Curr Opin Struct Biol*, 74:102377, 2022. ISSN 1879-033X (Electronic) 0959-440X (Linking). URL <https://doi.org/10.1016/j.sbi.2022.102377>.
- [91] J. R. McIntosh. Mitosis. *Cold Spring Harb Perspect Biol*, 8(9), 2016. URL <https://doi.org/10.1101/cshperspect.a023218>.
- [92] J. R. McIntosh, E. O’Toole, G. Morgan, J. Austin, E. Ulyanov, F. Ataullakhanov, and N. Gudimchuk. Microtubules grow by the addition of bent guanosine triphosphate tubulin to the tips of curved protofilaments. *J Cell Biol*, 217(8):2691–2708, 2018. URL <https://doi.org/10.1083/jcb.201802138>.
- [93] Joyce C. M. Meiring, Ilya Grigoriev, Wilco Nijenhuis, Lukas C. Kapitein, and Anna Akhmanova. Opto-katanin, an optogenetic tool for localized, microtubule disassembly. *Current Biology*, 32(21):4660–4674.e6, 2022. URL <https://doi.org/https://doi.org/10.1016/j.cub.2022.09.010>.
- [94] S. D. Mendoza, E. S. Nieweglowska, S. Govindarajan, L. M. Leon, J. D. Berry, A. Tiwari, V. Chaikerasitak, J. Pogliano, D. A. Agard, and J. Bondy-Denomy. A bacteriophage nucleus-like compartment shields dna from crispr nucleases. *Nature*, 577(7789):244–248, 2020. ISSN 1476-4687 (Electronic) 0028-0836 (Linking). URL <https://doi.org/10.1038/s41586-019-1786-y>.
- [95] T. Mitchison and M. Kirschner. Dynamic instability of microtubule growth. *Nature*, 312(5991):237–42, 1984. URL <https://doi.org/10.1038/312237a0>.
- [96] J. Moller-Jensen, J. Borch, M. Dam, R. B. Jensen, P. Roepstorff, and K. Gerdes. Bacterial mitosis: Parm of plasmid r1 moves plasmid dna by an actin-like insertional polymerization mechanism. *Mol Cell*, 12(6):1477–87, 2003. ISSN 1097-2765 (Print) 1097-2765 (Linking). URL [https://doi.org/10.1016/s1097-2765\(03\)00451-9](https://doi.org/10.1016/s1097-2765(03)00451-9).

-
- [97] E. A. Montabana and D. A. Agard. Bacterial tubulin tubz-bt transitions between a two-stranded intermediate and a four-stranded filament upon gtp hydrolysis. *Proc Natl Acad Sci U S A*, 111(9):3407–12, 2014. ISSN 1091-6490 (Electronic) 0027-8424 (Linking). URL <https://doi.org/10.1073/pnas.1318339111>.
- [98] L. Ni, W. Xu, M. Kumaraswami, and M. A. Schumacher. Plasmid protein tubr uses a distinct mode of hth-dna binding and recruits the prokaryotic tubulin homolog tubz to effect dna partition. *Proc Natl Acad Sci U S A*, 107(26):11763–8, 2010. ISSN 0027-8424. URL <https://doi.org/10.1073/pnas.1003817107>.
- [99] A. Nick Maleki, P. J. Huis In 't Veld, A. Akhmanova, M. Dogterom, and V. A. Volkov. Estimation of microtubule-generated forces using a dna origami nanospring. *J Cell Sci*, 136(5), 2023. URL <https://doi.org/10.1242/jcs.260154>.
- [100] W. Nijenhuis, M. M. P. van Grinsven, and L. C. Kapitein. An optimized toolbox for the optogenetic control of intracellular transport. *J Cell Biol*, 219(4), 2020. ISSN 1540-8140 (Electronic) 0021-9525 (Linking). URL <https://doi.org/10.1083/jcb.201907149>.
- [101] E. T. O'Brien, W. A. Voter, and H. P. Erickson. Gtp hydrolysis during microtubule assembly. *Biochemistry*, 26(13):4148–56, 1987. URL <https://doi.org/10.1021/bi00387a061>.
- [102] Funso E. Ogunmolu, Shoeib Moradi, Vladimir A. Volkov, Chris van Hoorn, Jingchao Wu, Nemo Andrea, Shasha Hua, Kai Jiang, Ioannis Vakonakis, Mia Potočnjak, Franz Herzog, Benoît Gigant, Nikita Gudimchuk, Kelly E. Stecker, Marileen Dogterom, Michel O. Steinmetz, and Anna Akhmanova. Microtubule plus-end regulation by centriolar cap proteins. *bioRxiv*, page 2021.12.29.474442, 2022. URL <https://doi.org/10.1101/2021.12.29.474442>.
- [103] R. Ohlendorf and A. Moglich. Light-regulated gene expression in bacteria: Fundamentals, advances, and perspectives. *Front Bioeng Biotechnol*, 10:1029403, 2022. URL <https://doi.org/10.3389/fbioe.2022.1029403>.
- [104] M. A. Oliva, A. J. Martin-Galiano, Y. Sakaguchi, and J. M. Andreu. Tubulin homolog tubz in a phage-encoded partition system. *Proc Natl Acad Sci U S A*, 109(20):7711–6, 2012. ISSN 1091-6490 (Electronic) 0027-8424 (Linking). URL <https://doi.org/10.1073/pnas.1121546109>.
- [105] L. Olivi, M. Berger, R. N. P. Creyghton, N. De Franceschi, C. Dekker, B. M. Mulder, N. J. Claassens, P. R. Ten Wolde, and J. van der Oost. Towards a synthetic cell cycle. *Nat Commun*, 12(1):4531, 2021. ISSN 2041-1723 (Electronic) 2041-1723 (Linking). URL <https://doi.org/10.1038/s41467-021-24772-8>.
- [106] F. Oosawa. Size distribution of protein polymers. *J Theor Biol*, 27(1):69–86, 1970. URL [https://doi.org/10.1016/0022-5193\(70\)90129-3](https://doi.org/10.1016/0022-5193(70)90129-3).
- [107] C. Pallavicini, A. Monastra, N. G. Bardeci, D. Wetzler, V. Levi, and L. Bruno. Characterization of microtubule buckling in living cells. *Eur Biophys J*, 46(6):581–594, 2017. URL <https://doi.org/10.1007/s00249-017-1207-9>.

- [108] M. Piel and P. T. Tran. Cell shape and cell division in fission yeast. *Curr Biol*, 19(17):R823–7, 2009. ISSN 1879-0445 (Electronic) 0960-9822 (Linking). URL <https://doi.org/10.1016/j.cub.2009.08.012>.
- [109] B. M. Piette, J. Liu, K. Peeters, A. Smertenko, T. Hawkins, M. Deeks, R. Quinlan, W. J. Zakrzewski, and P. J. Hussey. A thermodynamic model of microtubule assembly and disassembly. *PLoS One*, 4(8):e6378, 2009. URL <https://doi.org/10.1371/journal.pone.0006378>.
- [110] M. Pilhofer, M. S. Ladinsky, A. W. McDowall, G. Petroni, and G. J. Jensen. Microtubules in bacteria: Ancient tubulins build a five-prot filament homolog of the eukaryotic cytoskeleton. *PLoS Biol*, 9(12):e1001213, 2011. ISSN 1545-7885 (Electronic) 1544-9173 (Linking). URL <https://doi.org/10.1371/journal.pbio.1001213>.
- [111] Suzanna L. Prosser and Laurence Pelletier. Mitotic spindle assembly in animal cells: a fine balancing act. *Nature Reviews Molecular Cell Biology*, 18(3):187–201, 2017. URL <https://doi.org/10.1038/nrm.2016.162>.
- [112] R. Reyes-Lamothe, T. Tran, D. Meas, L. Lee, A. M. Li, D. J. Sherratt, and M. E. Tolmashy. High-copy bacterial plasmids diffuse in the nucleoid-free space, replicate stochastically and are randomly partitioned at cell division. *Nucleic Acids Res*, 42(2):1042–51, 2014. URL <https://doi.org/10.1093/nar/gkt918>.
- [113] J. Rickman, C. Duellberg, N. I. Cade, L. D. Griffin, and T. Surrey. Steady-state eb cap size fluctuations are determined by stochastic microtubule growth and maturation. *Proc Natl Acad Sci U S A*, 114(13):3427–3432, 2017. ISSN 1091-6490 (Electronic) 0027-8424 (Linking). URL <https://doi.org/10.1073/pnas.1620274114>.
- [114] J. Roostalu, C. Thomas, N. I. Cade, S. Kunzelmann, I. A. Taylor, and T. Surrey. The speed of gtp hydrolysis determines gtp cap size and controls microtubule stability. *Elife*, 9, 2020. ISSN 2050-084X (Electronic) 2050-084X (Linking). URL <https://doi.org/10.7554/eLife.51992>.
- [115] S. W. Rothwell, W. A. Grasser, and D. B. Murphy. End-to-end annealing of microtubules in vitro. *J Cell Biol*, 102(2):619–27, 1986. ISSN 0021-9525 (Print) 0021-9525 (Linking). URL <https://doi.org/10.1083/jcb.102.2.619>.
- [116] Yoshihiko Sakaguchi, Tetsuya Hayashi, Ken Kurokawa, Keisuke Nakayama, Ken-shiro Oshima, Yukako Fujinaga, Makoto Ohnishi, Eiichi Ohtsubo, Masahira Hattori, and Keiji Oguma. The genome sequence of *Clostridium botulinum* type c neurotoxin-converting phage and the molecular mechanisms of unstable lysogeny. *Proceedings of the National Academy of Sciences*, 102(48), 2005. URL <https://doi.org/10.1073/pnas.0505503102>.
- [117] K. Sakamoto and W. R. Briggs. Cellular and subcellular localization of phototropin 1. *Plant Cell*, 14(8):1723–35, 2002. URL <https://doi.org/10.1105/tpc.003293>.

-
- [118] D. Schlieper, M. A. Oliva, J. M. Andreu, and J. Lowe. Structure of bacterial tubulin btuba/b: evidence for horizontal gene transfer. *Proc Natl Acad Sci USA*, 102(26): 9170–5, 2005. URL <https://doi.org/10.1073/pnas.0502859102>.
- [119] M. Schmidt-Cernohorska, I. Zhernov, E. Steib, M. Le Guennec, R. Achek, S. Borgers, D. Demurtas, L. Mouawad, Z. Lansky, V. Hamel, and P. Guichard. Flagellar microtubule doublet assembly in vitro reveals a regulatory role of tubulin c-terminal tails. *Science*, 363(6424):285–288, 2019. URL <https://doi.org/10.1126/science.aav2567>.
- [120] Y. L. Shih and L. Rothfield. The bacterial cytoskeleton. *Microbiol Mol Biol Rev*, 70(3):729–54, 2006. URL <https://doi.org/10.1128/MMBR.00017-06>.
- [121] C. A. Sontag, J. T. Staley, and H. P. Erickson. In vitro assembly and gtp hydrolysis by bacterial tubulins btuba and btubb. *J Cell Biol*, 169(2):233–8, 2005. ISSN 0021-9525 (Print) 0021-9525 (Linking). URL <https://doi.org/10.1083/jcb.200410027>.
- [122] H. Sui. Inside out: tubulin cytomotive filaments versus microtubules. *Structure*, 22(4):509–10, 2014. URL <https://doi.org/10.1016/j.str.2014.03.007>.
- [123] M. Takeda, A. Yoneya, Y. Miyazaki, K. Kondo, H. Makita, M. Kondoh, I. Suzuki, and J. Koizumi. *Prostheco bacter fluviatilis* sp. nov., which lacks the bacterial tubulin btuba and btubb genes. *Int J Syst Evol Microbiol*, 58(Pt 7):1561–5, 2008. URL <https://doi.org/10.1099/ijs.0.65787-0>.
- [124] R. P. Tas, C. Y. Chen, E. A. Katrukha, M. Vleugel, M. Kok, M. Dogterom, A. Akhmanova, and L. C. Kapitein. Guided by light: Optical control of microtubule gliding assays. *Nano Lett*, 18(12):7524–7528, 2018. ISSN 1530-6992 (Electronic) 1530-6984 (Linking). URL <https://doi.org/10.1021/acs.nanolett.8b03011>.
- [125] M. P. Tran, R. Chatterjee, Y. Dreher, J. Fichtler, K. Jahnke, L. Hilbert, V. Zaburdaev, and K. Gopfrich. A dna segregation module for synthetic cells. *Small*, page e2202711. URL <https://doi.org/10.1002/smll.202202711>.
- [126] Cynthia M. van den Berg, Vladimir A. Volkov, Sebastian Schnorrenberg, Ziqiang Huang, Kelly E. Stecker, Ilya Grigoriev, Sebastian Patzke, Timo Zimmermann, Marileen Dogterom, and Anna Akhmanova. Csppl stabilizes growing microtubule ends and damaged lattices from the luminal side. *bioRxiv*, page 2022.06.23.497320, 2022. URL <https://doi.org/10.1101/2022.06.23.497320>.
- [127] Jeffrey van Haren, Rabab A. Charafeddine, Andreas Ettinger, Hui Wang, Klaus M. Hahn, and Torsten Wittmann. Local control of intracellular microtubule dynamics by eb1 photodissociation. *Nature Cell Biology*, 20(3):252–261, 2018. URL <https://doi.org/10.1038/s41556-017-0028-5>.

- [128] V. VanBuren, D. J. Odde, and L. Cassimeris. Estimates of lateral and longitudinal bond energies within the microtubule lattice. *Proc Natl Acad Sci U S A*, 99(9): 6035–40, 2002. URL <https://doi.org/10.1073/pnas.092504999>.
- [129] M. Vleugel, M. Kok, and M. Dogterom. Understanding force-generating microtubule systems through in vitro reconstitution. *Cell Adh Migr*, 10(5):475–494, 2016. URL <https://doi.org/10.1080/19336918.2016.1241923>.
- [130] M. Vleugel, S. Roth, C. F. Groenendijk, and M. Dogterom. Reconstitution of basic mitotic spindles in spherical emulsion droplets. *J Vis Exp*, (114), 2016. ISSN 1940-087X (Electronic) 1940-087X (Linking). URL <https://doi.org/10.3791/54278>.
- [131] J. Wagstaff and J. Lowe. Prokaryotic cytoskeletons: protein filaments organizing small cells. *Nat Rev Microbiol*, 16(4):187–201, 2018. ISSN 1740-1534 (Electronic) 1740-1526 (Linking). URL <https://doi.org/10.1038/nrmicro.2017.153>.
- [132] R. A. Walker, E. T. O'Brien, N. K. Pryer, M. F. Soboeiro, W. A. Voter, H. P. Erickson, and E. D. Salmon. Dynamic instability of individual microtubules analyzed by video light microscopy: rate constants and transition frequencies. *J Cell Biol*, 107(4):1437–48, 1988. URL <https://doi.org/10.1083/jcb.107.4.1437>.
- [133] Marian Weiss, Johannes Patrick Frohnmayer, Lucia Theresa Benk, Barbara Haller, Jan-Willi Janiesch, Thomas Heitkamp, Michael Börsch, Rafael B. Lira, Rumiana Dimova, Reinhard Lipowsky, Eberhard Bodenschatz, Jean-Christophe Baret, Tanja Vidakovic-Koch, Kai Sundmacher, Ilia Platzman, and Joachim P. Spatz. Sequential bottom-up assembly of mechanically stabilized synthetic cells by microfluidics. *Nature Materials*, 17(1):89–96, 2018. URL <https://doi.org/10.1038/nmat5005>.
- [134] P. Zakharov, N. Gudimchuk, V. Voevodin, A. Tikhonravov, F. I. Ataullakhanov, and E. L. Grishchuk. Molecular and mechanical causes of microtubule catastrophe and aging. *Biophys J*, 109(12):2574–2591, 2015. ISSN 1542-0086 (Electronic) 0006-3495 (Linking). URL <https://doi.org/10.1016/j.bpj.2015.10.048>.
- [135] E. A. Zehr, J. A. Kraemer, M. L. Erb, J. K. Coker, E. A. Montabana, J. Pogliano, and D. A. Agard. The structure and assembly mechanism of a novel three-stranded tubulin filament that centers phage dna. *Structure*, 22(4):539–48, 2014. ISSN 1878-4186 (Electronic) 0969-2126 (Linking). URL <https://doi.org/10.1016/j.str.2014.02.006>.
- [136] S. Q. Zheng, E. Palovcak, J. P. Armache, K. A. Verba, Y. Cheng, and D. A. Agard. Motioncor2: anisotropic correction of beam-induced motion for improved cryo-electron microscopy. *Nat Methods*, 14(4):331–332, 2017. URL <https://doi.org/10.1038/nmeth.4193>.

ACKNOWLEDGEMENTS

Last five years many people were involved in my unique journey in my PhD duration in a quite different world which have helped me to make it to the end safe and sound. I would like to appreciate their presence, their help, and their love:

First of all, **Marileen**, I would like to thank you for giving me the chance to join the interesting project of synthetic cells. I learned a lot in these years and you were always very open and supportive of all the amazing things that I did. I would also like to thank my co-promoter, **Christophe**, thank you for co-promoting this thesis and being helpful and open for discussion.

Although I was not pursuing them seriously at the beginning, I should confess that MDo group meetings were among the most useful places for me to learn and to share. **Vladimir**, although it was hard for me to deal with your criticism at the beginning, your direct and thoughtful critique have had significant impact on my work in this new field; thanks for that all. **Eli**, your biochemistry knowledge and exceptional patience are exactly what a PhD student like me desires. Thanks for teaching me precious things and for being the real-world genie in the lab. **Anne**, thanks for being so helpful and hard working in the bacterial microtubule project. **Ashmiani** and **Angel**, thanks for the proteins you purified for my projects. **Esengül**, thanks for bringing laughter and organization to our lab. If I could I would have added the Saffron protocol somewhere in my thesis. **Ilina**, thank you for being an active and warm person in the group and thanks for the cool seed idea for cover. **Yash**, you always surprise me with the number of people you sneakily work with. We had a good collaboration and co-supervision experience, thanks for that and our discussions in the office. **Ali**, thanks for all the on- and off-campus time we spent together. **Nemo**, thank you for additionally organizing and digitizing the lab and a special thanks for all the renders you provided for the cover. **Beatriz**, thanks for taking over the project. Keep going and make a neat segregation system. **Esther** thanks for being so kind and always there to find a way to solve the administrative problems.

I would also like to thank former group members, **Renu**, **Louis**, **Maurits**, **Kim**, and **Jolijn**, thank you all for teaching me invaluable scientific and non-scientific lessons. Special thanks to **Maurits** for mentoring me throughout my first years and leaving behind precious materials for my project. Also, special thanks to **Celine** for all the help on last steps of my PhD and for thesis proofreading. **Elisa** and **Johannes**, thank you for teaching me how to use PURE and helping me with the protein expression assays. I would also like to thank my English language experts which proofread the thesis, many thanks to **Lyndsay** and **SaFyre**.

I had an exceptional experience in Tokyo in fourth year of my PhD which would have

not been possible without **Tomo's** help. Thanks to you and all group members of Prof. Uemura for warmly hosting me in UTokyo. I would also like to thank all the students that I had pleasure to supervise, **Ana, Catalina, Kaj,** and **Koen**. And now that I have started to be part of another great group I would like to thank everyone in Brouns lab: **Alicia, Aswin, Daan, Desi, Jelger, Lucia, Maartje, Pippi, Rita, Sam,** and **Stan**. Thank you all for your welcoming fun lab.

I would like to acknowledge all my BN colleagues and friends which made BN a nice place for working and growing: **Jochem, Becca, Sophie, Ana, Arash, Enzo, Leila, George, Milan, Afshin, Yoones, Nils,** and **Tanja**; thanks to all of you. **Richard**, thank you for being like a big brother to me and for all chats we had. I wish you all the best for your next career. **Roland**, thanks for for the long chats and climbing sessions we had together.

Off-campus, I had the great chance to live a cheerful life thanks to my amazing friends. A big thank to all of you: **Arash, Artemis, Behrouz, Cyrus, Darya, Elham, Elmira, Eunjeong, Fayeze, Hamed, Jalal, Magali Matthijs, Milad, Milad, Mohammad, Mojde, Morteza, Oghanian, Pedram, Reza, Sajad,** and **Zahra**.

And lastly, I would like to thank my parents and my siblings for their supporting perspectives from the world outside of science. **Maman, baba, Marzie, Mohsen, Zahra, Raha, Mehdi,** and **Mahdi**, I love you all.

LIST OF PUBLICATIONS

3. **R. Amini Hounejani**, V. A. Volkov, M. Dogterom, *Dynamic instability of force-generating bacterial microtubules*, [to be submitted] (Chapter 3)
2. **R. Amini Hounejani**, Y. Jawale, E. van der Sluis, B. Orozco Monroy, M. Dogterom, *A light-inducible hybrid synthetic DNA segregation system* [to be submitted] (Chapter 4)
1. C. Ijspeert*, **R. Amini Hounejani***, M. Dogterom, *Dynamic properties of PhuZ filaments*, [in preparation] (Chapter 5)

* contributed equally